JOURNAL OF PETROLOGY | VOLUME 50 | NUMBER 10 | PAGES 1857–1898 | 2009 | doi:10.1093/petrology/egp055

# Temporal Evolution of the Lithospheric Mantle beneath the Eastern North China Craton

**ZHU-YIN CHU[1]*, FU-YUAN WU[1], RICHARD J. WALKER[2], ROBERTA L. RUDNICK[2], LYNNETTE PITCHER[2], IGOR S. PUCHTEL[2], YUE-HENG YANG[1] AND SIMON A. WILDE[3]**

[1]STATE KEY LABORATORY OF LITHOSPHERIC EVOLUTION, INSTITUTE OF GEOLOGY AND GEOPHYSICS, CHINESE ACADEMY OF SCIENCES, BEIJING 100029, CHINA

[2]ISOTOPE GEOCHEMISTRY LABORATORY, DEPARTMENT OF GEOLOGY, UNIVERSITY OF MARYLAND, COLLEGE PARK, MD 20742, USA

[3]DEPARTMENT OF APPLIED GEOLOGY, CURTIN UNIVERSITY OF TECHNOLOGY, PO BOX U1987, PERTH, W.A. 6845, AUSTRALIA

**RECEIVED JANUARY 28, 2009; ACCEPTED JULY 28, 2009**
**ADVANCE ACCESS PUBLICATION SEPTEMBER 3, 2009**

*It is now well established that lithospheric thinning of the eastern North China Craton (NCC) occurred during the Phanerozoic. The cause and extent of the thinning, however, remains highly debated. In this study, mantle xenoliths from the Paleozoic Mengyin kimberlites, along with xenoliths from the Cenozoic Penglai and Shanwang basalts in Shandong Province, are investigated via traditional petrographic and elemental, Sr–Nd–Hf–Os isotopic and platinum-group element (PGE) analyses. Late Archean Os model ages of c. 2·5 Ga for the Mengyin peridotites provide confirmation that refractory, Archean lithospheric mantle existed beneath the easternmost portion of the NCC during the Paleozoic. Some Paleoproterozoic lithospheric mantle fragments may also be present in the Mengyin xenolith suite. In contrast, the spatially associated Penglai and Shanwang peridotite xenoliths are more fertile, and have Sr–Nd isotopic compositions similar to the depleted mantle. They differ dramatically from the Archean peridotites sampled by the Mengyin kimberlites. Osmium model ages for single samples range from mid-Proterozoic to modern, similar to variations observed in Phanerozoic convecting upper mantle as sampled by modern abyssal peridotites. This suggests that the present lithospheric mantle beneath the eastern NCC formed in the Phanerozoic, despite the fact that Os model ages extend back to the Proterozoic. Some samples from the Penglai suite yield Proterozoic Lu–Hf clinopyroxene mineral isochron ages that are consistent with the Os model ages, suggesting that Hf isotopes in modern convective upper mantle can preserve evidence for ancient melt depletion, similar to Os isotopes. Our results are consistent with thinning of the eastern NCC as a result of foundering of the deep crust and lithospheric mantle, but are inconsistent with stretching or refertilization models, as remnants of Archean mantle are expected to be present in these scenarios. The match between $^{187}Os/^{188}Os$ in convective upper mantle and the eastern China lithopspheric mantle also precludes models that seek to explain the present lithosphere as being due to lateral translation of Proterozoic lithosphere.*

KEY WORDS: *Cenozoic; isotopes; lithospheric mantle; Sm–Nd, Rb–Sr, Lu–Hf; North China Craton; Paleozoic; platinum-group elements (PGE); Re–Os*

## INTRODUCTION

Many studies have shown that a significant part of the original lithospheric mantle beneath the eastern portion of the North China Craton (NCC) was removed during the Phanerozoic (Fan & Menzies, 1992; Menzies *et al.*, 1993, 2007; Griffin *et al.*, 1998; Menzies & Xu, 1998; Xu, 2001). Early Paleozoic (~470 Ma) diamondiferous

*Corresponding author. Telephone: +86-10-82998586. Fax: +86-10-62010846. E-mail: zhychu@mail.igcas.ac.cn

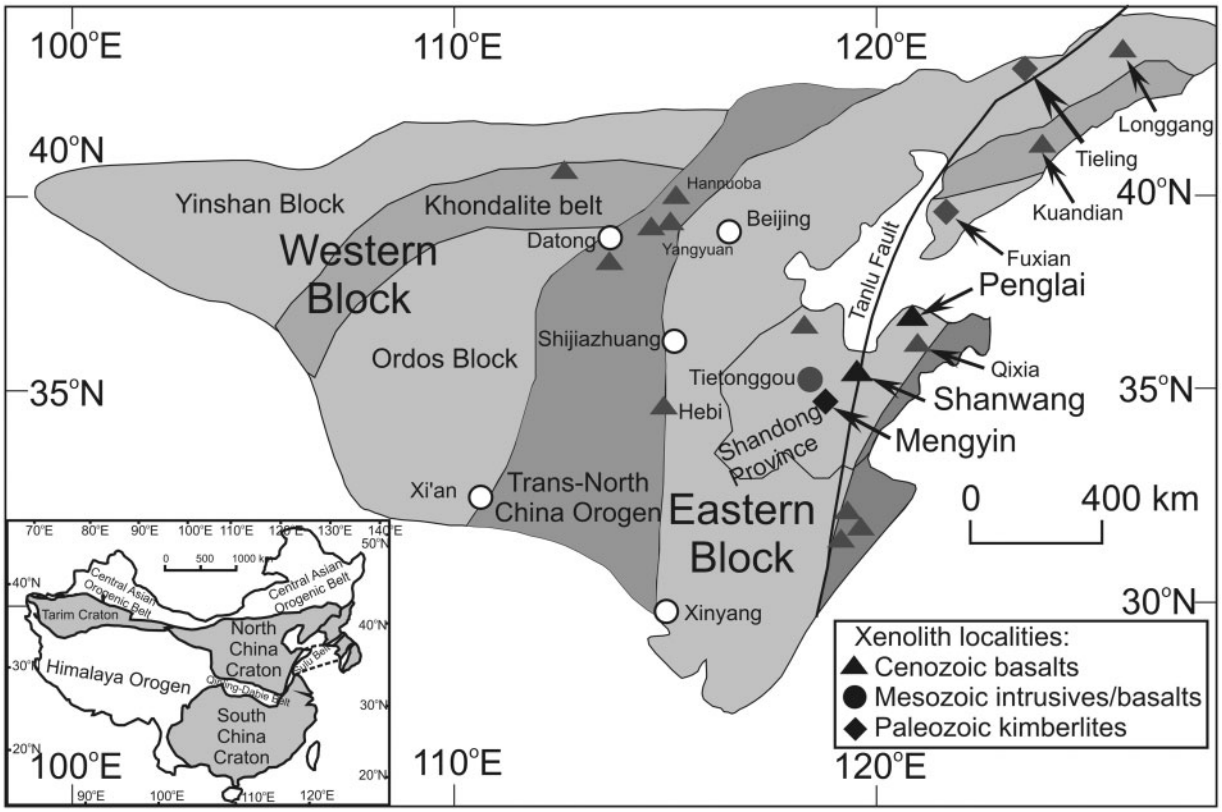


**Fig. 1.** Map of the North China Craton showing the xenolith localities discussed in the text. Tectonic subdivisions are based on Zhao *et al.* (2005). Inset shows location of the North China Craton (NCC) relative to other cratonic blocks (e.g. South China Craton) and intervening fold belts.

kimberlites in Mengyin, Shandong Province, and Fuxian, Liaoning Province, indicate the presence of lithosphere with a thickness of $\geq$200 km at the time of volcanism (Menzies *et al.*, 1993; Griffin *et al.*, 1998; Wang *et al.*, 1998; Menzies & Xu, 1998) (Fig. 1). Nevertheless, geophysical data and petrological studies of mantle xenoliths collected from Cenozoic basalts suggest that the present lithosphere is much thinner (60–120 km) and considerably more fertile (Menzies *et al.*, 1993; Griffin *et al.*, 1998; Menzies & Xu, 1998; Fan *et al.*, 2000; Xu, 2001; Rudnick *et al.*, 2004; Chen *et al.*, 2006). Because of these extensive studies, the eastern NCC is now recognized as the best example of a reactivated craton with decoupled crust and mantle lithosphere (Carlson *et al.*, 2005; Menzies *et al.*, 2007).

Despite extensive investigation, the cause of lithospheric thinning beneath the eastern block of the NCC remains highly debated. One school of thought suggests that the original Archean lithospheric mantle and associated lower crust were removed via density foundering, and were replaced by peridotite residues formed by melting of convecting upper mantle during the Mesozoic to early Cenozoic (Gao *et al.*, 2002, 2004, 2008; Wu *et al.*, 2003, 2005*a*). Another model suggests that mantle with Proterozoic Os model ages originated by mixing the original Archean mantle lithosphere with juvenile asthenospheric mantle via melt–peridotite interaction (Zhang, 2005; Zhang *et al.*, 2008). Others have proposed that this mantle lithosphere might be exotic, derived from southern China or elsewhere, and has no relationship with the crustal–mantle evolution of the NCC (Wu *et al.*, 2006).

Mapping of spatial variations in mantle melt depletion ages of the lithospheric mantle underlying the NCC before and after the loss of the deep lithosphere is essential to diagnose the cause of the loss (Carlson *et al.*, 2005; Foley, 2008). However, despite much recent study, the age structure of the lithospheric mantle underlying the NCC remains unclear, partly because of the paucity of data for appropriate xenolith locations. This is especially true for the easternmost portion of the NCC. To date, Os isotopic data have been reported for peridotite xenoliths from the Paleozoic Mengyin, Fuxian and Tieling kimberlites. These data reveal the existence of Archean lithospheric mantle beneath the eastern NCC during the early Paleozoic (Gao *et al.*, 2002; Wu *et al.*, 2006; Zhang *et al.*, 2008). In contrast, peridotite xenoliths from Cenozoic basalts in Qixia, Longgang, and Kuandian (Fig. 1) show considerable

variations in Os model ages. These model ages range from Proterozoic to Phanerozoic and have been interpreted in different ways. Most importantly, no peridotite xenoliths with Archean Os model ages have been documented in the Cenozoic basalts from the eastern NCC (Gao *et al.*, 2002; Wu *et al.*, 2003, 2006).

With the intent of providing a much more detailed picture of the age structure of the mantle lithosphere underlying the eastern portion of the NCC, we have determined the petrography, major and trace element chemistry, Sr–Nd–Hf–Os isotope and platinum-group element (PGE) concentrations for two large suites of peridotite xenoliths from the Cenozoic Penglai and Shanwang basalts in Shandong Province. These data complement published data for the nearby Qixia peridotites (Gao *et al.*, 2002; Rudnick *et al.*, 2004). To bolster limited earlier data and further constrain the nature of the lithospheric mantle present during the Paleozoic, we also analyzed additional mantle xenoliths from the Paleozoic Mengyin kimberlites.

## GEOLOGICAL BACKGROUND AND SAMPLE DESCRIPTIONS

Eastern China is composed of the three main lithotectonic domains, the Central Asian Orogenic Belt and the NCC in the north, the Dabie–Sulu ultrahigh-pressure collisional belt in the central region, and the South China Craton (including the Yangtze Craton and Southeastern China orogenic belt) in the south (Fig. 1). The NCC is the oldest tectonic unit in China, containing crust as old as 3800 Ma (Liu *et al.*, 1992; Wu *et al.*, 2008). Neodymium $T_{DM}$ model ages of felsic rocks are generally Archean and range mainly between 2·5 and 3·9 Ga, with two age peaks at 2·6–2·8 Ga and 3·2–3·6 Ga (Wu *et al.*, 2005*b*), indicating Archean crust formation. Petrologically, the NCC is composed mainly of various gneisses, granulites, amphibolites and supracrustal rocks.

The NCC can be divided into Eastern and Western blocks, which collided along the Trans-North China Orogen at ~1·85 Ga (Zhao *et al.*, 2005) (Fig. 1). The Western Block can be further divided into the Yinshan Block in the north and Ordos Block in the south, which are separated by the east–west-trending Paleoproterozoic Khondalite Belt (Zhao *et al.*, 2005). Within the Eastern Block, a Paleoproterozoic collisional belt is also present on the Liaodong–Jiaodong peninsulas (darker gray shading in northeastern NCC in Fig. 1; Faure *et al.*, 2004; Zhao *et al.*, 2005; Lu *et al.*, 2006).

From ~1·85 Ga until the late Mesozoic, the NCC remained stable. Starting in the Mesozoic, intensive deformation, mineralization, and igneous activity occurred, including extensive eruption of intermediate–acid volcanic rocks and widespread emplacement of granites (Wu *et al.*, 2005*a*, 2005*c*). During the Cenozoic, the NCC has witnessed extensive intraplate basaltic volcanism. Some of these basalts contain abundant ultramafic xenoliths (Fig. 1).

In Shandong Province, three stages of igneous rocks from the Paleozoic, Mesozoic, and Cenozoic contain mantle xenoliths and provide a unique opportunity to study the evolution of the lithospheric mantle throughout the critical period of lithosphere transformation within a spatially restricted region. The Mengyin kimberlite, emplaced during the Paleozoic at ~470 Ma (Dobbs *et al.*, 1994; Zhang & Yang, 2007; Yang *et al.*, 2009), contains abundant harzburgite xenoliths (Chi & Lu, 1996; Gao *et al.*, 2002; Zheng *et al.*, 2007; Zhang *et al.*, 2008). Among the Mesozoic rocks, the Tietonggou diorite in Laiwu (~125 Ma) contains harzburgite and dunite xenoliths, some of which yield Archean Os model ages (W. L. Xu, *et al.*, 2008; Gao *et al.*, 2008). During the Cenozoic, alkaline volcanic activity occurred in numerous localities, including Qixia (Gao *et al.*, 2002; Rudnick *et al.*, 2004), Penglai and Shanwang (Fig. 1). The Penglai volcanoes, erupted during the Neogene at 5·7–4·2 Ma (Liu, 1999), are located in the northeastern portion of the Shandong Peninsula, about 500 km to the NE of the Mengyin kimberlite, and about 100 km to the north of Qixia. The Shanwang volcanoes, erupted at ~16 Ma (Liu, 1999; Zheng *et al.*, 2007), are located *c.* 100 km to the north of the Paleozoic Mengyin kimberlite, within the Tan–Lu Fault.

Mantle xenoliths in the Mengyin kimberlite are rounded and average 5–8 cm across. They have been intensively altered, and only garnet remains as a primary mineral (Chi & Lu, 1996; Zhang *et al.*, 2008; Gao *et al.*, 2002). In contrast, lavas at both the Penglai and Shanwang volcanoes contain abundant, fresh xenoliths of lherzolite and pyroxenite, with minor harzburgite and wehrlite. Photographs of outcrop and hand specimens of some Penglai and Shanwang xenoliths are provided in an electronic supplement (available for downloading at http://www.petrology.oxfordjournals.org/). Petrographic descriptions of the samples analysed in this study are given in Appendix A.

At Penglai, most xenoliths range in size between 5 and 10 cm. These peridotite xenoliths are fresh, generally coarse-grained (1–3 mm) and equigranular, with some showing porphyroclastic textures (Fig. 2a and b). No strongly foliated types have been found. Primary minerals are olivine, orthopyroxene (opx), clinopyroxene (cpx), and spinel (Fig. 2a and b); most xenoliths are lherzolites, but minor harzburgite also occurs (Table 1).

The xenoliths at Shanwang are larger, typically ranging from 10 to 20 cm across. These xenoliths are characterized by four types of microstructures (protogranular, transitional, tabular equigranular, and porphyroclastic texture) (Fig. 2c and d), with primary mineral assemblages consisting of olivine, cpx, opx, and spinel (Fig. 2c and d). Again,

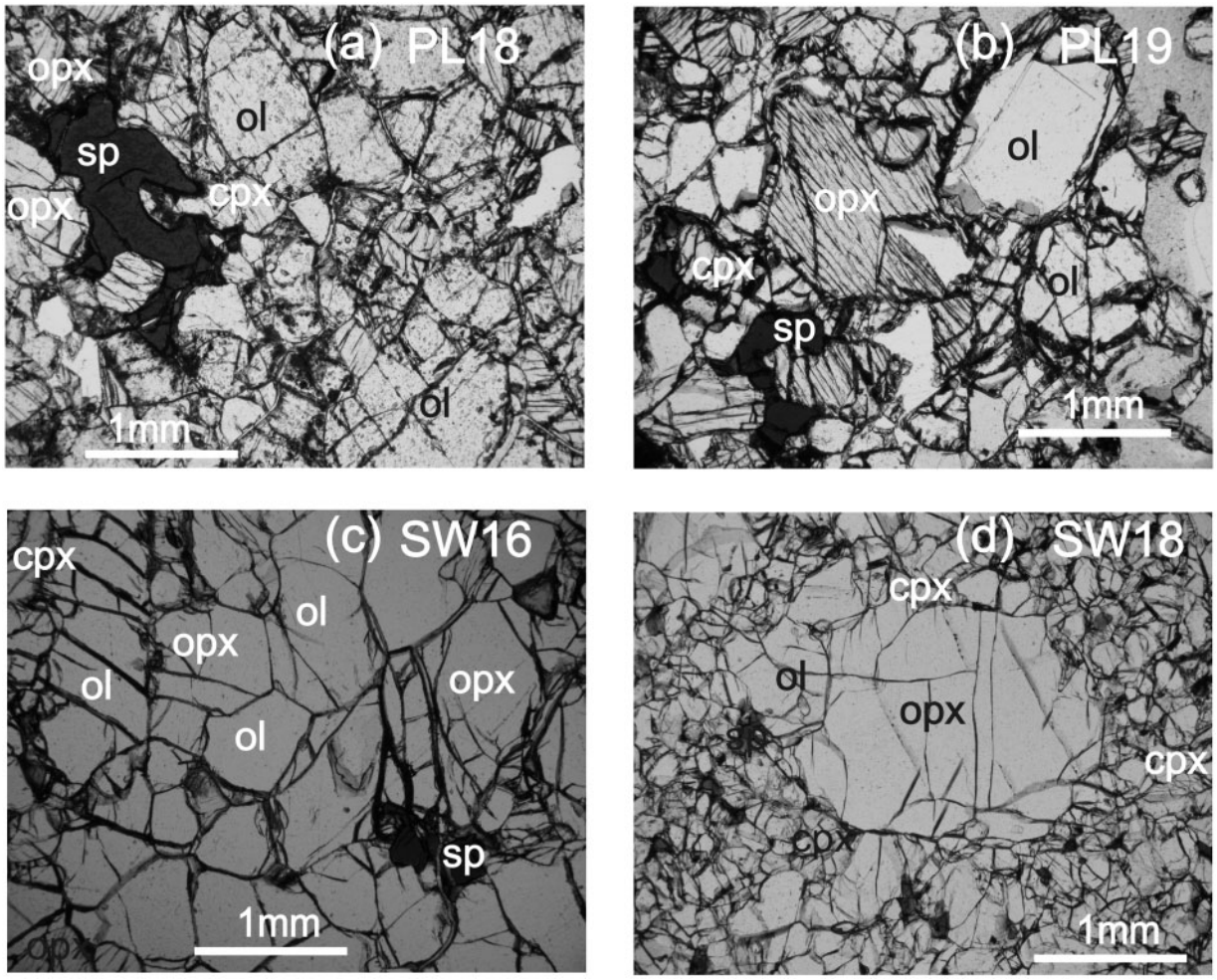


**Fig. 2.** Photomicrographs of representative textures in mantle xenoliths from Penglai (a, b) and Shanwang (c, d). (a, b) Penglai xenoliths PL18 and PL19 show equigranular to porphyroclastic textures (plane-polarized light); (c) Shanwang xenolith SW16 with granuloblastic texture (plane-polarized light); (d) Shanwang xenolith SW18 with porphyroclastic texture (plane-polarized light). Petrographic descriptions of the samples are given in Appendix A.

lherzolite dominates the rock types, but harzburgites also occur, as well as pyroxenites (SW04) and wehrlites (SW01, SW21) (Table 1). The lack of garnet in peridotite xenoliths from both Penglai and Shanwang studied here indicates derivation of these samples from depths of <80 km. Reports of garnet-bearing lherzolites from Shanwang, however, indicate that some peridotites from this locale were derived from depths of ≥~80 km (Zheng *et al.*, 2006).

## ANALYTICAL TECHNIQUES

The xenoliths were sawn from their lava hosts and the cut surfaces were abraded with quartz in a sand blaster to remove any possible contamination from the saw blade. The samples were first crushed using an alumina ceramic jaw crusher, and then small chips, devoid of surface alteration and host lava, were ground into a fine powder using an agate shatterbox. A portion of the crushed fraction was sieved and cpx separates were handpicked under a binocular microscope to a purity of >98%.

### Elemental analysis

Major element data for whole-rock samples were obtained by X-ray fluorescence spectrometry (XRF) on fused glass disks using a Shimadzu XRF-1500 instrument at the Institute of Geology and Geophysics, Chinese Academy of Sciences (see Appendix B for details). Precisions are ±1–3% relative for elements present in concentrations >1 wt %, and about ±10% relative for elements present in concentrations <1·0 wt %. A Chinese ultramafic rock reference material, DZE-1, was analyzed during the same period, and the values determined are well within the range of consensus values (Appendix B: Table B1).

Trace element concentrations, including the rare earth elements (REE), were determined by inductively coupled plasma mass spectrometry (ICP-MS) using an Agilent

*Table 1: Major and trace element compositions of the studied xenoliths*

| | MY9 | MY10 | MY33 | MY34 | MY35 | PL01 | PL02 | PL03 | PL06 | PL07 | PL08 |
|---|---|---|---|---|---|---|---|---|---|---|---|
| Lithology: | Hz | D | Hz | Hz | Px | Lz | Hz | Lz | Lz | Lz | Lz |
| *Modal compositions (%)** | | | | | | | | | | | |
| Ol | | | | | | 58·9 | 75·2 | 53·1 | 56·1 | 56·0 | 73·2 |
| Opx | | | | | | 25·7 | 20·5 | 30·1 | 24·8 | 25·9 | 19·3 |
| Cpx | | | | | | 12·4 | 3·4 | 14·1 | 15·4 | 15·2 | 5·8 |
| Sp | | | | | | 3·1 | 1·0 | 2·7 | 3·7 | 3·0 | 1·7 |
| Fo | | | | | | 89·8 | 90·8 | 88·7 | 89·9 | 89·6 | 91·3 |
| *Major elements (wt %)* | | | | | | | | | | | |
| $SiO_2$ | 40·8 | 36·3 | 39·7 | 40·8 | 37·1 | 45·0 | 44·2 | 44·2 | 44·7 | 45·2 | 44·1 |
| $TiO_2$ | 0·10 | 0·04 | 0·49 | 0·05 | 0·32 | 0·11 | 0·04 | 0·22 | 0·18 | 0·13 | 0·06 |
| $Al_2O_3$ | 0·32 | 0·06 | 0·27 | 0·79 | 8·67 | 3·56 | 1·19 | 3·97 | 4·31 | 3·96 | 1·69 |
| $TFe_2O_3$ | 4·22 | 7·75 | 6·05 | 3·96 | 8·08 | 8·34 | 8·15 | 10·92 | 8·28 | 8·47 | 7·97 |
| MnO | 0·07 | 0·07 | 0·05 | 0·05 | 0·13 | 0·11 | 0·12 | 0·14 | 0·11 | 0·12 | 0·11 |
| MgO | 39·4 | 44·6 | 38·7 | 39·3 | 28·9 | 39·3 | 44·5 | 36·1 | 38·2 | 37·9 | 43·8 |
| CaO | 0·64 | 0·21 | 0·44 | 0·46 | 2·72 | 2·61 | 1·01 | 2·79 | 3·27 | 3·08 | 1·39 |
| $Na_2O$ | 0·00 | 0·00 | 0·00 | 0·00 | 0·00 | 0·21 | 0·05 | 0·44 | 0·33 | 0·28 | 0·10 |
| $K_2O$ | 0·04 | 0·02 | 0·02 | 0·03 | 0·21 | 0·04 | 0·05 | 0·12 | 0·07 | 0·05 | 0·05 |
| $P_2O_5$ | 0·05 | 0·03 | 0·03 | 0·02 | 0·20 | 0·02 | 0·02 | 0·07 | 0·04 | 0·02 | 0·03 |
| LOI | 14·0 | 10·5 | 14·0 | 14·0 | 13·4 | −0·17 | −0·13 | 0·55 | 0·03 | 0·13 | 0·10 |
| Total | 99·7 | 99·6 | 99·7 | 99·5 | 99·7 | 99·2 | 99·2 | 99·4 | 99·5 | 99·4 | 99·4 |
| *Trace elements (ppm)* | | | | | | | | | | | |
| Ni | 2447 | 2729 | 2587 | 3227 | 427 | 2290 | 2743 | 2168 | 1964 | 1888 | 2704 |
| Cu | 1·74 | 6·52 | 3·87 | 2·52 | 3·42 | 16·7 | 13·9 | 28·1 | 24·2 | 23·7 | 25·8 |
| Zn | 23·8 | 38·1 | 23·3 | 33·6 | 52·7 | 57·8 | 51·1 | 102 | 61·1 | 57·8 | 49·5 |
| Sr | 40·1 | 23·9 | 32·8 | 50·3 | 225 | 20·3 | 19·9 | 132 | 52·3 | 24·5 | 37·4 |
| Y | 3·37 | 0·264 | 3·88 | 2·98 | 3·93 | 3·18 | 0·638 | 4·58 | 4·01 | 3·62 | 1·12 |
| Zr | 15·2 | 5·78 | 25·9 | 19·4 | 72·9 | 8·76 | 5·18 | 33·1 | 16·8 | 9·77 | 8·27 |
| Nb | 15·1 | 5·89 | 17·7 | 14·2 | 60·7 | 0·640 | 1·30 | 7·54 | 3·27 | 1·21 | 2·34 |
| Ba | 24·2 | 66·1 | 3·38 | 14·2 | 308 | 7·32 | 7·65 | 58·0 | 23·0 | 13·0 | 10·7 |
| Hf | 0·386 | 0·113 | 1·61 | 1·13 | 1·42 | 0·184 | 0·085 | 0·547 | 0·407 | 0·261 | 0·151 |
| Ta | 0·294 | 0·259 | 0·976 | 0·322 | 2·46 | 0·019 | 0·048 | 0·348 | 0·155 | 0·051 | 0·093 |
| Pb | 0·383 | 0·699 | 0·211 | 0·229 | 0·770 | 0·330 | 0·403 | 0·856 | 1·13 | 1·27 | 0·236 |
| Th | 0·270 | 0·564 | 0·325 | 0·155 | 7·58 | 0·073 | 0·075 | 0·495 | 0·311 | 0·103 | 0·157 |
| U | 0·742 | 0·088 | 0·760 | 0·495 | 1·71 | 0·019 | 0·024 | 0·137 | 0·092 | 0·031 | 0·047 |
| S | 480 | 510 | 210 | 440 | 140 | <50 | <50 | 260 | 50 | <50 | 50 |
| *Rare earth elements (ppm)* | | | | | | | | | | | |
| La | 20·5 | 3·77 | 26·4 | 24·7 | 90·7 | 0·464 | 0·570 | 4·65 | 1·77 | 1·18 | 1·09 |
| Ce | 24·5 | 6·42 | 31·6 | 29·2 | 120 | 1·14 | 1·20 | 9·12 | 3·78 | 1·88 | 2·24 |
| Pr | 2·01 | 0·629 | 2·41 | 2·29 | 10·0 | 0·160 | 0·137 | 1·27 | 0·454 | 0·318 | 0·270 |
| Nd | 6·94 | 2·05 | 7·31 | 7·27 | 30·4 | 0·828 | 0·572 | 5·57 | 2·11 | 1·49 | 1·15 |
| Sm | 1·11 | 0·262 | 1·00 | 0·915 | 3·64 | 0·280 | 0·120 | 1·22 | 0·580 | 0·432 | 0·252 |
| Eu | 0·397 | 0·076 | 0·187 | 0·233 | 0·779 | 0·103 | 0·040 | 0·420 | 0·209 | 0·157 | 0·084 |
| Gd | 1·26 | 0·206 | 1·14 | 0·971 | 3·13 | 0·399 | 0·120 | 1·30 | 0·723 | 0·580 | 0·258 |
| Tb | 0·130 | 0·018 | 0·125 | 0·095 | 0·263 | 0·071 | 0·017 | 0·175 | 0·121 | 0·100 | 0·036 |
| Dy | 0·635 | 0·068 | 0·648 | 0·439 | 1·01 | 0·478 | 0·108 | 0·946 | 0·773 | 0·677 | 0·210 |
| Ho | 0·109 | 0·010 | 0·130 | 0·078 | 0·152 | 0·106 | 0·021 | 0·170 | 0·167 | 0·144 | 0·040 |
| Er | 0·262 | 0·025 | 0·338 | 0·194 | 0·386 | 0·314 | 0·061 | 0·424 | 0·477 | 0·433 | 0·114 |
| Tm | 0·030 | 0·003 | 0·041 | 0·024 | 0·043 | 0·044 | 0·009 | 0·053 | 0·067 | 0·062 | 0·016 |
| Yb | 0·167 | 0·016 | 0·235 | 0·145 | 0·274 | 0·316 | 0·070 | 0·329 | 0·442 | 0·425 | 0·114 |
| Lu | 0·021 | 0·002 | 0·030 | 0·021 | 0·040 | 0·047 | 0·011 | 0·048 | 0·068 | 0·066 | 0·017 |

(continued)

*Table 1: Continued*

| | PL10 | PL11 | PL12 | PL13 | PL14 | PL15 | PL16 | PL17 | PL18 | PL19 | PL23 |
|---|---|---|---|---|---|---|---|---|---|---|---|
| Lithology: | Lz | Lz | Lz | Lz | Lz | Lz | Lz | Lz | Hz | Lz | Hz |
| *Modal compositions (%)* | | | | | | | | | | | |
| Ol | | | | 59·2 | 61·2 | | 58·2 | 59·8 | 70·9 | 68·0 | 64·2 |
| Opx | | | | 24·5 | 23·4 | | 24·5 | 25·6 | 21·8 | 22·4 | 30·0 |
| Cpx | | | | 12·8 | 12·5 | | 14·4 | 11·3 | 4·7 | 7·6 | 3·7 |
| Sp | | | | 3·4 | 2·9 | | 2·9 | 3·3 | 2·7 | 2·0 | 2·1 |
| Fo | | | | 89·5 | 90·4 | | 88·1 | 90·3 | 90·7 | 90·4 | 91·1 |
| *Major elements (wt %)* | | | | | | | | | | | |
| $SiO_2$ | 44·4 | 44·3 | 44·2 | 44·6 | 44·6 | 45·0 | 44·0 | 44·7 | 43·7 | 44·5 | 45·6 |
| $TiO_2$ | 0·14 | 0·08 | 0·11 | 0·15 | 0·11 | 0·08 | 0·18 | 0·12 | 0·09 | 0·02 | 0·05 |
| $Al_2O_3$ | 3·22 | 2·77 | 1·85 | 3·89 | 3·45 | 2·46 | 3·83 | 3·67 | 2·26 | 2·43 | 1·87 |
| $TFe_2O_3$ | 8·38 | 8·30 | 8·15 | 8·52 | 7·97 | 8·45 | 10·79 | 8·23 | 8·88 | 8·28 | 7·97 |
| MnO | 0·12 | 0·11 | 0·11 | 0·12 | 0·10 | 0·12 | 0·13 | 0·12 | 0·12 | 0·11 | 0·10 |
| MgO | 40·4 | 41·8 | 43·0 | 39·0 | 40·0 | 41·2 | 37·2 | 39·7 | 43·0 | 42·1 | 42·5 |
| CaO | 2·42 | 1·81 | 1·56 | 2·84 | 2·81 | 1·98 | 2·85 | 2·59 | 1·17 | 1·94 | 1·19 |
| $Na_2O$ | 0·27 | 0·12 | 0·18 | 0·24 | 0·24 | 0·16 | 0·34 | 0·22 | 0·09 | 0·07 | 0·07 |
| $K_2O$ | 0·06 | 0·07 | 0·14 | 0·04 | 0·04 | 0·05 | 0·05 | 0·06 | 0·06 | 0·03 | 0·04 |
| $P_2O_5$ | 0·03 | 0·03 | 0·07 | 0·03 | 0·03 | 0·02 | 0·04 | 0·03 | 0·03 | 0·01 | 0·02 |
| LOI | −0·27 | −0·12 | −0·23 | −0·02 | −0·05 | −0·23 | 0·17 | −0·02 | 0·03 | −0·28 | −0·05 |
| Total | 99·1 | 99·2 | 99·2 | 99·4 | 99·3 | 99·2 | 99·5 | 99·4 | 99·4 | 99·2 | 99·3 |
| *Trace elements (ppm)* | | | | | | | | | | | |
| Ni | 2356 | 2178 | 2232 | 2284 | 2039 | 2020 | 1871 | 2312 | 2260 | 2115 | 2113 |
| Cu | 20·9 | 14·8 | 11·5 | 17·6 | 15·2 | 11·2 | 25·3 | 24·6 | 16·0 | 12·2 | 12·0 |
| Zn | 61·7 | 61·8 | 51·9 | 59·3 | 57·4 | 46·4 | 79·6 | 59·5 | 60·3 | 52·0 | 53·2 |
| Sr | 51·4 | 43·8 | 113 | 43·6 | 39·8 | 34·1 | 62·4 | 49·9 | 46·8 | 18·4 | 25·0 |
| Y | 3·18 | 1·33 | 1·88 | 3·82 | 3·03 | 1·91 | 3·34 | 2·90 | 1·33 | 1·08 | 0·634 |
| Zr | 12·8 | 11·7 | 16·5 | 14·0 | 10·7 | 8·13 | 19·6 | 12·1 | 11·4 | 3·89 | 6·75 |
| Nb | 2·32 | 3·85 | 5·17 | 2·08 | 1·89 | 1·41 | 2·61 | 3·15 | 3·34 | 0·826 | 1·65 |
| Ba | 29·3 | 30·3 | 45·9 | 12·4 | 12·9 | 14·1 | 13·1 | 19·3 | 22·7 | 7·00 | 10·9 |
| Hf | 0·286 | 0·240 | 0·289 | 0·312 | 0·271 | 0·169 | 0·389 | 0·257 | 0·254 | 0·083 | 0·159 |
| Ta | 0·111 | 0·199 | 0·235 | 0·095 | 0·099 | 0·066 | 0·134 | 0·147 | 0·178 | 0·043 | 0·090 |
| Pb | 0·748 | 0·471 | 0·671 | 0·446 | 0·685 | 0·544 | 0·347 | 0·436 | 0·417 | 0·236 | 0·595 |
| Th | 0·180 | 0·317 | 0·459 | 0·148 | 0·182 | 0·140 | 0·245 | 0·241 | 0·264 | 0·141 | 0·184 |
| U | 0·059 | 0·097 | 0·125 | 0·054 | 0·054 | 0·038 | 0·073 | 0·070 | 0·077 | 0·046 | 0·055 |
| S | <50 | <50 | <50 | <50 | <50 | <50 | 60 | <50 | 50 | <50 | 50 |
| *Rare earth elements (ppm)* | | | | | | | | | | | |
| La | 1·52 | 2·18 | 3·80 | 1·22 | 1·39 | 0·836 | 1·96 | 1·75 | 1·77 | 0·873 | 0·985 |
| Ce | 3·05 | 3·50 | 7·48 | 2·63 | 2·89 | 1·89 | 4·35 | 3·59 | 3·88 | 1·77 | 2·18 |
| Pr | 0·387 | 0·440 | 0·842 | 0·345 | 0·348 | 0·220 | 0·539 | 0·386 | 0·402 | 0·183 | 0·226 |
| Nd | 1·71 | 1·77 | 3·35 | 1·62 | 1·56 | 0·980 | 2·44 | 1·63 | 1·70 | 0·721 | 0·939 |
| Sm | 0·447 | 0·354 | 0·671 | 0·451 | 0·410 | 0·253 | 0·602 | 0·403 | 0·367 | 0·143 | 0·187 |
| Eu | 0·173 | 0·119 | 0·221 | 0·174 | 0·155 | 0·099 | 0·211 | 0·144 | 0·121 | 0·049 | 0·064 |
| Gd | 0·539 | 0·361 | 0·641 | 0·605 | 0·527 | 0·320 | 0·682 | 0·492 | 0·382 | 0·164 | 0·188 |
| Tb | 0·090 | 0·049 | 0·081 | 0·100 | 0·090 | 0·053 | 0·107 | 0·080 | 0·054 | 0·029 | 0·026 |
| Dy | 0·570 | 0·275 | 0·416 | 0·663 | 0·571 | 0·337 | 0·643 | 0·501 | 0·303 | 0·202 | 0·133 |
| Ho | 0·119 | 0·055 | 0·069 | 0·139 | 0·123 | 0·071 | 0·124 | 0·106 | 0·055 | 0·044 | 0·026 |
| Er | 0·343 | 0·148 | 0·174 | 0·405 | 0·355 | 0·218 | 0·341 | 0·298 | 0·153 | 0·142 | 0·071 |
| Tm | 0·048 | 0·021 | 0·021 | 0·059 | 0·049 | 0·030 | 0·047 | 0·043 | 0·020 | 0·022 | 0·011 |
| Yb | 0·322 | 0·151 | 0·130 | 0·381 | 0·330 | 0·216 | 0·313 | 0·299 | 0·144 | 0·163 | 0·079 |
| Lu | 0·050 | 0·025 | 0·019 | 0·059 | 0·051 | 0·034 | 0·044 | 0·045 | 0·023 | 0·027 | 0·014 |

(continued)

*Table 1: Continued*

| | SW01 | SW02 | SW03 | SW04 | SW05 | SW06 | SW07 | SW08 | SW09 | SW10 | SW11 | SW12 |
|---|---|---|---|---|---|---|---|---|---|---|---|---|
| Lithology: | W | Lz | Lz | Px | Lz | Lz | Hz | Lz | Lz | Lz | Lz | Lz |
| *Modal compositions (%)* | | | | | | | | | | | | |
| Ol | | 58·7 | 51·7 | 34·9 | 63·7 | 60·8 | 76·6 | 60·7 | 72·8 | 62·6 | 64·9 | 56·7 |
| Opx | | 21·0 | 35·2 | 15·1 | 23·0 | 27·1 | 17·8 | 22·1 | 17·7 | 22·3 | 20·8 | 25·2 |
| Cpx | | 17·7 | 11·0 | 50·0 | 11·2 | 10·4 | 4·8 | 14·4 | 7·6 | 12·2 | 12·8 | 15·2 |
| Sp | | 2·6 | 2·1 | 0·02 | 2·2 | 1·8 | 0·8 | 2·7 | 1·9 | 2·9 | 1·5 | 2·9 |
| Fo | | 90·0 | 89·9 | 90·3 | 86·1 | 89·6 | 90·7 | 89·1 | 90·9 | 90·2 | 90·8 | 89·3 |
| *Major elements (wt %)* | | | | | | | | | | | | |
| $SiO_2$ | 41·3 | 44·3 | 44·9 | 43·2 | 44·3 | 44·9 | 43·7 | 44·3 | 43·6 | 44·5 | 44·2 | 44·8 |
| $TiO_2$ | 0·30 | 0·08 | 0·06 | 0·08 | 0·09 | 0·11 | 0·02 | 0·12 | 0·02 | 0·07 | 0·06 | 0·09 |
| $Al_2O_3$ | 2·29 | 3·29 | 3·07 | 3·19 | 2·70 | 2·93 | 1·21 | 3·46 | 1·79 | 3·08 | 2·22 | 3·58 |
| $TFe_2O_3$ | 14·23 | 8·18 | 8·94 | 7·60 | 9·51 | 8·42 | 8·13 | 8·88 | 8·13 | 8·05 | 7·95 | 8·54 |
| MnO | 0·18 | 0·12 | 0·10 | 0·10 | 0·13 | 0·11 | 0·10 | 0·13 | 0·09 | 0·11 | 0·09 | 0·12 |
| MgO | 34·8 | 37·7 | 37·2 | 26·0 | 38·8 | 39·9 | 44·1 | 38·6 | 42·9 | 40·0 | 40·5 | 38·0 |
| CaO | 5·05 | 3·75 | 2·36 | 9·26 | 2·64 | 2·38 | 1·09 | 3·02 | 1·62 | 2·62 | 2·78 | 3·31 |
| $Na_2O$ | 0·17 | 0·16 | 0·13 | 0·20 | 0·19 | 0·18 | 0·05 | 0·21 | 0·09 | 0·12 | 0·12 | 0·18 |
| $K_2O$ | 0·09 | 0·06 | 0·10 | 0·20 | 0·09 | 0·04 | 0·05 | 0·08 | 0·05 | 0·03 | 0·03 | 0·03 |
| $P_2O_5$ | 0·03 | 0·02 | 0·03 | 0·03 | 0·02 | 0·03 | 0·03 | 0·05 | 0·03 | 0·04 | 0·03 | 0·02 |
| LOI | 1·05 | 1·88 | 2·48 | 9·69 | 0·98 | 0·40 | 0·95 | 0·48 | 1·02 | 0·78 | 1·42 | 0·79 |
| Total | 99·5 | 99·4 | 99·4 | 99·5 | 99·5 | 99·4 | 99·4 | 99·4 | 99·4 | 99·4 | 99·4 | 99·4 |
| *Trace elements (ppm)* | | | | | | | | | | | | |
| Ni | 1808 | 2412 | 2686 | 2363 | 2449 | 2343 | 2854 | 2294 | 2630 | 2391 | 2507 | 2266 |
| Cu | 47·1 | 29·8 | 24·0 | 32·4 | 2·7 | 33·2 | 12·4 | 12·0 | 14·1 | 26·9 | 20·6 | 41·2 |
| Zn | 93·4 | 53·7 | 61·2 | 57·4 | 75·1 | 60·0 | 53·7 | 63·2 | 59·5 | 56·2 | 52·4 | 52·4 |
| Sr | 111 | 75·8 | 59·2 | 2120 | 72·6 | 34·1 | 27·7 | 53·9 | 42·8 | 34·2 | 159 | 18·3 |
| Y | 3·46 | 2·82 | 2·14 | 2·54 | 2·80 | 2·91 | 0·668 | 4·27 | 0·882 | 2·31 | 1·67 | 3·24 |
| Zr | 16·9 | 2·48 | 2·30 | 6·04 | 6·59 | 9·95 | 3·39 | 11·7 | 4·04 | 2·09 | 4·00 | 2·25 |
| Nb | 0·983 | 0·083 | 0·362 | 1·15 | 1·41 | 0·972 | 0·327 | 1·09 | 0·231 | 0·078 | 0·445 | 0·032 |
| Ba | 4·47 | 1·44 | 2·36 | 14·3 | 4·80 | 2·44 | 2·10 | 4·09 | 0·985 | 1·44 | 1·56 | 0·225 |
| Hf | 0·453 | 0·101 | 0·084 | 0·094 | 0·166 | 0·237 | 0·055 | 0·267 | 0·075 | 0·086 | 0·101 | 0·114 |
| Ta | 0·061 | 0·001 | 0·005 | 0·003 | 0·050 | 0·046 | 0·017 | 0·050 | 0·020 | 0·016 | 0·016 | — |
| Pb | 0·161 | 0·117 | 0·100 | 1·13 | 0·083 | 0·393 | 0·636 | 0·071 | 0·173 | 0·154 | 0·248 | 0·090 |
| Th | 0·119 | 0·015 | 0·012 | 0·020 | 0·032 | 0·045 | 0·044 | 0·107 | 0·052 | 0·039 | 0·089 | 0·006 |
| U | 0·035 | 0·012 | 0·011 | 0·019 | 0·053 | 0·021 | 0·013 | 0·033 | 0·017 | 0·013 | 0·039 | 0·004 |
| S | <50 | 50 | 80 | 60 | <50 | 80 | 60 | <50 | <50 | 80 | 90 | 270 |
| *Rare earth elements (ppm)* | | | | | | | | | | | | |
| La | 1·76 | 0·052 | 0·220 | 0·262 | 1·28 | 1·29 | 1·03 | 2·49 | 0·980 | 0·082 | 0·595 | 0·053 |
| Ce | 4·04 | 0·147 | 0·380 | 0·497 | 3·18 | 3·21 | 1·95 | 5·71 | 2·02 | 0·168 | 1·08 | 0·138 |
| Pr | 0·554 | 0·039 | 0·053 | 0·067 | 0·421 | 0·420 | 0·203 | 0·724 | 0·219 | 0·035 | 0·122 | 0·038 |
| Nd | 2·688 | 0·304 | 0·299 | 0·364 | 1·83 | 1·87 | 0·731 | 3·25 | 0·846 | 0·254 | 0·550 | 0·329 |
| Sm | 0·774 | 0·173 | 0·138 | 0·158 | 0·428 | 0·436 | 0·120 | 0·726 | 0·162 | 0·134 | 0·162 | 0·194 |
| Eu | 0·272 | 0·074 | 0·056 | 0·073 | 0·152 | 0·160 | 0·043 | 0·247 | 0·057 | 0·061 | 0·062 | 0·084 |
| Gd | 0·863 | 0·303 | 0·240 | 0·270 | 0·490 | 0·526 | 0·133 | 0·818 | 0·175 | 0·261 | 0·233 | 0·352 |
| Tb | 0·131 | 0·061 | 0·048 | 0·054 | 0·078 | 0·084 | 0·019 | 0·122 | 0·025 | 0·051 | 0·042 | 0·076 |
| Dy | 0·736 | 0·450 | 0·348 | 0·399 | 0·497 | 0·527 | 0·108 | 0·755 | 0·151 | 0·376 | 0·283 | 0·549 |
| Ho | 0·136 | 0·104 | 0·079 | 0·091 | 0·102 | 0·112 | 0·023 | 0·151 | 0·035 | 0·087 | 0·064 | 0·123 |
| Er | 0·335 | 0·318 | 0·251 | 0·274 | 0·304 | 0·315 | 0·068 | 0·420 | 0·101 | 0·261 | 0·194 | 0·373 |
| Tm | 0·041 | 0·045 | 0·038 | 0·042 | 0·042 | 0·043 | 0·010 | 0·059 | 0·014 | 0·039 | 0·028 | 0·057 |
| Yb | 0·246 | 0·328 | 0·268 | 0·284 | 0·291 | 0·297 | 0·070 | 0·405 | 0·097 | 0·277 | 0·194 | 0·375 |
| Lu | 0·034 | 0·049 | 0·043 | 0·047 | 0·044 | 0·044 | 0·011 | 0·057 | 0·016 | 0·044 | 0·030 | 0·059 |

(continued)

*Table 1: Continued*

| | SW13 | SW14 | SW15 | SW16 | SW16-R | SW17 | SW18 | SW19 | SW20 | SW21 | SW22 |
|---|---|---|---|---|---|---|---|---|---|---|---|
| Lithology: | Lz | Lz | Lz | Lz | | Lz | Lz | Lz | Lz | W | Lz |
| *Modal compositions (%)* | | | | | | | | | | | |
| Ol | 65·0 | 61·5 | 61·5 | 66·3 | | 57·8 | 71·6 | 60·3 | 73·1 | 63·5 | 61·3 |
| Opx | 22·1 | 21·4 | 23·7 | 22·7 | | 26·2 | 16·2 | 16·1 | 15·8 | 3·0 | 25·7 |
| Cpx | 10·3 | 14·3 | 13·3 | 9·6 | | 13·3 | 10·4 | 22·3 | 9·2 | 29·9 | 11·0 |
| Sp | 2·6 | 2·8 | 1·5 | 1·5 | | 2·7 | 1·8 | 1·3 | 2·0 | 3·6 | 2·1 |
| Fo | 90·6 | 90·0 | 90·8 | 91·0 | | 89·9 | 90·6 | 89·2 | 90·7 | | 89·8 |
| *Major elements (wt %)* | | | | | | | | | | | |
| $SiO_2$ | 44·3 | 43·8 | 44·6 | 44·3 | | 44·5 | 43·8 | 43·8 | 43·5 | 41·2 | 45·0 |
| $TiO_2$ | 0·07 | 0·10 | 0·06 | 0·03 | | 0·09 | 0·04 | 0·10 | 0·05 | 0·48 | 0·07 |
| $Al_2O_3$ | 2·70 | 3·40 | 2·39 | 2·05 | | 3·53 | 1·94 | 2·85 | 2·13 | 3·75 | 2·89 |
| $TFe_2O_3$ | 7·86 | 8·59 | 7·69 | 7·79 | | 8·51 | 8·17 | 9·06 | 8·08 | 14·3 | 8·67 |
| MnO | 0·10 | 0·12 | 0·09 | 0·10 | | 0·12 | 0·10 | 0·12 | 0·11 | 0·17 | 0·12 |
| MgO | 41·2 | 39·2 | 40·2 | 41·9 | | 39·0 | 42·5 | 36·8 | 42·8 | 32·7 | 39·8 |
| CaO | 2·31 | 2·83 | 2·84 | 2·09 | | 2·74 | 2·25 | 4·35 | 1·99 | 5·73 | 2·38 |
| $Na_2O$ | 0·13 | 0·14 | 0·11 | 0·11 | | 0·17 | 0·09 | 0·22 | 0·09 | 0·22 | 0·13 |
| $K_2O$ | 0·03 | 0·05 | 0·03 | 0·05 | | 0·08 | 0·03 | 0·05 | 0·03 | 0·07 | 0·05 |
| $P_2O_5$ | 0·03 | 0·03 | 0·06 | 0·02 | | 0·04 | 0·06 | 0·02 | 0·02 | 0·05 | 0·02 |
| LOI | 0·65 | 1·05 | 1·32 | 0·95 | | 0·67 | 0·42 | 2·03 | 0·68 | 0·92 | 0·38 |
| Total | 99·4 | 99·3 | 99·4 | 99·4 | | 99·4 | 99·4 | 99·4 | 99·4 | 99·5 | 99·5 |
| *Trace elements (ppm)* | | | | | | | | | | | |
| Ni | 2311 | 2094 | 2571 | 2219 | 2279 | 1829 | 2254 | 2089 | 2292 | 1324 | 1929 |
| Cu | 27·2 | 29·8 | 24·3 | 26·2 | 27·0 | 8·78 | 27·4 | 13·2 | 18·8 | 63·8 | 2·56 |
| Zn | 55·6 | 60·1 | 52·0 | 47·6 | 48·3 | 60·3 | 48·7 | 58·2 | 47·9 | 95·2 | 67·9 |
| Sr | 16·4 | 65·0 | 79·3 | 122 | 123 | 64·3 | 17·0 | 383 | 31·5 | 105 | 22·6 |
| Y | 2·33 | 2·86 | 1·90 | 1·18 | 1·19 | 3·12 | 1·47 | 3·20 | 1·73 | 4·22 | 2·20 |
| Zr | 3·75 | 5·17 | 3·62 | 2·85 | 2·87 | 7·33 | 3·62 | 7·35 | 2·08 | 18·8 | 4·31 |
| Nb | 0·318 | 0·490 | 0·134 | 0·664 | 0·670 | 1·01 | 0·027 | 0·545 | 0·034 | 1·40 | 0·237 |
| Ba | 1·45 | 1·30 | 1·08 | 2·23 | 2·28 | 4·69 | 0·480 | 1·69 | 0·348 | 6·97 | 0·920 |
| Hf | 0·116 | 0·151 | 0·086 | 0·054 | 0·049 | 0·216 | 0·079 | 0·199 | 0·083 | 0·725 | 0·131 |
| Ta | 0·011 | 0·026 | 0·004 | 0·041 | 0·039 | 0·061 | 0·001 | 0·031 | 0·001 | 0·091 | 0·015 |
| Pb | 0·410 | 0·331 | 0·108 | 0·392 | 0·383 | 0·143 | 0·106 | 0·299 | 0·053 | 0·604 | 0·057 |
| Th | 0·024 | 0·074 | 0·071 | 0·226 | 0·222 | 0·121 | 0·008 | 0·094 | 0·005 | 0·202 | 0·042 |
| U | 0·014 | 0·024 | 0·027 | 0·081 | 0·082 | 0·038 | 0·004 | 0·033 | 0·003 | 0·070 | 0·018 |
| S | 180 | 150 | 140 | 110 | | 60 | 230 | 100 | 160 | 510 | <50 |
| *Rare earth elements (ppm)* | | | | | | | | | | | |
| La | 0·188 | 1·59 | 0·397 | 1·01 | 0·999 | 2·11 | 0·144 | 0·902 | 0·032 | 2·94 | 0·786 |
| Ce | 0·466 | 3·52 | 0·758 | 2·12 | 2·09 | 5·01 | 0·533 | 1·86 | 0·149 | 6·60 | 1·88 |
| Pr | 0·075 | 0·422 | 0·094 | 0·226 | 0·217 | 0·621 | 0·093 | 0·225 | 0·038 | 0·859 | 0·239 |
| Nd | 0·450 | 1·78 | 0·457 | 0·814 | 0·801 | 2·67 | 0·532 | 1·02 | 0·266 | 4·20 | 1·09 |
| Sm | 0·194 | 0·425 | 0·147 | 0·159 | 0·150 | 0·595 | 0·168 | 0·314 | 0·128 | 1·16 | 0·287 |
| Eu | 0·076 | 0·148 | 0·058 | 0·054 | 0·053 | 0·209 | 0·060 | 0·122 | 0·057 | 0·409 | 0·106 |
| Gd | 0·303 | 0·503 | 0·228 | 0·187 | 0·182 | 0·663 | 0·222 | 0·472 | 0·235 | 1·34 | 0·371 |
| Tb | 0·058 | 0·084 | 0·041 | 0·033 | 0·031 | 0·106 | 0·040 | 0·083 | 0·046 | 0·195 | 0·067 |
| Dy | 0·418 | 0·540 | 0·290 | 0·224 | 0·219 | 0·663 | 0·279 | 0·586 | 0·329 | 1·10 | 0·439 |
| Ho | 0·092 | 0·115 | 0·064 | 0·052 | 0·051 | 0·138 | 0·064 | 0·127 | 0·075 | 0·197 | 0·097 |
| Er | 0·278 | 0·338 | 0·195 | 0·161 | 0·160 | 0·407 | 0·200 | 0·385 | 0·223 | 0·481 | 0·290 |
| Tm | 0·041 | 0·051 | 0·029 | 0·025 | 0·024 | 0·057 | 0·030 | 0·056 | 0·033 | 0·058 | 0·043 |
| Yb | 0·267 | 0·329 | 0·187 | 0·173 | 0·173 | 0·387 | 0·203 | 0·392 | 0·224 | 0·343 | 0·292 |
| Lu | 0·043 | 0·051 | 0·030 | 0·028 | 0·028 | 0·060 | 0·033 | 0·059 | 0·036 | 0·047 | 0·045 |

*Calculated using MINSQ (Hermann & Berry, 2002).
Lz, lherzolite; Hz, harzburgite; D, dunite; W, wehrlite; Px, pyroxenite; R, replicate analysis.

7500a system after digestion of samples using a mixture of ultra-pure HF and $HNO_3$ in Teflon bombs (see Appendix B for analytical details), also at the Institute of Geology and Geophysics, Chinese Academy of Sciences. Peridotite reference materials JP-1 and WPR-1 were measured to monitor the accuracy of the analytical procedure, and the results are in good agreement with reference values (Appendix B: Table B2). Precisions are generally better than 5% for most elements based on replicate analyses of several samples (e.g. SW16; see Table 1).

The major element compositions of minerals were measured at the Institute of Geology and Geophysics, Chinese Academy of Sciences using a JEOL-JXA8100 electron microprobe operated in wavelength-dispersive (WDS) mode. The operating conditions were as follows: 15 kV accelerating voltage, counting time of 20 s, and a 20 nA beam current. Natural minerals and synthetic oxides were used as standards, and a program based on the ZAF procedure was used for data correction.

Sulfur concentrations were determined at the National Research Center for Geoanalysis, Chinese Academy of Geological Sciences, using a high-frequency infrared absorption spectrometer (HIR-944B, Wuxi High-speed Analyzer Co., Ltd., China) (Shi *et al.*, 2001) (see Appendix B for method details). The quantification limit for S of the method was about 50 ppm. As Shi *et al.* (2001) reported, the analytical results for several Chinese rock reference materials using this method are comparable with their nominal values. Precisions are better than 3% for samples with S concentrations of >100 ppm and better than 10% for samples with S concentrations of <100 ppm.

## Clinopyroxene Sr–Nd–Hf isotope analyses

Strontium, Nd, and Hf isotope compositions of cpx separates from the Penglai and Shanwang peridotite xenoliths were determined at the State Key Laboratory of Lithospheric Evolution, Institute of Geology and Geophysics, Chinese Academy of Sciences. The mineral separates were washed with ultra-pure (Milli-Q) water, and ground to 200–400 mesh using an agate mortar before isotopic analysis. Analytical details for sample digestion and column separation procedures are described in Appendix B. For comparison, some cpx separates were treated with the following steps and then reanalyzed for Sr–Nd–Hf isotopes: (1) the separate was leached with 6M HCl at 100°C overnight; (2) the leached fraction was subsequently rinsed with Milli-Q water (18 MΩ) several times; (3) the leached fraction was ground to 200–400 mesh using an agate mortar.

The Rb–Sr and Sm–Nd isotopic analyses were conducted using a Finnigan MAT 262 thermal ionization mass spectrometer. Measured $^{87}Sr/^{86}Sr$ and $^{143}Nd/^{144}Nd$ ratios were corrected for mass-fractionation using $^{86}Sr/^{88}Sr = 0{\cdot}1194$ and $^{146}Nd/^{144}Nd = 0{\cdot}7219$, respectively. During the period of data collection, the measured values for the NBS-987 Sr standard and the JNdi-1 Nd standard were $^{87}Sr/^{86}Sr = 0{\cdot}710245 \pm 16$ ($2\sigma$, $n = 8$) and $^{143}Nd/^{144}Nd = 0{\cdot}512117 \pm 10$ ($2\sigma$, $n = 8$), respectively. Lutetium and Hf were measured using a ThermoElectron Neptune multi-collector ICP-MS system. Hafnium isotopic ratios were normalized to $^{179}Hf/^{177}Hf = 0{\cdot}7325$ and $^{176}Lu/^{175}Lu$ isotopic ratios were normalized using Yb isotopic ratios. During the analytical campaign, an Alfa Hf standard was measured 10 times and the average value of $^{176}Hf/^{177}Hf$ was $0{\cdot}282179 \pm 4$ ($2\sigma$). The USGS reference material BCR-2 was measured for Rb–Sr, Sm–Nd and Lu–Hf isotopic composition to monitor the accuracy of the analytical procedures, with the following results: 46·54 ppm Rb, 339·7 ppm Sr, $^{87}Sr/^{86}Sr = 0{\cdot}704986 \pm 13$ ($2\sigma$), 6·676 ppm Sm, 28·04 ppm Nd, $^{143}Nd/^{144}Nd = 0{\cdot}512623 \pm 13$ ($2\sigma$), and 0·5175 ppm Lu, 4·912 ppm Hf, $^{176}Hf/^{177}Hf = 0{\cdot}282830 \pm 4$ ($2\sigma$). These values are comparable with the reported reference values (GeoREM, http://georem.mpch-mainz.gwdg.de/). The procedural blanks were about 40 pg for Rb, 300 pg for Sr, 20 pg for Sm, 60 pg for Nd, 20 pg for Lu and 40 pg for Hf. With the exception of sample PL19, which has an Hf blank to sample ratio of about 0·5%, of which $^{176}Hf/^{177}Hf$ is blank-corrected, maximum blank to sample ratios are 0·02% for Sr (PL11), 0·09% for Nd (PL11) and 0·4% for Hf (PL11), requiring no correction of the measured isotopic ratios.

## Re–Os and PGE analyses

Re–Os isotopic compositions and PGE abundances were determined at both the State Key Laboratory of Lithospheric Evolution, Institute of Geology and Geophysics, Chinese Academy of Sciences (IGGCAS) and the Isotope Geochemistry Laboratory, University of Maryland (UMD). Some samples were analyzed in both laboratories for comparison. As shown in Appendix B (Fig. B1), the results from the two laboratories are in good agreement for Os isotopic compositions.

The methods used at both laboratories are similar to those described by Shirey & Walker (1995), Pearson & Woodland (2000) and Walker *et al.* (2008). Rhenium, Os, Ir, Ru, Pt, Pd concentrations and Os isotopic compositions were obtained from the same Carius tube sample digestion (for details of Re–Os and PGE chemistry see Appendix B).

Osmium isotopic compositions were measured by negative thermal ionization using either a GV Isoprobe-T mass spectrometer at IGGCAS (Chu *et al.*, 2007), or a VG Sector 54 mass spectrometer at UMD (Walker *et al.*, 2002, 2008). For these measurements, purified Os was loaded onto platinum filaments and $Ba(OH)_2$ was used as an ion emitter. At IGGCAS, all samples were run in static mode using Faraday cups. At UMD, samples were run in static mode on Faraday cups, or in peak-jumping mode with a single electron multiplier, depending on the amount of Os. The measured Os isotopic ratios were corrected for mass

fractionation using $^{192}Os/^{188}Os = 3{\cdot}0827$. The in-run precisions for Os isotopic measurements were better than $\pm 0{\cdot}2\%$ (2RSD) for all the samples. During the period of measurements of our samples, the $^{187}Os/^{188}Os$ ratio of the Johnson–Matthey standard of UMD was $0{\cdot}11380 \pm 4$ ($2\sigma$, $n = 5$) at IGGCAS, and $0{\cdot}11379 \pm 2$ ($2\sigma$, $n=5$) for Faraday cups and $0{\cdot}1138 \pm 1$ ($2\sigma$, $n = 5$) for electron multiplier at UMD.

The isotope dilution analyses of Re, Ir, Ru, Pt, and Pd were conducted either at IGGCAS using a Thermo-Electron Neptune MC-ICP-MS system with an electron multiplier in peak-jumping mode or using Faraday cups in static mode, according to the measured signal intensity, or at UMD using a Nu-Plasma MC-ICP-MS system with a triple electron multiplier configuration in static mode. Mass fractionations (and gain effects of different multipliers for the UMD method) for Re, Ir, Ru, Pt, and Pd were corrected using Re, Ir, Ru, Pt and Pd standards that were interspersed with the samples. In-run precisions for $^{185}Re/^{187}Re$, $^{191}Ir/^{193}Ir$, $^{194}Pt/^{196}Pt$, $^{105}Pd/^{106}Pd$, and $^{99}Ru/^{101}Ru$ were typically 0·1–0·3% (2RSD).

## RESULTS

### Major element geochemistry

The intense serpentinization of the five xenoliths from the Mengyin diamondiferous kimberlites is reflected in the high loss-on-ignition values (LOI; from 10·5 to 14·0%) (Table 1). Sample MY35 is characterized by high $Al_2O_3$, $Fe_2O_3$ and CaO contents, and relatively low MgO content, indicating that this sample may have originally been a pyroxenite. The other four samples have relatively low $Al_2O_3$ and CaO contents. Whole-rock compositions normalized to 100% volatile-free are refractory, with CaO ranging from 0·2 to 0·75 wt %, and $Al_2O_3$ from 0·07 to 0·37 wt %, similar to accepted values for the Archean cratonic mantle (e.g. Lee & Rudnick, 1999; Carlson *et al.*, 2005). The Mg-number of the whole-rocks ranges from 91·9 to 95·2, with samples MY9 and MY34 having the highest whole-rock Mg-number, close to 95. Sulfur concentrations in the Mengyin xenoliths are relatively high (from 140 to 510 ppm, Table 1).

The 17 Penglai peridotites have low LOI values, from −0·3 to 0·5 wt %, consistent with the generally low degrees of alteration of the xenoliths (Table 1, Fig. 2). Some samples have negative LOI values, indicating that oxidation of FeO to $Fe_2O_3$ was more significant than loss of volatiles. Whole-rocks are relatively fertile, with $Al_2O_3$ ranging from 1·2 to 4·3 wt %, and CaO ranging from 1·0 to 3·3 wt %. Most samples lie near the oceanic trend of Boyd (1989) (Fig. 3), which is considered typical of post-Archean peridotites. Except for PL03, $Al_2O_3$ and CaO show well-defined negative correlations with MgO content (Fig. 4a and b). There are also negative correlations between the $Al_2O_3$ content in whole-rocks and Fo and Cr-number values of olivine and spinel (not shown). Sulfur concentrations in most Penglai samples are <50 ppm (the quantification limit), except for samples PL03 and PL16, which have S concentrations of 260 and 60 ppm, respectively (Table 1).

The 22 Shanwang xenoliths also have relatively low LOI (from 0·4 to 2·5 wt %, Table 1), except for sample SW04, for which LOI was 9·7 wt %. Whole-rock xenoliths show variable fertility, as reflected by their $Al_2O_3$ contents, which range from 1·2 to 3·8 wt %, and CaO contents, which range from 1·1 to 5·7 wt %. Again, most samples lie near the oceanic trend of Boyd (1989) (Fig. 3). $Al_2O_3$ and CaO contents correlate negatively with the MgO content, except for samples SW01, SW04 and SW21 (Fig. 4c and d). The latter samples have high CaO and relatively low MgO contents, reflecting their pyroxene-rich compositions (they are pyroxenites or wehrlites). Except for these samples, the negative linear correlations between the $Al_2O_3$ content of whole-rocks and Fo and Cr-number values of olivine and spinel are also reasonably good (not shown). Sulfur contents are generally higher than those of Penglai (Table 1), with the wehrlite sample SW21 having the highest S content of 510 ppm.

### Mineral chemistry and equilibration temperatures

Major element compositions of minerals from Penglai and Shanwang are provided in Table 2. Overall, olivines have Fo-numbers ranging from 86·1 to 91·3 (Fig. 3). The Fo-numbers of olivines from the Penglai peridotites range from 88·1 to 91·3 (Table 2), with only two samples (PL03 and PL16) having Fo-numbers lower than 89. Olivines from the Shanwang xenoliths exhibit a similar range in Fo (89·0–91·0), with the exception of two samples having very low Fo (Fe-rich lherzolite SW05, with Fo of 86·1, and wehrlite SW21, with Fo of 81·8). Generally, the mineral modes and Fo compositions indicate that the Penglai and Shanwang peridotites are relatively fertile lherzolites. They are, thus, comparable with peridotite xenoliths from other Cenozoic locales in eastern China and distinct from the very refractory xenoliths present in the Paleozoic Mengyin and Fuxian kimberlites (Fan *et al.*, 2000; Rudnick *et al.*, 2004; Zheng *et al.*, 2007) (Fig. 3).

The Cr-number of spinels from the Penglai and Shanwang xenoliths range from 9·53 to 39·4 and from 9·03 to 28·4, respectively (Table 2), never reaching the high Cr-number of spinels that are typical of cratonic peridotites and inclusions in diamonds (Cr-number >60, e.g. Lee & Rudnick, 1999), as well as chromites from the Paleozoic kimberlites from eastern China (Zheng, 1999).

The equilibration temperatures of the mantle xenoliths from Penglai and Shanwang can be constrained via application of various geothermometers (Wood & Banno, 1973; Wells, 1977; Bertrand & Mercier, 1985; Brey & Kohler,

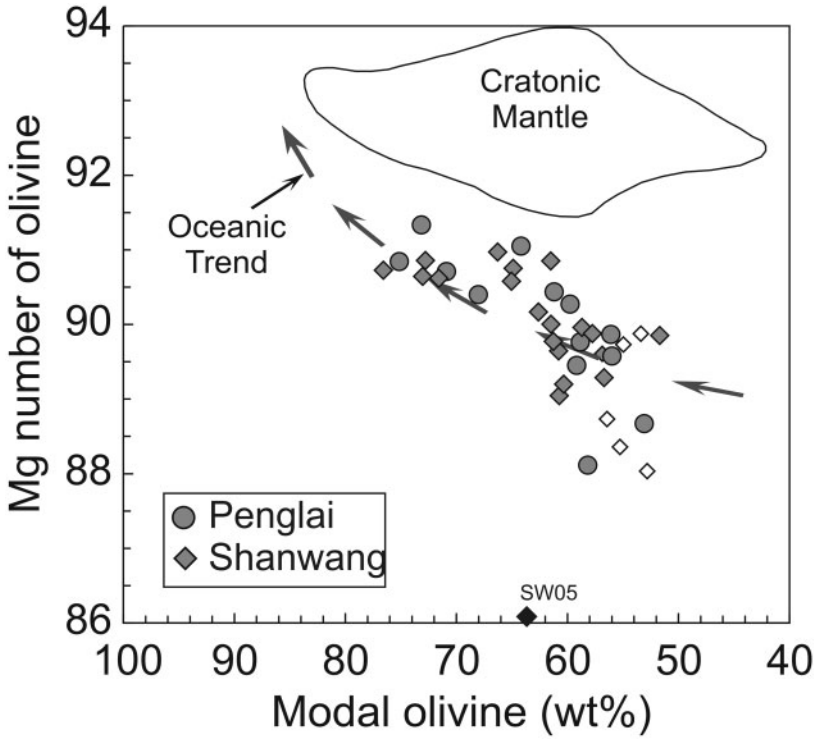


**Fig. 3.** Modal olivine vs Mg-number of olivine in peridotites after Boyd (1989). Black diamond, Fe-rich lherzolite SW05 from Shanwang; small open diamonds, literature data for Shanwang garnet-lherzolites from Zheng *et al.* (2006).

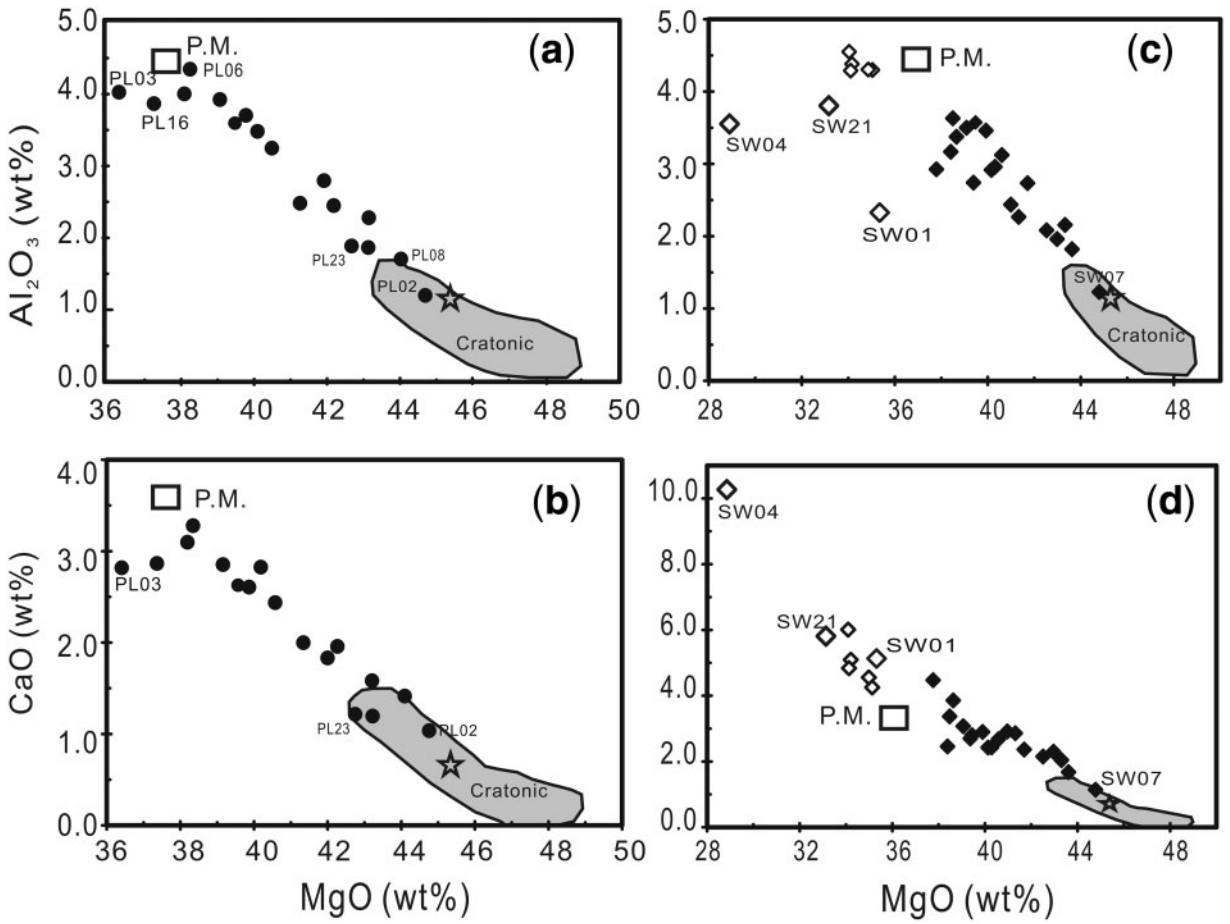


**Fig. 4.** Whole-rock $Al_2O_3$ and CaO vs MgO contents for Penglai (a, b) and Shanwang (c, d) peridotites. Large open diamonds, wehrlites and pyroxenites from Shanwang; small open diamonds, literature data for Shanwang peridotites from Zheng *et al.* (2005); P.M., Primitive mantle (McDonough & Sun, 1995); star, average peridotitic xenoliths from Archean cratons (Griffin *et al.*, 1999); gray field represents cratonic peridotite xenoliths from the Tanzanian craton (Lee & Rudnick, 1999).

*Table 2: Mineral compositions of peridotites from Penglai and Shanwang (n = 3)*

| Sample | Mineral | $SiO_2$ | $TiO_2$ | $Cr_2O_3$ | $Al_2O_3$ | FeO | NiO | MnO | MgO | CaO | $Na_2O$ | $K_2O$ | Total |
|---|---|---|---|---|---|---|---|---|---|---|---|---|---|
| PL01 | Ol | 41·12 | 0·00 | 0·01 | 0·00 | 9·88 | 0·40 | 0·14 | 48·62 | 0·04 | 0·01 | 0·00 | 100·22 |
| | Opx | 55·59 | 0·09 | 0·31 | 4·09 | 6·28 | 0·07 | 0·14 | 32·53 | 0·52 | 0·10 | 0·01 | 99·74 |
| | Cpx | 52·35 | 0·54 | 0·87 | 7·04 | 2·68 | 0·04 | 0·10 | 14·25 | 19·68 | 2·12 | 0·00 | 99·68 |
| | Sp | 0·01 | 0·09 | 10·14 | 56·43 | 10·77 | 0·37 | 0·12 | 20·12 | 0·00 | 0·00 | 0·01 | 98·05 |
| PL02 | Ol | 41·02 | 0·00 | 0·02 | 0·00 | 8·80 | 0·36 | 0·12 | 49·00 | 0·04 | 0·02 | 0·00 | 99·38 |
| | Opx | 56·28 | 0·06 | 0·58 | 2·67 | 5·58 | 0·09 | 0·12 | 33·37 | 0·69 | 0·06 | 0·00 | 99·48 |
| | Cpx | 53·40 | 0·13 | 1·04 | 3·11 | 2·37 | 0·05 | 0·09 | 16·54 | 21·79 | 0·78 | 0·00 | 99·29 |
| | Sp | 0·06 | 0·66 | 32·34 | 33·43 | 15·95 | 0·19 | 0·22 | 15·74 | 0·00 | 0·03 | 0·00 | 98·63 |
| PL03 | Ol | 40·71 | 0·01 | 0·01 | 0·01 | 10·81 | 0·37 | 0·16 | 47·45 | 0·07 | 0·00 | 0·00 | 99·60 |
| | Opx | 54·46 | 0·08 | 0·40 | 5·27 | 6·84 | 0·07 | 0·18 | 30·65 | 0·85 | 0·32 | 0·01 | 99·11 |
| | Cpx | 52·09 | 0·47 | 0·78 | 7·05 | 3·36 | 0·04 | 0·10 | 14·61 | 18·33 | 2·28 | 0·00 | 99·10 |
| | Sp | 0·04 | 0·12 | 10·50 | 54·35 | 12·56 | 0·37 | 0·13 | 19·61 | 0·01 | 0·00 | 0·00 | 97·70 |
| PL06 | Ol | 41·02 | 0·01 | 0·00 | 0·01 | 9·73 | 0·38 | 0·13 | 48·41 | 0·02 | 0·00 | 0·01 | 99·72 |
| | Opx | 54·85 | 0·15 | 0·28 | 4·30 | 6·05 | 0·09 | 0·15 | 32·14 | 0·59 | 0·11 | 0·00 | 98·71 |
| | Cpx | 52·08 | 0·59 | 0·71 | 6·73 | 2·60 | 0·02 | 0·10 | 14·49 | 19·76 | 1·92 | 0·01 | 99·01 |
| | Sp | 0·02 | 0·09 | 9·01 | 57·37 | 10·10 | 0·39 | 0·13 | 20·66 | 0·00 | 0·00 | 0·00 | 97·78 |
| PL07 | Ol | 40·79 | 0·02 | 0·00 | 0·06 | 9·91 | 0·36 | 0·14 | 47·76 | 0·04 | 0·01 | 0·01 | 99·08 |
| | Opx | 55·15 | 0·11 | 0·32 | 4·46 | 6·35 | 0·10 | 0·12 | 32·08 | 0·61 | 0·09 | 0·00 | 99·40 |
| | Cpx | 53·07 | 0·53 | 0·70 | 6·95 | 2·67 | 0·05 | 0·09 | 15·07 | 19·02 | 1·60 | 0·00 | 99·76 |
| | Sp | 0·09 | 0·09 | 9·06 | 57·16 | 10·20 | 0·40 | 0·12 | 20·10 | 0·00 | 0·02 | 0·00 | 97·24 |
| PL08 | Ol | 41·33 | 0·00 | 0·01 | 0·00 | 8·38 | 0·36 | 0·11 | 49·53 | 0·04 | 0·01 | 0·00 | 99·77 |
| | Opx | 56·29 | 0·03 | 0·50 | 3·34 | 5·30 | 0·07 | 0·16 | 33·41 | 0·65 | 0·07 | 0·00 | 99·80 |
| | Cpx | 53·06 | 0·16 | 1·16 | 4·54 | 2·12 | 0·04 | 0·06 | 15·68 | 21·26 | 1·27 | 0·00 | 99·34 |
| | Sp | 0·03 | 0·09 | 21·64 | 46·50 | 10·47 | 0·29 | 0·15 | 19·19 | 0·01 | 0·01 | 0·00 | 98·38 |
| PL13 | Ol | 40·85 | 0·01 | 0·00 | 0·00 | 10·08 | 0·36 | 0·15 | 47·96 | 0·01 | 0·02 | 0·00 | 99·45 |
| | Opx | 55·77 | 0·10 | 0·25 | 3·79 | 6·41 | 0·08 | 0·17 | 32·57 | 0·45 | 0·08 | 0·00 | 99·66 |
| | Cpx | 51·91 | 0·63 | 0·78 | 6·71 | 2·50 | 0·04 | 0·08 | 14·00 | 20·24 | 2·00 | 0·01 | 98·89 |
| | Sp | 0·02 | 0·07 | 9·18 | 57·18 | 10·82 | 0·36 | 0·13 | 19·90 | 0·00 | 0·01 | 0·00 | 97·67 |
| PL14 | Ol | 40·89 | 0·00 | 0·03 | 0·01 | 9·18 | 0·39 | 0·12 | 48·71 | 0·04 | 0·00 | 0·00 | 99·36 |
| | Opx | 55·31 | 0·07 | 0·45 | 4·20 | 5·84 | 0·07 | 0·13 | 32·42 | 0·66 | 0·11 | 0·00 | 99·26 |
| | Cpx | 52·61 | 0·45 | 0·98 | 6·11 | 2·36 | 0·03 | 0·08 | 14·89 | 20·05 | 1·83 | 0·00 | 99·40 |
| | Sp | 0·04 | 0·09 | 13·98 | 53·31 | 10·04 | 0·32 | 0·11 | 19·92 | 0·00 | 0·01 | 0·01 | 97·84 |
| PL16 | Ol | 40·64 | 0·01 | 0·02 | 0·02 | 11·31 | 0·29 | 0·14 | 47·06 | 0·05 | 0·01 | 0·00 | 99·54 |
| | Opx | 54·41 | 0·15 | 0·41 | 5·15 | 7·02 | 0·10 | 0·15 | 30·76 | 0·88 | 0·16 | 0·00 | 99·19 |
| | Cpx | 52·13 | 0·53 | 0·80 | 7·16 | 3·53 | 0·05 | 0·10 | 14·77 | 18·34 | 2·20 | 0·01 | 99·62 |
| | Sp | 0·07 | 0·19 | 10·28 | 54·33 | 12·17 | 0·28 | 0·13 | 19·69 | 0·00 | 0·01 | 0·00 | 97·15 |
| PL17 | Ol | 41·02 | 0·01 | 0·02 | 0·02 | 9·30 | 0·36 | 0·13 | 48·41 | 0·04 | 0·00 | 0·01 | 99·29 |
| | Opx | 55·13 | 0·06 | 0·39 | 4·21 | 5·92 | 0·10 | 0·16 | 32·07 | 0·65 | 0·11 | 0·00 | 98·80 |
| | Cpx | 52·40 | 0·30 | 0·80 | 5·71 | 2·54 | 0·04 | 0·10 | 15·25 | 20·32 | 1·43 | 0·00 | 98·89 |
| | Sp | 0·03 | 0·04 | 12·02 | 54·63 | 10·20 | 0·33 | 0·12 | 20·01 | 0·00 | 0·02 | 0·01 | 97·40 |
| PL18 | Ol | 41·05 | 0·00 | 0·02 | 0·01 | 8·91 | 0·40 | 0·13 | 48·81 | 0·04 | 0·01 | 0·00 | 99·37 |
| | Opx | 55·68 | 0·06 | 0·48 | 3·55 | 5·60 | 0·10 | 0·15 | 32·73 | 0·66 | 0·06 | 0·01 | 99·07 |
| | Cpx | 52·83 | 0·22 | 1·04 | 4·53 | 2·34 | 0·02 | 0·08 | 15·85 | 21·25 | 1·09 | 0·01 | 99·28 |
| | Sp | 0·01 | 0·08 | 20·34 | 47·17 | 10·75 | 0·31 | 0·14 | 18·94 | 0·00 | 0·00 | 0·00 | 97·72 |
| PL19 | Ol | 40·98 | 0·01 | 0·01 | 0·00 | 9·20 | 0·41 | 0·14 | 48·63 | 0·05 | 0·00 | 0·00 | 99·44 |
| | Opx | 55·39 | 0·01 | 0·40 | 3·68 | 5·81 | 0·08 | 0·14 | 32·33 | 0·62 | 0·08 | 0·01 | 98·54 |
| | Cpx | 53·58 | 0·04 | 0·74 | 4·61 | 2·41 | 0·05 | 0·09 | 15·87 | 20·93 | 1·36 | 0·01 | 99·68 |
| | Sp | 0·06 | 0·01 | 16·95 | 48·55 | 14·47 | 0·29 | 0·18 | 17·16 | 0·01 | 0·00 | 0·01 | 97·70 |

(continued)

*Table 2: Continued*

| Sample | Mineral | $SiO_2$ | $TiO_2$ | $Cr_2O_3$ | $Al_2O_3$ | FeO | NiO | MnO | MgO | CaO | $Na_2O$ | $K_2O$ | Total |
|---|---|---|---|---|---|---|---|---|---|---|---|---|---|
| PL23 | Ol | 41·23 | 0·00 | 0·00 | 0·01 | 8·58 | 0·40 | 0·13 | 48·98 | 0·04 | 0·01 | 0·00 | 99·40 |
| | Opx | 56·69 | 0·02 | 0·44 | 2·38 | 5·60 | 0·09 | 0·12 | 33·58 | 0·53 | 0·01 | 0·00 | 99·46 |
| | Cpx | 53·41 | 0·06 | 0·73 | 2·49 | 2·02 | 0·04 | 0·09 | 16·66 | 22·88 | 0·46 | 0·01 | 98·85 |
| | Sp | 0·02 | 6·55 | 19·37 | 20·39 | 42·66 | 0·10 | 0·45 | 8·26 | 0·00 | 0·01 | 0·00 | 97·80 |
| SW02 | Ol | 41·01 | 0·00 | 0·00 | 0·01 | 9·65 | 0·37 | 0·14 | 48·52 | 0·02 | 0·01 | 0·00 | 99·75 |
| | Opx | 55·43 | 0·08 | 0·29 | 3·74 | 6·20 | 0·11 | 0·16 | 32·58 | 0·42 | 0·05 | 0·00 | 99·06 |
| | Cpx | 52·62 | 0·49 | 0·70 | 5·97 | 2·30 | 0·04 | 0·10 | 14·55 | 20·95 | 1·79 | 0·00 | 99·50 |
| | Sp | 0·02 | 0·02 | 9·91 | 57·41 | 10·19 | 0·35 | 0·11 | 19·82 | 0·00 | 0·01 | 0·00 | 97·83 |
| SW03 | Ol | 40·84 | 0·00 | 0·01 | 0·00 | 9·77 | 0·35 | 0·13 | 48·54 | 0·01 | 0·01 | 0·00 | 99·65 |
| | Opx | 55·79 | 0·07 | 0·26 | 3·61 | 6·36 | 0·11 | 0·15 | 32·66 | 0·44 | 0·04 | 0·00 | 99·51 |
| | Cpx | 52·61 | 0·42 | 0·73 | 6·37 | 2·41 | 0·05 | 0·07 | 14·26 | 20·72 | 1·81 | 0·00 | 99·44 |
| | Sp | 0·09 | 0·03 | 9·02 | 57·36 | 10·05 | 0·35 | 0·11 | 20·11 | 0·01 | 0·02 | 0·01 | 97·16 |
| SW04 | Ol | 40·96 | 0·00 | 0·01 | 0·01 | 9·31 | 0·37 | 0·15 | 48·55 | 0·01 | 0·03 | 0·00 | 99·40 |
| | Opx | 55·07 | 0·09 | 0·43 | 4·41 | 6·03 | 0·08 | 0·16 | 32·59 | 0·47 | 0·05 | 0·01 | 99·40 |
| | Cpx | 52·33 | 0·39 | 0·83 | 5·93 | 2·35 | 0·04 | 0·08 | 14·85 | 20·67 | 1·64 | 0·00 | 99·13 |
| | Sp | 0·03 | 0·07 | 11·36 | 55·89 | 9·89 | 0·35 | 0·11 | 19·92 | 0·00 | 0·01 | 0·00 | 97·64 |
| SW05 | Ol | 40·33 | 0·00 | 0·01 | 0·02 | 13·27 | 0·34 | 0·22 | 46·06 | 0·05 | 0·01 | 0·01 | 100·31 |
| | Opx | 55·09 | 0·10 | 0·38 | 3·93 | 8·09 | 0·08 | 0·21 | 31·10 | 0·61 | 0·13 | 0·01 | 99·72 |
| | Cpx | 52·66 | 0·40 | 0·81 | 4·21 | 2·93 | 0·04 | 0·07 | 15·76 | 21·04 | 1·25 | 0·01 | 99·19 |
| | Sp | 0·01 | 0·03 | 11·98 | 54·03 | 11·91 | 0·38 | 0·12 | 19·41 | 0·01 | 0·03 | 0·00 | 97·91 |
| SW06 | Ol | 40·43 | 0·00 | 0·00 | 0·01 | 9·88 | 0·36 | 0·16 | 48·00 | 0·05 | 0·00 | 0·00 | 98·89 |
| | Opx | 54·64 | 0·11 | 0·34 | 4·16 | 6·05 | 0·13 | 0·16 | 32·22 | 0·63 | 0·10 | 0·00 | 98·55 |
| | Cpx | 52·16 | 0·60 | 0·91 | 6·59 | 2·50 | 0·06 | 0·09 | 14·54 | 19·74 | 1·99 | 0·01 | 99·19 |
| | Sp | 0·01 | 0·13 | 11·70 | 54·34 | 10·72 | 0·38 | 0·11 | 20·01 | 0·01 | 0·01 | 0·00 | 97·40 |
| SW07 | Ol | 40·64 | 0·00 | 0·02 | 0·00 | 8·89 | 0·37 | 0·13 | 48·77 | 0·03 | 0·02 | 0·01 | 98·89 |
| | Opx | 56·12 | 0·06 | 0·53 | 3·29 | 5·74 | 0·04 | 0·13 | 32·92 | 0·61 | 0·15 | 0·00 | 99·61 |
| | Cpx | 53·51 | 0·16 | 1·40 | 4·85 | 2·46 | 0·04 | 0·09 | 15·24 | 19·12 | 2·19 | 0·00 | 99·06 |
| | Sp | 0·03 | 0·15 | 25·10 | 42·43 | 11·80 | 0·24 | 0·19 | 17·76 | 0·00 | 0·01 | 0·00 | 97·72 |
| SW08 | Ol | 40·84 | 0·01 | 0·02 | 0·00 | 10·49 | 0·38 | 0·15 | 47·84 | 0·05 | 0·03 | 0·01 | 99·83 |
| | Opx | 54·82 | 0·10 | 0·28 | 4·43 | 6·62 | 0·10 | 0·15 | 31·80 | 0·66 | 0·13 | 0·01 | 99·08 |
| | Cpx | 51·59 | 0·58 | 0·70 | 6·59 | 2·81 | 0·05 | 0·09 | 14·54 | 19·67 | 1·97 | 0·03 | 98·63 |
| | Sp | 0·02 | 0·04 | 9·07 | 56·84 | 10·85 | 0·38 | 0·12 | 20·06 | 0·00 | 0·01 | 0·01 | 97·40 |
| SW09 | Ol | 41·47 | 0·02 | 0·03 | 0·01 | 8·87 | 0·36 | 0·12 | 49·44 | 0·08 | 0·04 | 0·00 | 100·45 |
| | Opx | 55·64 | 0·06 | 0·55 | 3·30 | 5·58 | 0·08 | 0·14 | 33·23 | 0·65 | 0·14 | 0·01 | 99·36 |
| | Cpx | 53·72 | 0·13 | 1·39 | 5·04 | 2·41 | 0·04 | 0·08 | 15·37 | 19·09 | 2·16 | 0·00 | 99·45 |
| | Sp | 0·08 | 0·20 | 23·56 | 44·05 | 11·34 | 0·27 | 0·18 | 18·72 | 0·00 | 0·02 | 0·00 | 98·42 |
| SW10 | Ol | 41·53 | 0·01 | 0·02 | 0·01 | 9·54 | 0·38 | 0·14 | 49·08 | 0·03 | 0·01 | 0·01 | 100·75 |
| | Opx | 55·98 | 0·03 | 0·27 | 3·41 | 6·14 | 0·12 | 0·13 | 33·06 | 0·32 | 0·03 | 0·00 | 99·49 |
| | Cpx | 52·36 | 0·43 | 0·74 | 5·84 | 2·34 | 0·03 | 0·08 | 14·40 | 20·89 | 1·76 | 0·00 | 98·88 |
| | Sp | 0·06 | 0·03 | 10·24 | 56·66 | 9·98 | 0·35 | 0·10 | 19·83 | 0·01 | 0·00 | 0·00 | 97·28 |
| SW11 | Ol | 40·92 | 0·00 | 0·02 | 0·00 | 8·94 | 0·39 | 0·13 | 49·23 | 0·05 | 0·02 | 0·00 | 99·69 |
| | Opx | 55·46 | 0·10 | 0·43 | 3·75 | 5·65 | 0·11 | 0·12 | 32·91 | 0·63 | 0·09 | 0·01 | 99·27 |
| | Cpx | 52·37 | 0·44 | 1·02 | 5·52 | 2·35 | 0·05 | 0·08 | 15·18 | 20·70 | 1·65 | 0·01 | 99·37 |
| | Sp | 0·02 | 0·13 | 16·35 | 51·22 | 10·46 | 0·30 | 0·13 | 19·99 | 0·00 | 0·02 | 0·01 | 98·63 |
| SW12 | Ol | 40·84 | 0·01 | 0·01 | 0·00 | 10·29 | 0·36 | 0·18 | 48·10 | 0·02 | 0·01 | 0·00 | 99·81 |
| | Opx | 55·81 | 0·08 | 0·25 | 3·89 | 6·67 | 0·06 | 0·13 | 32·57 | 0·44 | 0·03 | 0·01 | 99·93 |
| | Cpx | 0·00 | 0·01 | 8·57 | 57·91 | 10·39 | 0·36 | 0·09 | 20·18 | 0·01 | 0·01 | 0·01 | 97·54 |
| | Sp | 52·19 | 0·48 | 0·63 | 6·21 | 2·45 | 0·04 | 0·09 | 14·56 | 21·08 | 1·69 | 0·01 | 99·43 |

(continued)

*Table 2: Continued*

| Sample | Mineral | $SiO_2$ | $TiO_2$ | $Cr_2O_3$ | $Al_2O_3$ | FeO | NiO | MnO | MgO | CaO | $Na_2O$ | $K_2O$ | Total |
|---|---|---|---|---|---|---|---|---|---|---|---|---|---|
| SW13 | Ol | 41·25 | 0·00 | 0·01 | 0·01 | 9·10 | 0·34 | 0·13 | 49·11 | 0·01 | 0·01 | 0·00 | 99·97 |
| | Opx | 55·43 | 0·10 | 0·39 | 3·41 | 5·83 | 0·09 | 0·14 | 33·35 | 0·39 | 0·06 | 0·01 | 99·20 |
| | Cpx | 52·41 | 0·51 | 0·94 | 5·64 | 2·06 | 0·05 | 0·06 | 14·79 | 21·44 | 1·77 | 0·01 | 99·70 |
| | Sp | 0·01 | 0·09 | 14·24 | 53·61 | 10·07 | 0·32 | 0·11 | 19·72 | 0·00 | 0·01 | 0·01 | 98·19 |
| SW14 | Ol | 40·97 | 0·00 | 0·03 | 0·03 | 9·71 | 0·37 | 0·13 | 49·04 | 0·07 | 0·00 | 0·00 | 100·35 |
| | Opx | 55·32 | 0·13 | 0·34 | 4·18 | 6·20 | 0·10 | 0·15 | 32·55 | 0·62 | 0·12 | 0·01 | 99·72 |
| | Cpx | 52·66 | 0·42 | 0·79 | 6·65 | 2·89 | 0·04 | 0·12 | 15·54 | 18·83 | 1·84 | 0·00 | 99·77 |
| | Sp | 0·03 | 0·15 | 10·41 | 56·21 | 10·55 | 0·35 | 0·12 | 20·40 | 0·01 | 0·02 | 0·00 | 98·25 |
| SW15 | Ol | 41·33 | 0·01 | 0·01 | 0·01 | 9·01 | 0·38 | 0·12 | 50·20 | 0·04 | 0·00 | 0·00 | 101·11 |
| | Opx | 56·04 | 0·07 | 0·41 | 3·87 | 5·66 | 0·09 | 0·15 | 33·69 | 0·63 | 0·10 | 0·01 | 100·73 |
| | Cpx | 52·69 | 0·39 | 1·05 | 5·70 | 2·37 | 0·06 | 0·09 | 15·41 | 20·48 | 1·66 | 0·01 | 99·91 |
| | Sp | 0·04 | 0·12 | 16·22 | 52·20 | 10·41 | 0·32 | 0·13 | 20·31 | 0·00 | 0·01 | 0·01 | 99·76 |
| SW16 | Ol | 41·46 | 0·00 | 0·01 | 0·00 | 8·91 | 0·37 | 0·13 | 50·37 | 0·04 | 0·02 | 0·00 | 101·33 |
| | Opx | 56·23 | 0·05 | 0·45 | 3·69 | 5·48 | 0·09 | 0·11 | 33·66 | 0·62 | 0·13 | 0·01 | 100·51 |
| | Cpx | 53·20 | 0·22 | 1·06 | 5·27 | 2·13 | 0·02 | 0·08 | 15·52 | 20·47 | 1·74 | 0·01 | 99·70 |
| | Sp | 0·04 | 0·07 | 17·24 | 51·73 | 10·20 | 0·29 | 0·14 | 20·34 | 0·00 | 0·01 | 0·00 | 100·06 |
| SW17 | Ol | 41·12 | 0·00 | 0·00 | 0·00 | 9·91 | 0·39 | 0·14 | 49·37 | 0·06 | 0·01 | 0·02 | 101·02 |
| | Opx | 55·34 | 0·08 | 0·32 | 4·43 | 6·38 | 0·10 | 0·16 | 32·74 | 0·60 | 0·13 | 0·00 | 100·28 |
| | Cpx | 52·62 | 0·39 | 0·66 | 6·49 | 2·73 | 0·05 | 0·10 | 15·02 | 19·45 | 2·11 | 0·01 | 99·62 |
| | Sp | 0·02 | 0·06 | 9·99 | 57·88 | 10·60 | 0·39 | 0·11 | 20·77 | 0·00 | 0·01 | 0·01 | 99·84 |
| SW18 | Ol | 41·70 | 0·00 | 0·01 | 0·00 | 9·25 | 0·38 | 0·15 | 50·13 | 0·01 | 0·00 | 0·00 | 101·63 |
| | Opx | 56·55 | 0·07 | 0·40 | 3·23 | 5·91 | 0·07 | 0·15 | 33·91 | 0·40 | 0·04 | 0·00 | 100·74 |
| | Cpx | 53·53 | 0·34 | 1·01 | 5·08 | 2·35 | 0·04 | 0·06 | 15·33 | 21·39 | 1·55 | 0·00 | 100·67 |
| | Sp | 0·06 | 0·03 | 17·49 | 51·09 | 10·86 | 0·30 | 0·13 | 19·56 | 0·01 | 0·02 | 0·00 | 99·54 |
| SW19 | Ol | 41·16 | 0·00 | 0·02 | 0·01 | 10·50 | 0·37 | 0·13 | 48·65 | 0·03 | 0·01 | 0·01 | 100·87 |
| | Opx | 55·53 | 0·09 | 0·32 | 4·57 | 6·51 | 0·08 | 0·15 | 32·47 | 0·62 | 0·10 | 0·00 | 100·45 |
| | Cpx | 52·66 | 0·51 | 0·74 | 6·63 | 2·89 | 0·06 | 0·09 | 15·13 | 19·64 | 1·81 | 0·00 | 100·16 |
| | Sp | 0·04 | 0·12 | 9·74 | 57·21 | 10·59 | 0·40 | 0·13 | 20·47 | 0·01 | 0·01 | 0·00 | 98·72 |
| SW20 | Ol | 41·51 | 0·00 | 0·02 | 0·00 | 9·14 | 0·39 | 0·13 | 49·69 | 0·02 | 0·01 | 0·00 | 100·91 |
| | Opx | 56·49 | 0·09 | 0·34 | 3·48 | 5·86 | 0·11 | 0·13 | 33·80 | 0·45 | 0·05 | 0·00 | 100·82 |
| | Cpx | 53·02 | 0·47 | 0·91 | 5·85 | 2·18 | 0·03 | 0·07 | 15·08 | 20·85 | 1·72 | 0·01 | 100·18 |
| | Sp | 0·02 | 0·07 | 13·89 | 54·65 | 10·02 | 0·33 | 0·13 | 20·40 | 0·00 | 0·01 | 0·01 | 99·52 |
| SW22 | Ol | 41·24 | 0·02 | 0·00 | 0·00 | 9·86 | 0·39 | 0·14 | 48·55 | 0·05 | 0·00 | 0·00 | 100·24 |
| | Opx | 55·81 | 0·07 | 0·34 | 4·20 | 6·10 | 0·13 | 0·16 | 32·63 | 0·65 | 0·11 | 0·00 | 100·21 |
| | Cpx | 52·91 | 0·43 | 0·90 | 6·30 | 2·63 | 0·03 | 0·06 | 14·93 | 20·01 | 1·82 | 0·00 | 100·02 |
| | Sp | 0·01 | 0·08 | 12·11 | 55·79 | 10·40 | 0·38 | 0·12 | 20·03 | 0·00 | 0·01 | 0·00 | 98·94 |

*n*, number of spot analyses for minerals; total iron is expressed as FeO.

1990), a selection of which are shown in Table 3. Despite systematic temperature differences between the thermometers, the temperatures returned for each locality vary by no more than 300°C and the temperature ranges for a given thermometer are indistinguishable between localities. If the xenoliths equilibrated to a geotherm similar to that proposed by Zheng *et al.* (2006) for garnet-bearing Shanwang peridotites, the temperatures imply sampling over a depth range of ~20 km, all within the spinel stability field.

As mentioned above, because of poor preservation of primary minerals in the Mengyin peridotites, their $P$–$T$ conditions cannot be constrained. Minimum derivation depths of 50–100 km, however, can be inferred from the presence of garnet peridotites previously noted (Gao *et al.*, 2002).

*Table 3: Temperature calculations for Penglai and Shanwang peridotites using various geothermometers**

| | Wood & Banno (1973) | Wells (1977) | Bertrand & Mercier (1985) | Brey & Kohler (1990) |
|---|---|---|---|---|
| PL01 | 1055 | 958 | 1071 | 1005 |
| PL02 | 1069 | 963 | 1019 | 965 |
| PL03 | 1110 | 1038 | 1178 | 1094 |
| PL06 | 1065 | 967 | 1075 | 1012 |
| PL07 | 1127 | 1047 | 1176 | 1113 |
| PL08 | 1059 | 947 | 1008 | 956 |
| PL13 | 1014 | 910 | 999 | 935 |
| PL14 | 1072 | 973 | 1069 | 1012 |
| PL16 | 1113 | 1044 | 1188 | 1101 |
| PL17 | 1080 | 984 | 1074 | 1014 |
| PL18 | 1067 | 962 | 1028 | 973 |
| PL19 | 1075 | 976 | 1052 | 996 |
| PL23 | 1009 | 893 | 910 | 855 |
| SW02 | 1002 | 894 | 963 | 903 |
| SW03 | 1009 | 904 | 981 | 918 |
| SW04 | 1037 | 933 | 1010 | 952 |
| SW05 | 1036 | 961 | 1036 | 970 |
| SW06 | 1064 | 966 | 1074 | 1013 |
| SW07 | 1111 | 1016 | 1132 | 1075 |
| SW08 | 1056 | 965 | 1073 | 1004 |
| SW09 | 1119 | 1022 | 1143 | 1088 |
| SW10 | 998 | 888 | 954 | 892 |
| SW11 | 1050 | 943 | 1020 | 963 |
| SW12 | 992 | 888 | 952 | 888 |
| SW13 | 974 | 856 | 899 | 839 |
| SW14 | 1134 | 1053 | 1181 | 1115 |
| SW15 | 1072 | 967 | 1057 | 1001 |
| SW16 | 1077 | 970 | 1055 | 1005 |
| SW17 | 1084 | 993 | 1110 | 1046 |
| SW18 | 1028 | 918 | 984 | 926 |
| SW19 | 1093 | 1007 | 1123 | 1056 |
| SW20 | 1041 | 933 | 1010 | 956 |
| SW22 | 1078 | 982 | 1087 | 1024 |

*Pressure of 1·5 GPa assumed throughout.

## Rare earth and trace elements

All Mengyin peridotites are strongly light REE (LREE) enriched (Fig. 5a), and, except for sample MY10, are characterized by relatively high total REE concentrations. On a primitive mantle-normalized diagram, the Mengyin samples show significant Sr depletion, as well as variable depletion in Th (Fig. 5b).

The REE patterns of the Penglai peridotites display little variation (Fig. 5c). The cpx-poor lherzolites (PL08, PL19) and harzburgites (PL02, PL18, PL23), are relatively LREE enriched and heavy REE (HREE) depleted. Sample PL19 is characterized by a spoon-shaped REE pattern, and the two harzburgites, PL02 and PL23, have the lowest HREE abundances of this suite. LREE enrichment of cpx-poor mantle xenoliths is common worldwide (McDonough & Frey, 1989). The cpx-rich lherzolites, such as PL01, PL06, PL07, PL16 and PL17, show more limited LREE enrichment, with the exception of sample PL03. The LREE-depleted character of many of the Penglai cpx separates (eight out of 19 samples, Table 5, including most of the lherzolites), suggests that the whole-rock REE patterns may have been compromised by addition of a LREE-enriched grain boundary phase (see Discussion). Compared with those from the Mengyin kimberlites, the Penglai xenoliths have lower La/Yb ratios. Similar to the REE patterns, the primitive mantle-normalized trace element patterns of the Penglai peridotites show relatively uniform variations with slight enrichments in Sr and depletions in Ti (Fig. 5d).

The REE patterns of the Shanwang samples are more variable (Fig. 5e). The most refractory samples, SW07 and SW09, are strongly enriched in LREE and depleted in HREE. Lherzolites SW02, SW03, SW04, SW10, SW12, SW13, SW18, and SW20 are LREE depleted, albeit with some showing La enrichment relative to Ce. The remaining samples are LREE enriched. The primitive mantle-normalized plots for the Shanwang samples are different from those of the Penglai xenoliths, showing pronounced positive Sr and negative Ti anomalies (Fig. 5f), possibly reflecting some form of Sr-rich (carbonate) melt interaction (Zheng *et al.*, 2005). The two wehrlites (SW01 and SW21) have the highest REE contents, do not show the $TiO_2$ depletions, and show only modest Sr enrichments.

## Clinopyroxene Sr–Nd–Hf isotopic data

Rb–Sr and Sm–Nd isotopic compositions of cpx from the Penglai and Shanwang xenoliths are provided in Tables 4 and 5, respectively. Most of the Penglai samples have $^{87}Rb/^{86}Sr$ ratios less than 0·06 and $^{87}Sr/^{86}Sr$ ratios between 0·7022 and 0·7042, except for unleached cpx PL15, which has a higher $^{87}Rb/^{86}Sr$ of 0·11 (Fig. 6a). The Shanwang samples show even less variation in $^{87}Rb/^{86}Sr$ and $^{87}Sr/^{86}Sr$ ratios (Fig. 6a). Generally, the leached cpx are slightly less radiogenic in $^{87}Sr/^{86}Sr$, compared with their paired, unleached cpx (Table 4; Fig. 6a). Although the differences in Sr concentration between leached and unleached cpx are insignificant, the Rb concentrations in leached cpx are much lower than their paired, unleached cpx (Table 4; Fig. 6a). Similar to other worldwide xenolith suites, no Rb–Sr isochron can be generated from the data. Penglai and Shanwang samples show modest variations in $^{147}Sm/^{144}Nd$ and $^{143}Nd/^{144}Nd$ ratios (Fig. 6b). The leached cpx have $^{147}Sm/^{144}Nd$ and $^{143}Nd/^{144}Nd$ ratios nearly identical to their paired, unleached cpx, except for samples

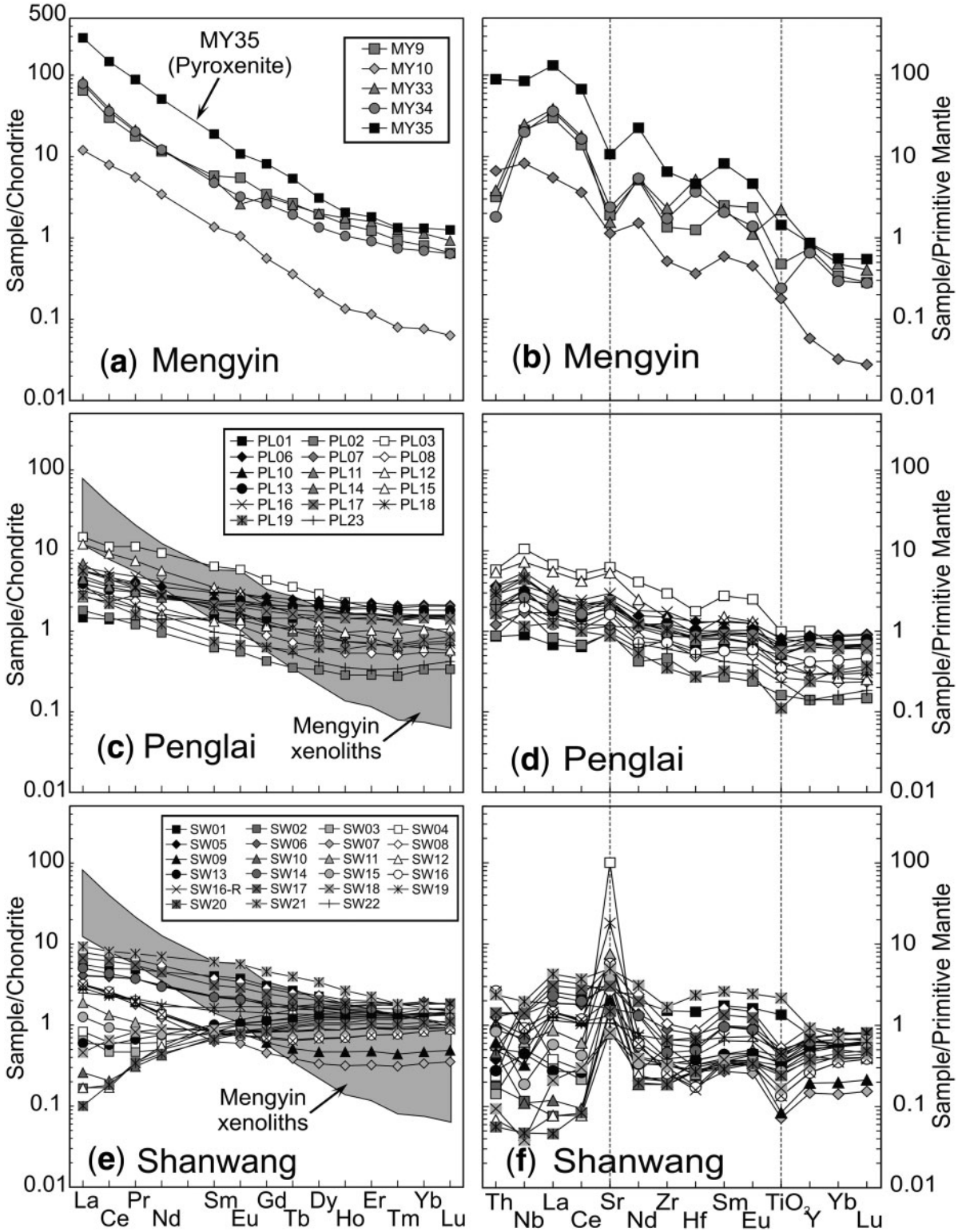


**Fig. 5.** Chondrite-normalized rare earth element patterns (a, c, e) and primitive mantle-normalized trace element patterns (b, d, f) for the xenoliths from Mengyin, Penglai and Shanwang. Chondrite normalizing values are from Masuda *et al.* (1973) divided by 1·2, and those of primitive mantle for trace elements are from McDonough & Sun (1995). R, replicate analysis.

*Table 4: Cpx Rb–Sr isotopic compositions of the Penglai and Shanwang peridotites*

| Sample | *t* (Ma) | Rb (ppm) | Sr (ppm) | $^{87}Rb/^{86}Sr$ | $^{87}Sr/^{86}Sr$ | 2σ | $I_{Sr}$ |
|---|---|---|---|---|---|---|---|
| PL01 | 5 | 0·190 | 71·70 | 0·00767 | 0·702319 | 0·000014 | 0·702318 |
| PL02 | 5 | 0·408 | 139·2 | 0·00847 | 0·702696 | 0·000014 | 0·702695 |
| PL03 | 5 | 0·116 | 155·5 | 0·00215 | 0·703476 | 0·000020 | 0·703476 |
| PL03-leached | | 0·109 | 164·6 | 0·00191 | 0·703373 | 0·000007 | 0·703373 |
| PL06 | 5 | 0·338 | 75·45 | 0·0130 | 0·702646 | 0·000013 | 0·702645 |
| PL07 | 5 | 0·207 | 54·44 | 0·0110 | 0·702570 | 0·000014 | 0·702569 |
| PL11 | 5 | 0·266 | 13·18 | 0·0584 | 0·704250 | 0·000046 | 0·704245 |
| PL12 | 5 | 0·168 | 89·95 | 0·00541 | 0·702552 | 0·000010 | 0·702551 |
| PL13 | 5 | 0·359 | 307·9 | 0·00338 | 0·703293 | 0·000014 | 0·703292 |
| PL14 | 5 | 0·492 | 75·13 | 0·0190 | 0·702897 | 0·000014 | 0·702896 |
| PL15 | 5 | 2·19 | 59·09 | 0·107 | 0·702831 | 0·000014 | 0·702824 |
| PL15-leached | | 0·100 | 60·58 | 0·00479 | 0·702795 | 0·000027 | 0·702795 |
| PL16 | 5 | 0·271 | 160·2 | 0·00490 | 0·703339 | 0·000012 | 0·703339 |
| PL17 | 5 | 0·257 | 34·96 | 0·0212 | 0·703335 | 0·000013 | 0·703334 |
| PL17-leached | | 0·0983 | 32·88 | 0·00864 | 0·702914 | 0·000010 | 0·702914 |
| PL18 | 5 | 0·346 | 20·21 | 0·0495 | 0·704127 | 0·000014 | 0·704123 |
| PL19 | 5 | 0·0766 | 41·13 | 0·00539 | 0·703623 | 0·000013 | 0·703622 |
| PL19-leached | | | 37·53 | | 0·703496 | 0·000014 | |
| PL19-leached-R | | 0·0173 | 37·40 | 0·00133 | 0·703470 | 0·000011 | 0·703470 |
| PL23 | 5 | 0·308 | 34·26 | 0·0260 | 0·703646 | 0·000013 | 0·703644 |
| PL23-leached | | 0·094 | 32·97 | 0·0083 | 0·703590 | 0·000016 | 0·703590 |
| SW01 | 16 | 2·22 | 117·7 | 0·0546 | 0·703220 | 0·000013 | 0·703207 |
| SW01-leached | | 0·0806 | 100·3 | 0·00232 | 0·703053 | 0·000013 | 0·703053 |
| SW02 | 16 | 0·350 | 20·21 | 0·0500 | 0·702676 | 0·000013 | 0·702664 |
| SW03-leached | 16 | 0·0230 | 10·51 | 0·00632 | 0·702895 | 0·000016 | 0·702893 |
| SW04 | 16 | 0·447 | 28·87 | 0·0463 | 0·703135 | 0·000018 | 0·703124 |
| SW04-leached | | 0·0074 | 20·02 | 0·0011 | 0·702450 | 0·000014 | 0·702450 |
| SW05 | 16 | 0·569 | 165·0 | 0·0100 | 0·703183 | 0·000015 | 0·703181 |
| SW05-leached | | 0·0525 | 161·7 | 0·000938 | 0·703031 | 0·000011 | 0·703031 |
| SW07 | 16 | 0·860 | 277·4 | 0·00896 | 0·703131 | 0·000013 | 0·703129 |
| SW08 | 16 | 1·49 | 146·8 | 0·0294 | 0·703391 | 0·000015 | 0·703384 |
| SW09 | 16 | 0·845 | 282·9 | 0·00863 | 0·703145 | 0·000013 | 0·703143 |
| SW10 | 16 | 0·372 | 23·18 | 0·0464 | 0·702631 | 0·000013 | 0·702620 |
| SW11 | 16 | 0·264 | 90·52 | 0·00845 | 0·703176 | 0·000013 | 0·703174 |
| SW11-leached | | 0·0148 | 82·26 | 0·000519 | 0·703158 | 0·000017 | 0·703158 |
| SW12 | 16 | 0·231 | 14·44 | 0·0463 | 0·702590 | 0·000036 | 0·702579 |
| SW13 | 16 | 0·481 | 27·93 | 0·0498 | 0·702665 | 0·000012 | 0·702654 |
| SW14 | 16 | 0·469 | 127·6 | 0·0106 | 0·703132 | 0·000014 | 0·703129 |
| SW15 | 16 | 0·307 | 104·6 | 0·00849 | 0·703259 | 0·000011 | 0·703257 |
| SW16 | 16 | 0·626 | 176·5 | 0·0103 | 0·703525 | 0·000014 | 0·703522 |
| SW17 | 16 | 0·260 | 224·3 | 0·00335 | 0·703133 | 0·000012 | 0·703132 |
| SW18 | 16 | 0·048 | 60·99 | 0·00228 | 0·702268 | 0·000013 | 0·702268 |
| SW19 | 16 | 0·261 | 109·9 | 0·00688 | 0·702905 | 0·000013 | 0·702904 |
| SW20 | 16 | 0·279 | 29·24 | 0·0276 | 0·702499 | 0·000013 | 0·702493 |
| SW21 | 16 | 0·622 | 126·0 | 0·0143 | 0·703100 | 0·000013 | 0·703097 |
| SW22 | 16 | | 167·5 | | 0·703064 | 0·000012 | |
| SW22-leached | | 0·0878 | 162·9 | 0·00156 | 0·703041 | 0·000013 | 0·703041 |

'leached' indicates that the minerals were leached with 6M HCl at 100°C overnight before crushing to 200–400 mesh; 'R', replicate analysis.

*Table 5: Cpx Sm–Nd isotopic compositions of the Penglai and Shanwang peridotites*

| Sample | *t* (Ma) | Sm (ppm) | Nd (ppm) | $^{147}Sm/^{144}Nd$ | $^{143}Nd/^{144}Nd$ | 2σ | $\varepsilon_{Nd(t)}$ | $\varepsilon_{Nd(0)}$ | $T_{DM}$ (Ma) |
|---|---|---|---|---|---|---|---|---|---|
| PL01 | 5 | 1·349 | 3·391 | 0·2406 | 0·513215 | 0·000014 | 11·4 | 11·3 | 364 |
| PL02 | 5 | 1·082 | 4·399 | 0·1487 | 0·513003 | 0·000012 | 7·3 | 7·1 | 347 |
| PL03 | 5 | 3·291 | 13·20 | 0·1508 | 0·512983 | 0·000010 | 6·9 | 6·7 | 408 |
| PL03-leached | | 4·161 | 16·96 | 0·1483 | 0·512977 | 0·000008 | 6·7 | 6·6 | 406 |
| PL06 | 5 | 1·463 | 3·725 | 0·2375 | 0·513080 | 0·000012 | 8·7 | 8·6 | −457 |
| PL07 | 5 | 1·340 | 3·254 | 0·2490 | 0·513168 | 0·000013 | 10·5 | 10·3 | 76 |
| PL11 | 5 | 0·1487 | 0·5354 | 0·1679 | 0·512971 | 0·000040 | 6·6 | 6·5 | 601 |
| PL12 | 5 | 1·681 | 4·176 | 0·2433 | 0·513176 | 0·000015 | 10·6 | 10·5 | 128 |
| PL13 | 5 | 2·614 | 12·44 | 0·1270 | 0·512908 | 0·000012 | 5·4 | 5·3 | 428 |
| PL14 | 5 | 1·313 | 3·528 | 0·2251 | 0·513285 | 0·000010 | 12·7 | 12·6 | 1794 |
| PL15 | 5 | 1·102 | 2·781 | 0·2396 | 0·513190 | 0·000014 | 10·9 | 10·8 | 232 |
| PL15-leached | | 1·246 | 3·202 | 0·2355 | 0·513203 | 0·000007 | 11·1 | 11·0 | 362 |
| PL16 | 5 | 2·214 | 7·993 | 0·1674 | 0·513022 | 0·000013 | 7·6 | 7·5 | 425 |
| PL17 | 5 | 0·7616 | 1·403 | 0·3283 | 0·513813 | 0·000013 | 23·1 | 22·9 | 881 |
| PL17-leached | | 0·8447 | 1·491 | 0·3427 | 0·513867 | 0·000009 | 24·1 | 24·0 | 847 |
| PL18 | 5 | 0·7417 | 1·424 | 0·3150 | 0·513406 | 0·000013 | 15·1 | 15·0 | 384 |
| PL19 | 5 | 0·2420 | 1·197 | 0·1222 | 0·513054 | 0·000015 | 8·2 | 8·1 | 162 |
| PL19-leached | | 0·2335 | 1·125 | 0·1255 | 0·513143 | 0·000010 | 10·0 | 9·8 | 14 |
| PL19-leached-R | | 0·2303 | 1·138 | 0·1224 | 0·513126 | 0·000011 | 9·6 | 9·5 | 42 |
| PL23 | 5 | 0·2675 | 0·9223 | 0·1754 | 0·512795 | 0·000035 | 3·2 | 3·1 | 1412 |
| PL23-leached | | 0·2559 | 0·8949 | 0·1732 | 0·512894 | 0·000008 | 5·1 | 5·0 | 967 |
| SW01 | 16 | 2·364 | 8·035 | 0·1778 | 0·512944 | 0·000013 | 6·4 | 6·0 | 878 |
| SW01-leached | | 2·882 | 9·875 | 0·1765 | 0·512964 | 0·000013 | 6·8 | 6·4 | 766 |
| SW02 | 16 | 0·9915 | 1·678 | 0·3571 | 0·513411 | 0·000011 | 15·5 | 15·1 | 277 |
| SW03 | 16 | 1·031 | 1·673 | 0·3725 | 0·513018 | 0·000012 | 7·8 | 7·4 | −128 |
| SW03-leached | | 1·174 | 1·927 | 0·3684 | 0·513076 | 0·000007 | 8·9 | 8·5 | −74 |
| SW04 | 16 | 1·029 | 1·834 | 0·3391 | 0·513479 | 0·000010 | 16·8 | 16·4 | 400 |
| SW04-leached | | 1·155 | 2·070 | 0·3379 | 0·513473 | 0·000007 | 16·7 | 16·3 | 396 |
| SW05 | 16 | 2·248 | 8·976 | 0·1514 | 0·513078 | 0·000012 | 9·0 | 8·6 | 179 |
| SW07 | 16 | 2·475 | 12·85 | 0·1164 | 0·512940 | 0·000013 | 6·3 | 5·9 | 331 |
| SW08 | 16 | 2·360 | 9·530 | 0·1497 | 0·512981 | 0·000013 | 7·1 | 6·7 | 405 |
| SW09 | 16 | 2·415 | 12·13 | 0·1204 | 0·512940 | 0·000013 | 6·3 | 5·9 | 346 |
| SW10 | 16 | 1·051 | 1·796 | 0·3537 | 0·513457 | 0·000012 | 16·4 | 16·0 | 334 |
| SW11 | 16 | 1·163 | 3·262 | 0·2156 | 0·513123 | 0·000009 | 9·9 | 9·5 | −2301 |
| SW11-leached | | 1·339 | 3·830 | 0·2114 | 0·513105 | 0·000007 | 9·5 | 9·1 | 3079 |
| SW12 | 16 | 1·057 | 1·742 | 0·3669 | 0·513411 | 0·000014 | 15·5 | 15·1 | 259 |
| SW13 | 16 | 1·204 | 2·388 | 0·3048 | 0·513266 | 0·000012 | 12·7 | 12·3 | 193 |
| SW14 | 16 | 1·551 | 5·989 | 0·1566 | 0·513095 | 0·000011 | 9·3 | 8·9 | 150 |
| SW15 | 16 | 1·188 | 3·809 | 0·1886 | 0·513090 | 0·000013 | 9·2 | 8·8 | 370 |
| SW16 | 16 | 0·9280 | 4·575 | 0·1226 | 0·513078 | 0·000012 | 9·0 | 8·6 | 123 |
| SW17 | 16 | 2·206 | 9·757 | 0·1367 | 0·512982 | 0·000012 | 7·1 | 6·7 | 336 |
| SW18 | 16 | 1·240 | 3·605 | 0·2079 | 0·513291 | 0·000010 | 13·1 | 12·7 | −3742 |
| SW19 | 16 | 1·492 | 4·852 | 0·1859 | 0·513202 | 0·000012 | 11·4 | 11·0 | −281 |
| SW20 | 16 | 1·197 | 2·370 | 0·3053 | 0·513267 | 0·000012 | 12·7 | 12·3 | 194 |
| SW21 | 16 | 2·733 | 9·033 | 0·1829 | 0·512986 | 0·000013 | 7·2 | 6·8 | 815 |
| SW22-leached | 16 | 2·342 | 9·970 | 0·1421 | 0·513039 | 0·000005 | 8·2 | 7·8 | 240 |

'leached' indicates that the minerals were leached with 6M HCl at 100°C overnight before crushing to 200–400 mesh; R, replicate analysis; $\varepsilon_{Nd}$ values were calculated using $(^{147}Sm/^{144}Nd)_{CHUR(0)} = 0·1967$ and $(^{143}Nd/^{144}Nd)_{CHUR(0)} = 0·512638$; $T_{DM}$ values were calculated using $(^{147}Sm/^{144}Nd)_{DM(0)} = 0·2137$ and $(^{143}Nd/^{144}Nd)_{DM(0)} = 0·513151$.

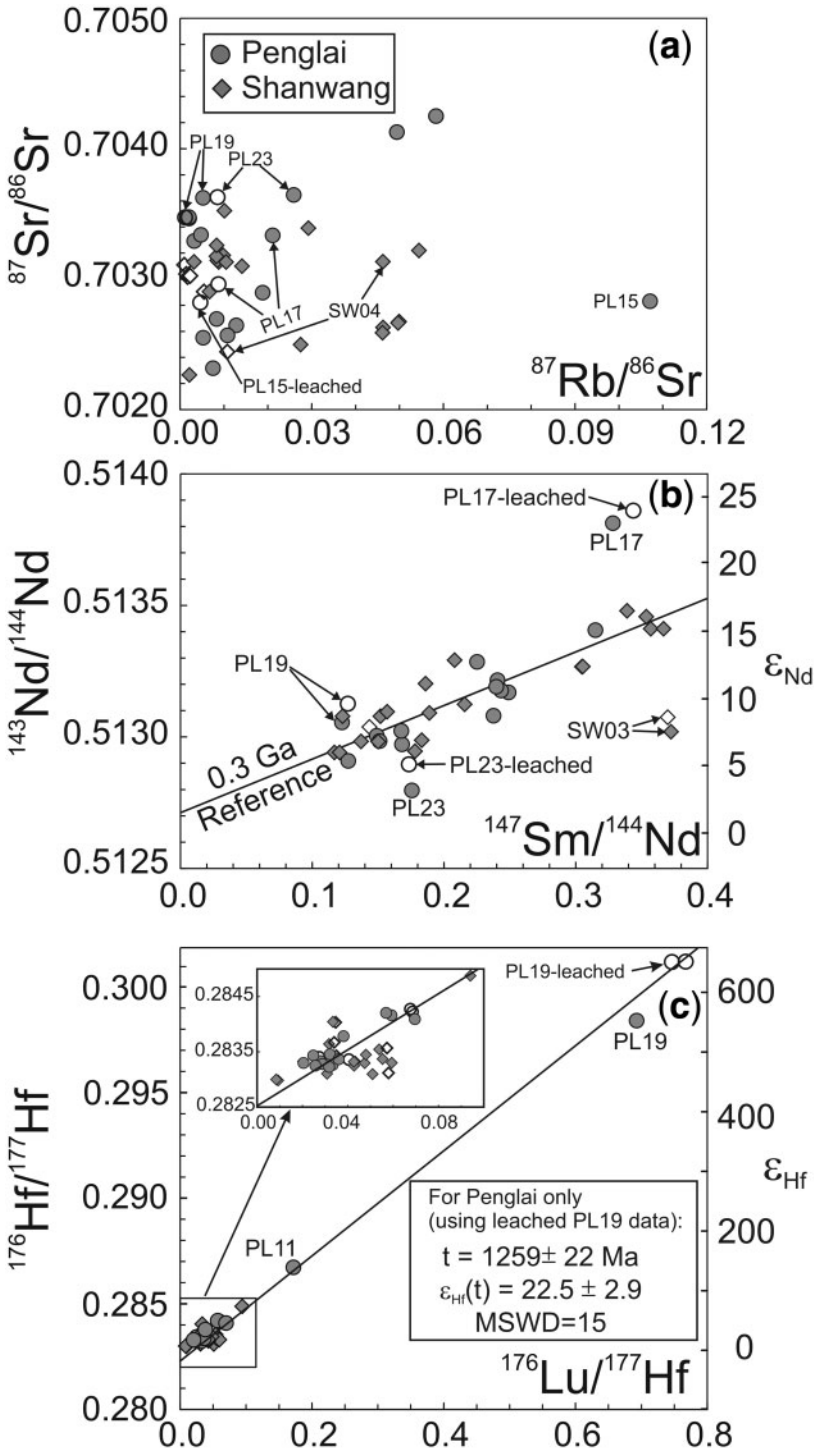


**Fig. 6.** Rb–Sr (a), Sm–Nd (b) and Lu–Hf (c) isotopic compositions of the cpx from the Penglai and Shanwang peridotites. Open circles, leached Penglai cpx; open diamonds, leached Shanwang cpx; In (c) the Lu–Hf isochron with an age of 1259 ± 22 Ma (using leached PL19 cpx data) is for Penglai samples only (although Shanwang data are also plotted in the figure). If the Penglai and Shanwang xenoliths are combined, an isochron age of 1262 ± 35 Ma (using leached PL19 cpx data) is obtained (not shown). The inset shows the data for samples with $^{176}Lu/^{177}Hf$ <0·1.

PL19 and PL23, which have slightly more radiogenic Nd in the leached cpx (Table 5; Fig. 6b). Except for samples PL17 and SW03, all samples plot near an errorchron with an age of ~300 Ma (Fig. 6b).

Hafnium isotopic compositions of the cpx are provided in Table 6 and shown in Fig. 6c. The Penglai samples show larger ranges of $^{176}Lu/^{177}Hf$ and $^{176}Hf/^{177}Hf$ ratios than the Shanwang xenoliths. Generally, the leached cpx have Hf isotopic compositions that are indistinguishable from the paired, unleached cpx, although there are some significant differences in Lu and Hf concentrations (Table 6). The only exception is sample PL19, which is characterized by extremely radiogenic Hf; the leached cpx has slightly more radiogenic Hf (Fig. 6c). The $^{176}Hf/^{177}Hf$ of two analyses of leached PL19 cpx are reproducible within uncertainties. Penglai cpx samples define a Lu–Hf isochron with an age of $1259 \pm 22$ Ma (using the data for the leached PL19 cpx) (Fig. 6c). If the Penglai and Shanwang xenoliths are combined, an isochron age of $1262 \pm 35$ Ma is obtained (also using data for leached cpx from sample PL19).

All the cpx samples are characterized by low initial $^{87}Sr/^{86}Sr$ ratios of 0·7022–0·7042, and high initial $\varepsilon_{Nd}$ and $\varepsilon_{Hf}$ values of +5·4 to +23·1 and +16·0 to +553, when corrected for the eruption ages of the host basalts (Fig. 7). A crude negative correlation between $^{87}Sr/^{86}Sr$ and $\varepsilon_{Nd}$ is similar to cpx from other Cenozoic mantle xenoliths in eastern China (Fig. 7a) (Fan *et al.*, 2000; Rudnick *et al.*, 2004; Wu *et al.*, 2006; and references therein). These Sr–Nd isotopic compositions differ greatly from those for the Paleozoic Mengyin and Fuxian kimberlites and the mantle xenoliths they host (Chi & Lu, 1996; Zheng, 1999; Wu *et al.*, 2006; Zhang & Yang, 2007; Zhang *et al.*, 2008), which are characterized by much more enriched Sr–Nd isotope signatures (Fig. 7a). In a diagram of $\varepsilon_{Nd}$ vs $\varepsilon_{Hf}$, most xenoliths straddle a line of $\varepsilon_{Hf} = 1{\cdot}5\varepsilon_{Nd}$, which is similar to the Nd and Hf isotopic ratios seen in oceanic basalts (Nowell *et al.*, 1998; Vervoort *et al.*, 1999). However, some samples, such as PL19 and PL11, fall above the line at much higher $\varepsilon_{Hf}$ values (Fig. 7b). The apparent decoupling of the Nd–Hf systematics in these samples suggests that high Lu/Hf was preserved for a much longer period of time than high Sm/Nd. Leached cpx sample PL19, which has an extremely high $^{176}Lu/^{177}Hf$ ratio of about 0·76, yields a Hf model age of about 1·3 Ga.

## Re–Os isotopic geochemistry

Re–Os isotopic data for the Mengyin, Penglai and Shanwang xenoliths are given in Table 7. All Mengyin samples have Re concentrations less than 0·1 ppb, with a large range in Os concentrations from 0·1 to 7·8 ppb (Fig. 8a). Three analyses of sample MY9 yielded Os concentrations ranging between 2·0 and 7·8 ppb, indicating a significant 'nugget effect' whereby Os is evidently concentrated in trace phases that are not well homogenized during the preparation of sample powders. Peridotites MY9, MY10 and MY34 have $^{187}Os/^{188}Os$ that are identical within uncertainties: 0·1104–0·1109, corresponding to $T_{RD}$ ages of 2·5–2·6 Ga (Table 7). These model ages are similar to ages reported for peridotites from the Fuxian and Tieling kimberlites (Gao *et al.*, 2002; Wu *et al.*, 2006; Zhang *et al.*, 2008), and chromites from Mengyin (Wu *et al.*, 2006). In contrast to the other Mengyin peridotites, MY33 has a higher $^{187}Os/^{188}Os$ ratio of 0·1166 corresponding to a $T_{RD}$ age of 1·6 Ga (Table 7). In addition, pyroxenite sample MY35 is characterized by relatively low Os (0·97 ppb), relatively high $^{187}Re/^{188}Os$ (0·288) and a high $^{187}Os/^{188}Os$ ratio of 0·1319. Relatively high ratios like this are common in pyroxenites from the lithospheric mantle (e.g. Becker *et al.*, 2004).

The Penglai peridotites are strongly depleted in Re, with concentrations ranging from <0·01 ppb to 0·04 ppb; Os concentrations are mostly <1 ppb (Fig. 8a). The $^{187}Re/^{188}Os$ ratios range from 0·01 to 0·23. As is common in other peridotite xenoliths from the continental lithospheric mantle, the $^{187}Re/^{188}Os$ ratios do not correlate well with their $^{187}Os/^{188}Os$ ratios (Fig. 8b). Generally, the Penglai samples have $^{187}Os/^{188}Os$ ratios ranging from 0·1178 to 0·1289, which is lower than the primitive upper mantle (PUM) estimate of 0·1296 (Meisel *et al.*, 2001). Among these, relatively refractory samples PL02, PL08, PL12 and PL23 (<2 wt % $Al_2O_3$) have similar $^{187}Os/^{188}Os$ ratios around 0·12, with $T_{RD}$ ages of ~1 Ga (Table 7). Sample PL18, however, which has a slightly higher $Al_2O_3$ of 2·27 wt %, has the lowest $^{187}Os/^{188}Os$ of ~0·1170, with $T_{RD}$ and $T_{MA}$ ages of 1·4 and 2·5 Ga, respectively (Table 7).

Shanwang xenoliths have higher average Re and Os concentrations than the Penglai xenoliths, with Re of 0·01–0·51 ppb and Os of 0·3– 8·7 ppb (Fig. 8a). The exception is Fe-rich lherzolite SW05, which has unusually low Re and Os concentrations of 0·005 and 0·04 ppb, respectively, with high $^{187}Re/^{188}Os$ and $^{187}Os/^{188}Os$ of 0·630 and 0·1352, respectively. Lherzolites SW12 and wehrlites SW01 and SW21 have higher $^{187}Re/^{188}Os$ ratios of 0·589–1·636 than PUM and have correspondingly chondritic to radiogenic $^{187}Os/^{188}Os$ of 0·1265–0·1335 (Fig. 8b). The remaining samples have $^{187}Os/^{188}Os$ ratios of 0·1196–0·1274. Of these, relatively refractory samples SW07, SW09, SW11, SW15, SW16 and SW20 have low $^{187}Os/^{188}Os$ ratios, ranging from 0·120 to 0·122, with $T_{RD}$ ages ranging from 0·8 to 1·1 Ga (Table 7). Sample SW03, although not refractory (3·2 wt % $Al_2O_3$), also has a $^{187}Os/^{188}Os$ of ~0·12 (Table 7).

## Platinum-group elements

The PGE abundances (especially Ir, Ru) in replicate analyses of some samples vary considerably beyond analytical uncertainties (Table 8), indicating that the 'nugget effect' is significant for the Mengyin, Penglai and Shanwang xenoliths. Despite this, the chondrite-normalized PGE

*Table 6: Cpx Lu–Hf isotopic compositions of the Penglai and Shanwang peridotites*

| Sample | *t* (Ma) | Lu (ppm) | Hf (ppm) | $^{176}Lu/^{176}Hf$ | $^{176}Hf/^{177}Hf$ | 2σ | $\varepsilon_{Hf}(0)$ | $\varepsilon_{Hf}(t)$ | $T_{DM}$ (Ma) |
|---|---|---|---|---|---|---|---|---|---|
| PL01 | 5 | 0·215 | 0·984 | 0·0311 | 0·283283 | 0·000009 | 18·1 | 18·1 | −244 |
| PL02 | 5 | 0·0940 | 0·477 | 0·0280 | 0·283332 | 0·000017 | 19·8 | 19·8 | −423 |
| PL03 | 5 | 0·167 | 0·958 | 0·0248 | 0·283432 | 0·000007 | 23·4 | 23·4 | −722 |
| PL03-leached | 5 | 0·207 | 1·08 | 0·0274 | 0·283426 | 0·000005 | 23·1 | 23·2 | −865 |
| PL06 | 5 | 0·208 | 1·03 | 0·0288 | 0·283277 | 0·000007 | 17·9 | 17·9 | −153 |
| PL07 | 5 | 0·217 | 0·922 | 0·0334 | 0·283265 | 0·000007 | 17·4 | 17·4 | −159 |
| PL11 | 5 | 0·111 | 0·0915 | 0·172 | 0·286727 | 0·000062 | 140 | 139 | 1377 |
| PL12 | 5 | 0·105 | 0·581 | 0·0257 | 0·283250 | 0·000013 | 16·9 | 16·9 | −1 |
| PL13 | 5 | 0·248 | 1·11 | 0·0318 | 0·283225 | 0·000006 | 16·0 | 16·0 | 199 |
| PL14 | 5 | 0·194 | 0·859 | 0·0321 | 0·283456 | 0·000009 | 24·2 | 24·2 | −1779 |
| PL15 | 5 | 0·177 | 0·699 | 0·0360 | 0·283365 | 0·000012 | 21·0 | 21·0 | −2614 |
| PL15-leached | 5 | 0·213 | 0·753 | 0·0402 | 0·283396 | 0·000005 | 22·1 | 22·0 | 4192 |
| PL16 | 5 | 0·165 | 1·14 | 0·0205 | 0·283298 | 0·000008 | 18·6 | 18·6 | −143 |
| PL17 | 5 | 0·175 | 0·420 | 0·0593 | 0·284162 | 0·000017 | 49·1 | 49·1 | 2285 |
| PL17-R | 5 | 0·171 | 0·427 | 0·0569 | 0·284205 | 0·000016 | 50·7 | 50·6 | 2694 |
| PL17-leached | 5 | 0·209 | 0·431 | 0·0690 | 0·284259 | 0·000007 | 52·6 | 52·5 | 1740 |
| PL18 | 5 | 0·156 | 0·582 | 0·0381 | 0·283783 | 0·000012 | 35·8 | 35·8 | – |
| PL19 | 5 | 0·130 | 0·0267 | 0·693 | 0·298410 | 0·000177 | 553 | 551 | 1227 |
| PL19-leached | 5 | 0·121 | 0·0232 | 0·747 | 0·301364 | 0·000048 | 654 | 652 | 1345 |
| PL19-leached-R | 5 | 0·125 | 0·0232 | 0·768 | 0·301392 | 0·000058 | 655 | 652 | 1308 |
| PL23 | 5 | 0·0653 | 0·133 | 0·0696 | 0·284091 | 0·000075 | 46·7 | 46·5 | 1424 |
| PL23-leached | 5 | 0·0612 | 0·129 | 0·0675 | 0·284299 | 0·000019 | 54·0 | 53·9 | 1895 |
| SW01 | 16 | 0·0974 | 1·49 | 0·00928 | 0·282981 | 0·000010 | 7·4 | 7·7 | 492 |
| SW02 | 16 | 0·202 | 0·605 | 0·0474 | 0·283297 | 0·000014 | 18·6 | 18·4 | 275 |
| SW03 | 16 | 0·221 | 0·618 | 0·0509 | 0·283097 | 0·000013 | 11·5 | 11·3 | −660 |
| SW03-leached | 16 | 0·271 | 0·659 | 0·0584 | 0·283098 | 0·000004 | 11·5 | 11·3 | −409 |
| SW04 | 16 | 0·224 | 0·591 | 0·0538 | 0·283544 | 0·000016 | 27·3 | 27·1 | 1011 |
| SW04-leached | 16 | 0·252 | 0·621 | 0·0577 | 0·283575 | 0·000005 | 28·4 | 28·1 | 895 |
| SW05 | 16 | 0·222 | 0·887 | 0·0356 | 0·283324 | 0·000011 | 19·5 | 19·5 | −1457 |
| SW05-leached | 16 | 0·239 | 0·944 | 0·0360 | 0·283318 | 0·000006 | 19·3 | 19·3 | −1548 |
| SW07 | 16 | 0·121 | 0·821 | 0·0209 | 0·283327 | 0·000012 | 19·6 | 19·8 | −236 |
| SW08 | 16 | 0·215 | 0·989 | 0·0309 | 0·283104 | 0·000010 | 11·7 | 11·8 | 1028 |
| SW09 | 16 | 0·114 | 0·838 | 0·0193 | 0·283327 | 0·000011 | 19·6 | 19·8 | −218 |
| SW10 | 16 | 0·238 | 0·611 | 0·0553 | 0·283371 | 0·000019 | 21·2 | 20·9 | 380 |
| SW11 | 16 | 0·168 | 0·704 | 0·0340 | 0·283410 | 0·000011 | 22·5 | 22·5 | −1982 |
| SW11-leached | 16 | 0·194 | 0·774 | 0·0356 | 0·283405 | 0·000005 | 22·4 | 22·4 | −3107 |
| SW12 | 16 | 0·244 | 0·584 | 0·0594 | 0·283302 | 0·000013 | 18·8 | 18·5 | 133 |
| SW13 | 16 | 0·210 | 0·691 | 0·0432 | 0·283327 | 0·000011 | 19·6 | 19·5 | 852 |
| SW14 | 16 | 0·214 | 0·633 | 0·0480 | 0·283448 | 0·000011 | 23·9 | 23·8 | 1097 |
| SW15 | 16 | 0·162 | 0·692 | 0·0334 | 0·283446 | 0·000014 | 23·8 | 23·8 | −2121 |
| SW16 | 16 | 0·169 | 0·256 | 0·0941 | 0·284878 | 0·000026 | 74·5 | 73·8 | 1543 |
| SW17 | 16 | 0·221 | 0·735 | 0·0428 | 0·283249 | 0·000012 | 16·9 | 16·8 | −12 |
| SW18 | 16 | 0·188 | 0·801 | 0·0335 | 0·284044 | 0·000013 | 45·0 | 45·0 | −9369 |
| SW19 | 16 | 0·216 | 0·974 | 0·0315 | 0·283454 | 0·000012 | 24·1 | 24·1 | −1614 |
| SW20 | 16 | 0·213 | 0·709 | 0·0427 | 0·283320 | 0·000015 | 19·4 | 19·3 | 870 |
| SW21 | 16 | 0·102 | 1·71 | 0·0085 | 0·282999 | 0·000010 | 8·0 | 8·3 | 447 |
| SW22 | 16 | 0·194 | 0·867 | 0·0318 | 0·283641 | 0·000010 | 30·7 | 30·8 | −3255 |
| SW22-leached | 16 | 0·215 | 0·884 | 0·0346 | 0·283666 | 0·000005 | 31·6 | 31·6 | −6178 |

'leached' indicates that the minerals were leached with 6M HCl at 100°C overnight before crushing to 200–400 mesh; R, replicate analysis; $\varepsilon_{Hf}$ values were calculated using $(^{176}Lu/^{177}Hf)_{CHUR(0)} = 0·0332$ and $(^{176}Hf/^{177}Hf)_{CHUR(0)} = 0·282772$; $T_{DM}$ values were calculated using $(^{176}Lu/^{177}Hf)_{DM(0)} = 0·0384$ and $(^{176}Hf/^{177}Hf)_{DM(0)} = 0·28325$; Hf isotopic ratios of replicate analyses of sample PL19 are blank-corrected (using blank values: Hf, 40 pg; $^{176}Hf/^{177}Hf$ ratio of 0·283).

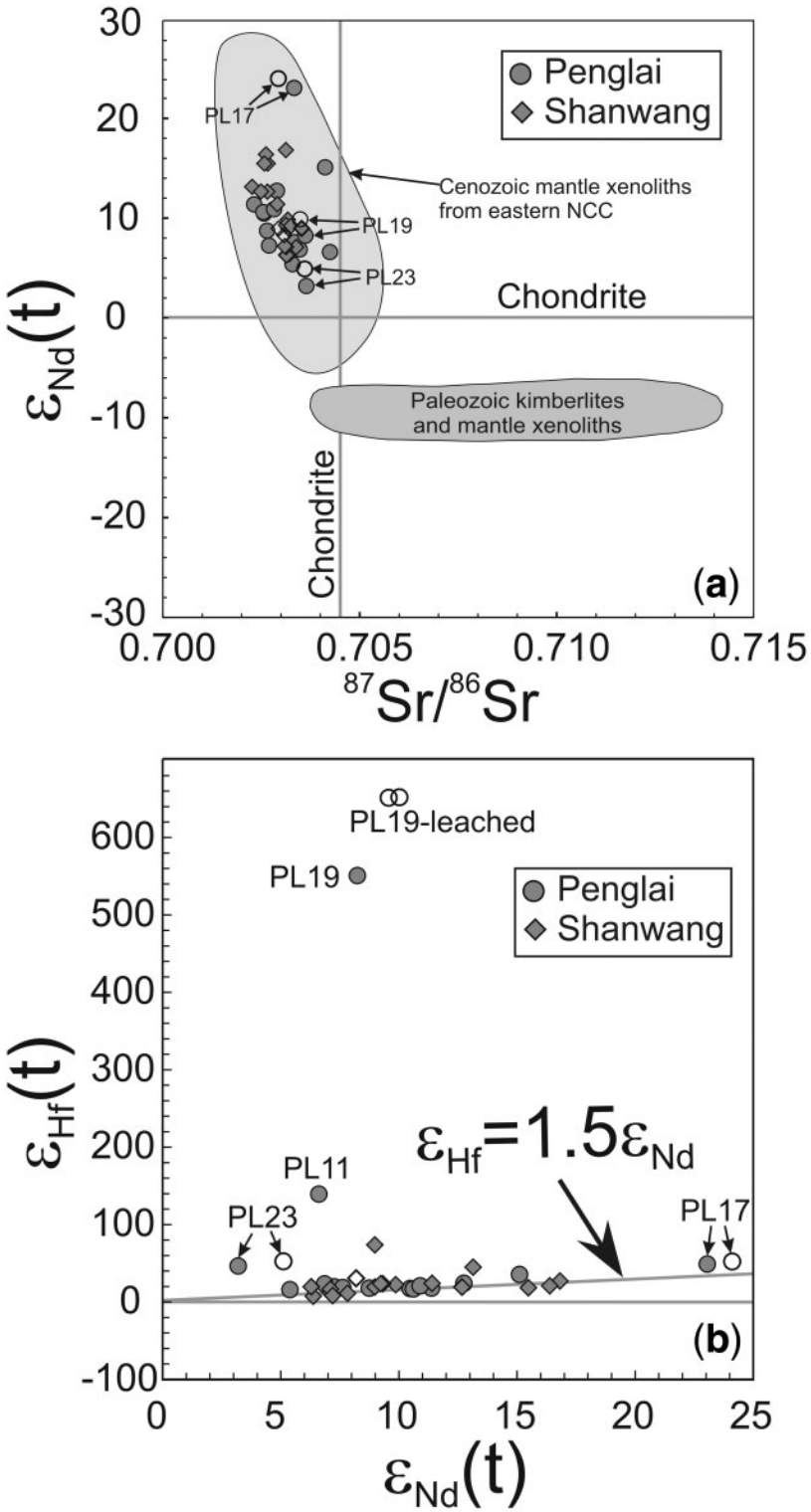


**Fig. 7.** Sr–Nd (a) and Nd–Hf (b) isotope correlation diagrams for cpx from the Penglai and Shanwang peridotites. 't' represents the eruption age of the host basalts; Open circles, leached Penglai cpx; open diamonds, leached Shanwang cpx. In (a), data sources for Paleozoic kimberlites and their mantle xenoliths are Chi & Lu (1996), Zheng (1999), Wu *et al.* (2006), Zhang & Yang (2007) and Zhang *et al.* (2008); data sources for Cenozoic mantle xenoliths from the eastern NCC are Fan *et al.* (2000), Rudnick *et al.* (2004), Wu *et al.* (2006), and references therein.

*Table 7: Re–Os isotopic compositions of the mantle xenoliths*

| Sample | T (Ma) | $Al_2O_3$ (wt %) | Fo (Ol) | Cr-no. (Sp) | *T* (°C) | Re (ppb) | Os (ppb) | $^{187}Re/^{188}Os$ | $^{187}Os/^{188}Os$ | 2σ% | $\gamma_{Os}$ | $Os_i$ | $T_{RD}$ (Ga) | $T_{MA}$ (Ga) |
|---|---|---|---|---|---|---|---|---|---|---|---|---|---|---|
| MY9 | 470 | 0·37 | | | | 0·068 | 1·98 | 0·17 | 0·11052 | 0·07 | −11·8 | 0·10921 | 2·60 | 4·05 |
| MY9-R | 470 | 0·37 | | | | 0·089 | 7·80 | 0·055 | 0·11039 | 0·05 | −11·2 | 0·10996 | 2·49 | 2·81 |
| MY9* | 470 | 0·37 | | | | 0·017 | 4·26 | 0·020 | 0·11056 | 0·05 | −10·9 | 0·11040 | 2·43 | 2·53 |
| MY10* | 470 | 0·06 | | | | 0·005 | 0·090 | 0·3 | 0·11091 | 0·31 | −12·1 | 0·10886 | 2·65 | 6·44 |
| MY33 | 470 | 0·31 | | | | 0·008 | 1·19 | 0·03 | 0·11662 | 0·05 | −6·0 | 0·11635 | 1·57 | 1·67 |
| MY34 | 470 | 0·92 | | | | 0·050 | 3·30 | 0·073 | 0·11043 | 0·05 | −11·3 | 0·10986 | 2·51 | 2·95 |
| MY35 | 470 | 10·0 | | | | 0·058 | 0·969 | 0·29 | 0·13195 | 0·10 | 4·7 | 0·12969 | −0·40 | −2·68 |
| PL01 | 5 | 3·58 | 89·8 | 10·8 | 1005 | 0·008 | 0·280 | 0·1 | 0·12544 | 1·2 | −1·2 | 0·12543 | 0·23 | 0·36 |
| PL02 | 5 | 1·20 | 90·8 | 39·4 | 965 | 0·011 | 0·654 | 0·081 | 0·11974 | 0·26 | −5·7 | 0·11974 | 1·08 | 1·34 |
| PL02* | 5 | | | | | 0·005 | 0·835 | 0·03 | 0·12103 | 0·12 | −4·7 | 0·12103 | 0·89 | 0·96 |
| PL03 | 5 | 4·01 | 88·7 | 11·5 | 1094 | 0·031 | 0·710 | 0·21 | 0·12677 | 0·13 | −0·2 | 0·12675 | 0·04 | 0·07 |
| PL03-R | 5 | | | | | 0·031 | 0·651 | 0·23 | 0·12588 | 0·06 | −0·9 | 0·12586 | 0·17 | 0·39 |
| PL03* | 5 | | | | | 0·523 | 1·15 | 2·19 | 0·12618 | 0·21 | −0·8 | 0·12599 | 0·15 | −0·03 |
| PL06 | 5 | 4·33 | 89·9 | 9·53 | 1012 | 0·019 | 0·400 | 0·23 | 0·12608 | 0·37 | −0·7 | 0·12606 | 0·14 | 0·32 |
| PL07 | 5 | 3·99 | 89·6 | 9·62 | 1113 | 0·181 | 0·829 | 1·05 | 0·12697 | 0·05 | −0·1 | 0·12688 | 0·02 | 0·00 |
| PL07* | 5 | | | | | 0·032 | 0·751 | 0·20 | 0·12722 | 0·11 | 0·2 | 0·12720 | −0·03 | −0·07 |
| PL08 | 5 | 1·70 | 91·3 | 23·8 | 956 | 0·019 | 0·496 | 0·19 | 0·12032 | 0·27 | −5·2 | 0·12030 | 0·99 | 1·83 |
| PL08* | 5 | | | | | 0·001 | 0·426 | 0·01 | 0·12060 | 0·08 | −5·0 | 0·12060 | 0·95 | 0·98 |
| PL10 | 5 | 3·24 | | | | 0·020 | 1·22 | 0·080 | 0·12272 | 0·06 | −3·4 | 0·12271 | 0·64 | 0·79 |
| PL11 | 5 | 2·79 | | | | 0·015 | 0·747 | 0·098 | 0·12519 | 0·10 | −1·4 | 0·12518 | 0·27 | 0·36 |
| PL11* | 5 | | | | | 0·020 | 1·01 | 0·097 | 0·12479 | 0·08 | −1·7 | 0·12478 | 0·33 | 0·43 |
| PL12 | 5 | 1·86 | | | | 0·028 | 1·20 | 0·11 | 0·12072 | 0·03 | −4·9 | 0·12071 | 0·93 | 1·29 |
| PL13 | 5 | 3·91 | 89·5 | 9·72 | 935 | 0·009 | 0·406 | 0·1 | 0·12885 | 0·13 | 1·5 | 0·12884 | −0·28 | −0·38 |
| PL14 | 5 | 3·47 | 90·4 | 15·0 | 1012 | 0·011 | 0·411 | 0·13 | 0·12754 | 0·13 | 0·4 | 0·12753 | −0·08 | −0·12 |
| PL14* | 5 | | | | | 0·008 | 0·470 | 0·08 | 0·12529 | 0·04 | −1·3 | 0·12529 | 0·26 | 0·32 |
| PL15 | 5 | 2·47 | | | | 0·014 | 0·680 | 0·098 | 0·12136 | 0·15 | −4·4 | 0·12135 | 0·84 | 1·10 |
| PL16 | 5 | 3·86 | 88·1 | 11·3 | 1101 | 0·009 | 0·593 | 0·07 | 0·12599 | 0·06 | −0·8 | 0·12598 | 0·15 | 0·18 |
| PL16-R | 5 | | | | | 0·065 | 0·729 | 0·43 | 0·12596 | 0·18 | −0·8 | 0·12592 | 0·16 | −2·27 |
| PL16* | 5 | | | | | 0·011 | 1·15 | 0·046 | 0·12588 | 0·10 | −0·9 | 0·12587 | 0·17 | 0·19 |
| PL17 | 5 | 3·69 | 90·3 | 12·9 | 1014 | 0·012 | 0·541 | 0·10 | 0·12592 | 0·10 | −0·8 | 0·12591 | 0·16 | 0·22 |
| PL17* | 5 | | | | | 0·015 | 0·688 | 0·11 | 0·12546 | 0·10 | −1·2 | 0·12545 | 0·23 | 0·31 |
| PL18 | 5 | 2·27 | 90·7 | 22·4 | 973 | 0·072 | 0·476 | 0·73 | 0·11765 | 0·14 | −7·4 | 0·11759 | 1·39 | −1·72 |
| PL18-R | 5 | | | | | 0·020 | 0·622 | 0·16 | 0·11672 | 0·09 | −8·1 | 0·11670 | 1·52 | 2·48 |
| PL18* | 5 | | | | | 0·410 | 1·02 | 1·93 | 0·11741 | 0·05 | −7·7 | 0·11725 | 1·44 | −0·38 |
| PL19 | 5 | 2·44 | 90·4 | 19·0 | 996 | 0·038 | 0·810 | 0·23 | 0·12711 | 0·23 | 0·1 | 0·12709 | −0·01 | −0·04 |
| PL19* | 5 | | | | | 0·030 | 1·04 | 0·14 | 0·12533 | 0·06 | −1·3 | 0·12532 | 0·25 | 0·38 |
| PL19*-R | 5 | | | | | 0·036 | 0·833 | 0·21 | 0·12547 | 0·22 | −1·2 | 0·12546 | 0·23 | 0·47 |
| PL23 | 5 | 1·88 | 91·1 | 38·9 | 855 | 0·012 | 1·21 | 0·049 | 0·12029 | 0·07 | −5·3 | 0·12028 | 0·99 | 1·13 |
| PL23* | 5 | | | | | 0·011 | 1·11 | 0·046 | 0·12077 | 0·04 | −4·9 | 0·12077 | 0·92 | 1·04 |
| SW01 | 16 | 2·33 | | | | 0·072 | 0·282 | 1·2 | 0·13351 | 0·36 | 5·0 | 0·13319 | −0·93 | 0·47 |
| SW02 | 16 | 3·37 | 90·0 | 10·4 | 903 | 0·161 | 2·99 | 0·259 | 0·12611 | 0·04 | −0·7 | 0·12605 | 0·14 | 0·37 |
| SW03 | 16 | 3·17 | 89·9 | 9·55 | 918 | 0·100 | 3·21 | 0·150 | 0·12101 | 0·02 | −4·7 | 0·12097 | 0·89 | 1·41 |
| SW04 | 16 | 3·55 | 90·3 | 12·0 | 952 | 0·032 | 2·22 | 0·068 | 0·12278 | 0·07 | −3·3 | 0·12276 | 0·63 | 0·75 |
| SW05 | 16 | 2·74 | 86·1 | 13·0 | 970 | 0·005 | 0·036 | 0·6 | 0·13520 | 1·30 | 6·4 | 0·13503 | −1·21 | 2·12 |
| SW06 | 16 | 2·96 | 89·6 | 12·6 | 1013 | 0·077 | 2·02 | 0·18 | 0·12416 | 0·05 | −2·2 | 0·12411 | 0·43 | 0·78 |
| SW07 | 16 | 1·23 | 90·7 | 28·4 | 1075 | 0·420 | 1·39 | 1·44 | 0·12219 | 0·03 | −4·0 | 0·12181 | 0·77 | −0·28 |

(continued)

*Table 7: Continued*

| Sample | T (Ma) | $Al_2O_3$ (wt %) | Fo (Ol) | Cr-no. (Sp) | *T* (°C) | Re (ppb) | Os (ppb) | $^{187}Re/^{188}Os$ | $^{187}Os/^{188}Os$ | 2σ% | $\gamma_{Os}$ | $Os_i$ | $T_{RD}$ (Ga) | $T_{MA}$ (Ga) |
|---|---|---|---|---|---|---|---|---|---|---|---|---|---|---|
| SW07* | 16 | | | | | 0·012 | 1·38 | 0·041 | 0·12230 | 0·08 | −3·6 | 0·12229 | 0·70 | 0·78 |
| SW08 | 16 | 3·50 | 89·0 | 9·67 | 1004 | 0·030 | 0·419 | 0·34 | 0·12739 | 0·16 | 0·3 | 0·12729 | −0·04 | −0·41 |
| SW09 | 16 | 1·82 | 90·9 | 26·4 | 1088 | 0·050 | 1·45 | 0·16 | 0·12171 | 0·21 | −4·1 | 0·12167 | 0·79 | 1·28 |
| SW09* | 16 | | | | | 0·028 | 2·33 | 0·058 | 0·12209 | 0·10 | −3·8 | 0·12208 | 0·73 | 0·85 |
| SW10 | 16 | 3·12 | 90·2 | 10·8 | 892 | 0·224 | 3·27 | 0·331 | 0·12395 | 0·03 | −2·4 | 0·12386 | 0·47 | 2·51 |
| SW11* | 16 | 2·27 | 90·8 | 17·6 | 963 | 0·159 | 4·83 | 0·159 | 0·12131 | 0·02 | −4·4 | 0·12127 | 0·85 | 1·39 |
| SW12 | 16 | 3·63 | 89·3 | 9·03 | 888 | 0·508 | 4·15 | 0·589 | 0·12979 | 0·04 | 2·2 | 0·12964 | −0·39 | 0·89 |
| SW13 | 16 | 2·73 | 90·6 | 15·1 | 839 | 0·312 | 4·38 | 0·343 | 0·12292 | 0·07 | −3·2 | 0·12283 | 0·62 | 4·02 |
| SW14 | 16 | 3·46 | 90·0 | 11·0 | 1115 | 0·262 | 3·88 | 0·326 | 0·12515 | 0·04 | −1·4 | 0·12506 | 0·29 | 1·44 |
| SW15 | 16 | 2·44 | 90·9 | 17·2 | 1001 | 0·248 | 4·51 | 0·265 | 0·12138 | 0·08 | −4·4 | 0·12131 | 0·84 | 2·41 |
| SW16 | 16 | 2·08 | 91·0 | 18·3 | 1005 | 0·263 | 8·69 | 0·146 | 0·11996 | 0·01 | −5·5 | 0·11992 | 1·05 | 1·63 |
| SW17 | 16 | 3·57 | 89·9 | 10·4 | 1046 | 0·113 | 3·53 | 0·154 | 0·12325 | 0·05 | −2·9 | 0·12321 | 0·56 | 0·90 |
| SW18 | 16 | 1·96 | 90·6 | 18·7 | 926 | 0·415 | 4·83 | 0·414 | 0·12501 | 0·01 | −1·6 | 0·12490 | 0·31 | −11·06 |
| SW18* | 16 | | | | | 0·362 | 4·38 | 0·398 | 0·12527 | 0·11 | −1·4 | 0·12516 | 0·27 | 20·71 |
| SW19 | 16 | 2·93 | 89·2 | 10·3 | 1056 | 0·083 | 2·50 | 0·16 | 0·12500 | 0·03 | −1·5 | 0·12496 | 0·30 | 0·49 |
| SW20 | 16 | 2·16 | 90·7 | 14·5 | 956 | 0·200 | 4·12 | 0·234 | 0·11965 | 0·02 | −5·8 | 0·11959 | 1·10 | 2·57 |
| SW21 | 16 | 3·80 | 81·8 | 21·0 | | 0·332 | 0·978 | 1·64 | 0·12650 | 0·06 | −0·7 | 0·12606 | 0·14 | −0·02 |
| SW22 | 16 | 2·92 | 89·8 | 12·7 | 1024 | 0·025 | 0·564 | 0·21 | 0·12255 | 0·09 | −3·5 | 0·12249 | 0·67 | 1·39 |

The parameters used in calculation are: $\lambda_{Re} = 1{\cdot}666 \times 10^{-11}$/year, $(^{187}Re/^{188}Os)_{Chond(0)} = 0{\cdot}40186$, $(^{187}Os/^{188}Os)_{Chond(0)} = 0{\cdot}1270$ (Shirey & Walker, 1998); R, replicate analysis; $Al_2O_3$ (wt %) is normalized to 100% volatile-free; Re, Os concentration and Os isotopic ratios are blank-corrected.
*Measured in UMD.

patterns (and hence, PGE element ratios) are generally reproducible.

For the Mengyin samples, the chondrite-normalized PGE patterns show relatively flat IPGE (Os, Ir, Ru) patterns, with corresponding strong PPGE (Pt, Pd) depletions (Fig. 9a). Thus, $(Os/Ir)_N$ and $(Ru/Ir)_N$ of Mengyin peridotites straddle unity (Fig. 9d), but $(Pt/Ir)_N$ and $(Pd/Ir)_N$ values are uniformly less than 1 (Fig. 9e and 9f). These characteristics are frequently observed in ancient cratonic peridotite xenoliths from elsewhere (Rehkämper *et al.*, 1997; Pearson *et al.*, 2004), and have previously been ascribed to large degrees of melt depletion (Pearson *et al.*, 2004).

The Penglai peridotites show Os depletion relative to Ir, and are also depleted in Pt and Pd (Fig. 9b). Their $(Os/Ir)_N$ range from 0·13 to 0·63, much lower than those from the Mengyin xenoliths (Fig. 9d). Similar, dramatic fractionation of Os from Ir has been noted in peridotitic xenoliths from Vitim, Siberia (Pearson *et al.*, 2004) and North Queensland, Australia (Handler *et al.*, 1999), and has previously been attributed to Os loss due to syn- or post-eruption sulfide breakdown and alteration (Handler *et al.*, 1999; Pearson *et al.*, 2004). Moreover, the $(Pt/Ir)_N$ and $(Pd/Ir)_N$ values of the Penglai xenoliths are mostly less than unity (Fig. 9e and f). Harzburgite PL18 has the lowest $(Pd/Ir)_N$ value, consistent with its unradiogenic Os isotopic ratio.

The Shanwang xenoliths show large variations in PGE concentrations (Table 8). In contrast to peridotites from Mengyin and Penglai, this suite of xenoliths does not show significant fractionation between IPGE and PPGE (Fig. 9c). Although the Shanwang xenoliths have almost the same $(Os/Ir)_N$ values as those from Mengyin, their $(Ru/Ir)_N$, $(Pt/Ir)_N$ and $(Pd/Ir)_N$ values are much higher (Fig. 9e and f), and some samples have PGE + Re patterns similar to estimates of PUM (e.g. Becker *et al.*, 2006).

## DISCUSSION

### Limitations to dating lithospheric mantle using the Re–Os isotopic system

It has been shown that Re–Os isotopic systematics can be used to date melt extraction from the mantle, and thus the age of formation of the lithospheric mantle (Shirey & Walker, 1998). The principle is that the daughter element, Os, is strongly compatible in mantle residues, whereas the parent element, Re, is moderately incompatible during mantle melting (Walker *et al.*, 1989). Removal of Re accompanying melt depletion leads to retardation or cessation in the growth of $^{187}Os$. Because of the lack of the parent

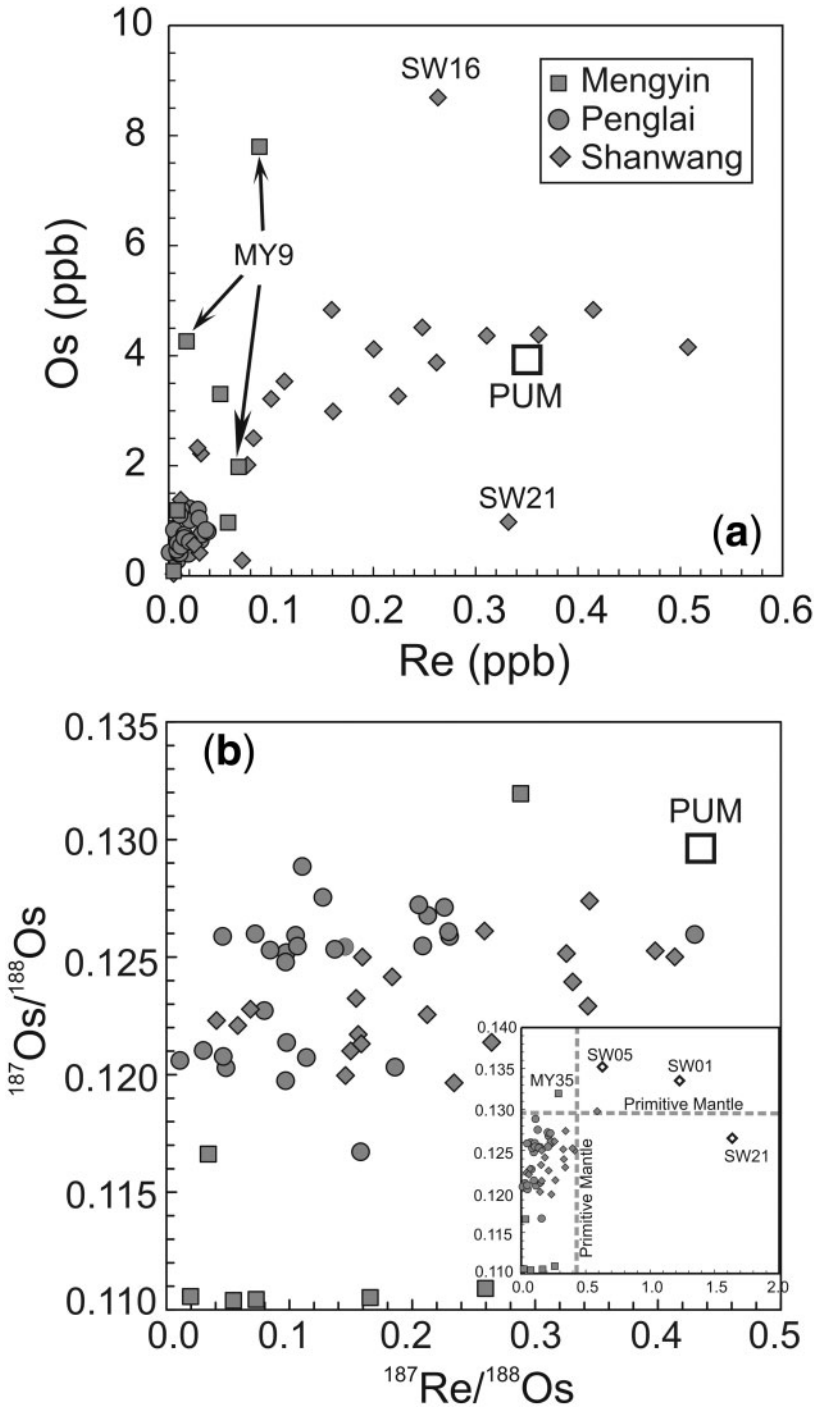


**Fig. 8.** Re–Os (a) and $^{187}Re/^{188}Os$–$^{187}Os/^{188}Os$ (b) variation diagrams for the Mengyin, Penglai and Shanwang xenoliths, (a) PUM (open square) values from Becker *et al.* (2006); (b) the larger panel shows a close-up of the data with $^{187}Re/^{188}Os$ up to 0·5 and the inset shows the full dataset; PUM (open square) values from Meisel *et al.* (2001); open diamonds, wehrlites SW01 and SW21, and Fe-rich lherzolite SW05 from Shanwang that show evidence of metasomatism.

isotope, the residue is relatively immune to subsequent diffusive resetting at high temperatures in mantle peridotites.

The most robust method to date mantle melt depletion using the Re–Os system would be via the generation of whole-rock isochrons. This method, however, is generally not viable for peridotites because of the presumption of lack of isotopic homogeneity in a large mantle domain at the time of melting, and the possible late-stage mobility

*Table 8: PGE elemental compositions of the mantle xenoliths*

| Samples | Os (ppb) | Ir (ppb) | Ru (ppb) | Pt (ppb) | Pd (ppb) | Re (ppb) | $(Os/Ir)_N$ | $(Ru/Ir)_N$ | $(Pt/Ir)_N$ | $(Pd/Ir)_N$ |
|---|---|---|---|---|---|---|---|---|---|---|
| MY9 | 7·80 | 5·52 | 5·11 | 0·76 | 0·43 | 0·089 | 1·31 | 0·59 | 0·06 | 0·06 |
| MY9* | 4·26 | 3·18 | 5·27 | 0·44 | 0·33 | 0·017 | 1·24 | 1·06 | 0·06 | 0·08 |
| MY10* | 0·09 | 0·07 | 0·12 | 0·03 | 0·00 | 0·005 | 1·26 | 1·19 | 0·19 | 0·06 |
| MY33 | 1·19 | 1·48 | 1·63 | 0·15 | 0·09 | 0·008 | 0·75 | 0·70 | 0·05 | 0·05 |
| MY34 | 3·30 | 3·48 | 5·27 | 2·20 | 0·25 | 0·050 | 0·88 | 0·97 | 0·29 | 0·06 |
| MY35 | 0·97 | 0·96 | 1·51 | 0·34 | 0·60 | 0·058 | 0·93 | 1·00 | 0·16 | 0·52 |
| PL01 | 0·28 | 1·99 | 3·23 | 2·78 | 0·94 | 0·008 | 0·13 | 1·04 | 0·63 | 0·39 |
| PL02* | 0·83 | 1·92 | 2·56 | 4·54 | 0·51 | 0·005 | 0·40 | 0·85 | 1·07 | 0·22 |
| PL03 | 0·65 | 2·40 | 2·39 | 3·66 | 1·28 | 0·031 | 0·25 | 0·64 | 0·69 | 0·44 |
| PL03* | 1·15 | 1·69 | 3·76 | 3·61 | 1·26 | 0·523 | 0·63 | 1·42 | 0·96 | 0·62 |
| PL06 | 0·56 | 1·75 | 3·09 | 3·29 | 1·65 | 0·012 | 0·30 | 1·13 | 0·85 | 0·78 |
| PL07* | 0·75 | 1·86 | 4·12 | 3·72 | 1·07 | 0·032 | 0·38 | 1·42 | 0·90 | 0·48 |
| PL08* | 0·43 | 1·03 | 2·53 | 2·22 | 0·51 | 0·001 | 0·38 | 1·58 | 0·97 | 0·41 |
| PL10 | 1·70 | 2·57 | 4·71 | 4·71 | 2·18 | 0·031 | 0·61 | 1·17 | 0·82 | 0·70 |
| PL11* | 1·01 | 1·91 | 2·89 | 4·01 | 0·81 | 0·020 | 0·49 | 0·97 | 0·95 | 0·35 |
| PL12 | 1·60 | 2·83 | 6·08 | 4·04 | 0·93 | 0·033 | 0·53 | 1·38 | 0·64 | 0·27 |
| PL13 | 1·58 | 1·90 | 3·16 | 3·49 | 1·10 | 0·124 | 0·77 | 1·07 | 0·83 | 0·48 |
| PL14* | 0·47 | 1·51 | 2·98 | 2·02 | 0·42 | 0·008 | 0·29 | 1·27 | 0·60 | 0·23 |
| PL15 | 0·74 | 2·11 | 3·50 | 2·38 | 0·83 | 0·017 | 0·33 | 1·06 | 0·51 | 0·32 |
| PL16 | 0·73 | 2·92 | 4·62 | 4·24 | 1·83 | 0·065 | 0·23 | 1·01 | 0·65 | 0·52 |
| PL16* | 1·15 | 2·02 | 5·10 | 4·28 | 1·75 | 0·011 | 0·53 | 1·61 | 0·95 | 0·72 |
| PL17* | 0·69 | 2·11 | 4·20 | 4·47 | 1·01 | 0·015 | 0·30 | 1·28 | 0·95 | 0·40 |
| PL18 | 0·62 | 2·18 | 2·99 | 1·76 | 0·33 | 0·020 | 0·26 | 0·88 | 0·36 | 0·12 |
| PL18* | 1·02 | 2·07 | 3·56 | 1·65 | 0·32 | 0·410 | 0·46 | 1·10 | 0·36 | 0·13 |
| PL19* | 1·04 | 2·03 | 3·49 | 4·44 | 0·98 | 0·030 | 0·48 | 1·10 | 0·99 | 0·40 |
| PL19*-R | 0·83 | 1·94 | 3·42 | 4·50 | 1·00 | 0·036 | 0·40 | 1·13 | 1·05 | 0·43 |
| PL23* | 1·11 | 2·37 | 4·81 | 4·40 | 1·63 | 0·011 | 0·43 | 1·30 | 0·84 | 0·57 |
| SW01 | 0·28 | 0·66 | 0·78 | 0·48 | 0·25 | 0·072 | 0·39 | 0·75 | 0·33 | 0·31 |
| SW02 | 2·99 | 3·39 | 6·71 | 6·76 | 5·31 | 0·161 | 0·82 | 1·27 | 0·90 | 1·30 |
| SW03 | 3·21 | 3·99 | 8·33 | 7·11 | 5·56 | 0·100 | 0·75 | 1·34 | 0·80 | 1·15 |
| SW04 | 2·22 | 3·76 | 6·99 | 6·15 | 5·41 | 0·032 | 0·55 | 1·19 | 0·74 | 1·19 |
| SW05 | 0·04 | 0·23 | 0·40 | 0·11 | 0·09 | 0·005 | 0·15 | 1·11 | 0·22 | 0·32 |
| SW06 | 2·02 | 2·27 | 5·73 | 4·97 | 2·90 | 0·077 | 0·82 | 1·62 | 0·99 | 1·06 |
| SW07 | 1·39 | 1·59 | 2·37 | 2·78 | 1·26 | 0·418 | 0·81 | 0·96 | 0·79 | 0·66 |
| SW07* | 1·38 | 1·28 | 2·32 | 2·82 | 1·31 | 0·012 | 1·01 | 1·17 | 1·00 | 0·85 |
| SW08 | 0·42 | 0·77 | 1·68 | 1·83 | 1·12 | 0·030 | 0·51 | 1·40 | 1·07 | 1·21 |
| SW09 | 1·45 | 2·75 | 4·99 | 6·09 | 2·71 | 0·047 | 0·49 | 1·16 | 1·00 | 0·81 |
| SW09* | 2·33 | 2·55 | 4·77 | 5·83 | 2·60 | 0·028 | 0·85 | 1·20 | 1·03 | 0·84 |
| SW10 | 3·27 | 3·62 | 6·67 | 6·38 | 4·70 | 0·224 | 0·84 | 1·18 | 0·79 | 1·08 |
| SW11* | 4·83 | 3·99 | 8·13 | 7·42 | 4·83 | 0·159 | 1·13 | 1·31 | 0·84 | 1·00 |
| SW12 | 4·15 | 4·67 | 7·48 | 8·49 | 7·31 | 0·508 | 0·83 | 1·03 | 0·82 | 1·30 |
| SW13 | 4·38 | 3·81 | 7·61 | 6·37 | 4·99 | 0·268 | 1·07 | 1·28 | 0·75 | 1·08 |
| SW14 | 3·88 | 3·29 | 7·31 | 6·63 | 5·76 | 0·262 | 1·09 | 1·42 | 0·91 | 1·45 |
| SW15 | 4·51 | 3·79 | 8·35 | 7·45 | 5·40 | 0·248 | 1·11 | 1·41 | 0·89 | 1·18 |
| SW16 | 8·69 | 7·40 | 14·7 | 13·0 | 8·93 | 0·263 | 1·09 | 1·27 | 0·79 | 1·00 |
| SW17 | 3·53 | 2·56 | 5·63 | 6·14 | 4·21 | 0·113 | 1·28 | 1·41 | 1·08 | 1·36 |
| SW18 | 4·83 | 3·94 | 8·49 | 10·1 | 10·2 | 0·415 | 1·14 | 1·38 | 1·15 | 2·14 |
| SW18* | 4·38 | 3·77 | 7·91 | 10·0 | 10·5 | 0·362 | 1·08 | 1·34 | 1·20 | 2·31 |
| SW19 | 2·50 | 2·23 | 5·22 | 5·52 | 3·10 | 0·083 | 1·04 | 1·50 | 1·11 | 1·15 |
| SW20 | 4·12 | 3·34 | 7·61 | 5·50 | 4·04 | 0·200 | 1·14 | 1·46 | 0·74 | 1·00 |
| SW21 | 0·98 | 0·91 | 1·80 | 1·37 | 1·46 | 0·332 | 1·00 | 1·27 | 0·68 | 1·33 |
| SW22 | 0·56 | 0·41 | 1·85 | 0·72 | 0·58 | 0·025 | 1·28 | 2·90 | 0·79 | 1·17 |

All the concentration data are blank-corrected; subscript N indicates chondrite normalized after McDonough & Sun (1995).
*Measured in UMD.

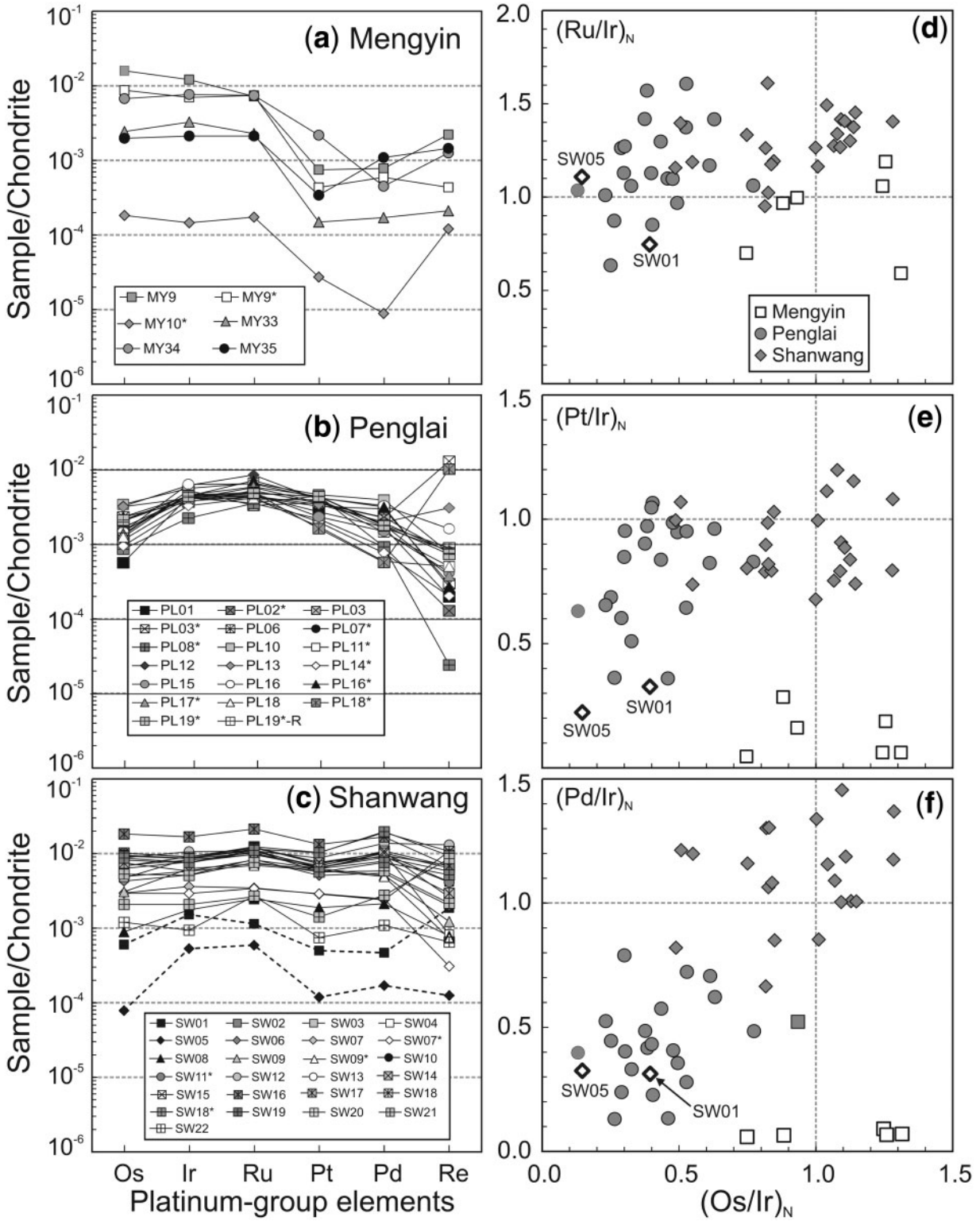


**Fig. 9.** PGE + Re patterns of the Mengyin (a), Penglai (b) and Shanwang (c) peridotites, normalized to the chondrite values of McDonough & Sun (1995). (d–f) PGE ratios. R, replicate analysis. *Measured at UMD. In (c) dashed lines are for wehrlites SW01 and Fe-rich lherzolite SW05 from Shanwang that show evidence of metasomatism. In (d–f) open diamonds show wehrlites SW01 and Fe-rich lherzolite SW05 from Shanwang that probably experienced melt–rock reaction at high melt–rock ratios.

of Re. Consequently, Os model ages for mantle melt residues are more commonly used.

Time of Re depletion ($T_{RD}$) model ages, calculated by assuming that a single melting event removes all of the Re from a peridotite, can provide minimum age constraints for mantle melt depletion (Walker *et al.*, 1989; Shirey & Walker, 1998). $T_{RD}$ ages will significantly underestimate the age of a melt depletion event for samples that have experienced only partial Re removal, such as in the case of lower extents of partial melting, and are applicable for only very highly refractory peridotites (e.g. $Al_2O_3 \leq 1{\cdot}2$ wt %). Model $T_{MA}$ ages may be more accurate (Shirey & Walker, 1998) for peridotites that have undergone only modest melt depletion. They are calculated based on measured $^{187}Re/^{188}Os$, and record the intersection of the isotopic evolution of a sample with a mantle evolution line. However, the accuracy of $T_{MA}$ model ages may be compromised by Re addition or loss during the history of the rock, but especially in transit to the surface in typically high-Re volcanic systems.

Both $T_{RD}$ and $T_{MA}$ model age calculations are subject to some further uncertainties. First, it is clear that the depleted mid-ocean ridge basalt (MORB) mantle (DMM) is not isotopically homogeneous with respect to Os, based on analyses of abyssal peridotites, ophiolites and oceanic basalts. For example, most abyssal peridotites have $^{187}Os/^{188}Os$ ratios ranging from about 0·120 to 0·129 (e.g. Snow & Reisberg, 1995), but some can have substantially lower $^{187}Os/^{188}Os$ (Harvey *et al.*, 2006; C. Z. Liu *et al.*, 2008). Thus, even the modern DMM includes peridotite with ancient melt depletion histories recorded in their Os isotopic compositions (e.g. Parkinson *et al.*, 1998; Brandon *et al.*, 2000; Meibom & Frei, 2002; Meibom *et al.*, 2002; Walker *et al.*, 2002, 2005; Reisberg *et al.*, 2004; Bizimis *et al.*, 2007; Pearson *et al.*, 2007; C. Z. Liu *et al.*, 2008). The ancient Os is evidently undisturbed by mantle stirring because the extremely high partition coefficients for Os in some trace sulfides and alloy phases inhibit loss or gain of Os on a whole-rock scale (Pearson *et al.*, 2004). A single sample with a depleted Os isotopic composition is, therefore, not strong evidence for the presence of ancient mantle, and instead a case for mantle with an ancient provenance must sometimes be made via the distribution of $^{187}Os/^{188}Os$ ratios for a sizeable suite of samples (Rudnick & Walker, 2009).

The second question related to model melt depletion ages is the extent to which a sample may have been affected by melt–rock reaction processes, including metasomatism. Reactions involving melts or fluids with high $^{187}Os/^{188}Os$ can potentially elevate the $^{187}Os/^{188}Os$ ratio of the affected rock and, hence, decrease the apparent melt depletion age. However, most metasomatic fluids and melts have low Os contents and are inefficient at modifying $^{187}Os/^{188}Os$ in peridotites characterized by high Os concentrations (Handler *et al.*, 1997; Shirey & Walker, 1998; Walker *et al.*, 2002; Chesley *et al.*, 2004; Rudnick & Walker, 2009). Only during situations when the melt/fluid–rock ratio is high, such as when lherzolites or harzburgites are transformed into dunite, are such changes noted (e.g. Becker *et al.*, 2001; Büchl *et al.*, 2002). Refertilization can also affect the Os isotopic and PGE composition of peridotites (Saal *et al.*, 2001; Beyer *et al.*, 2006; Rudnick & Walker, 2009). If refertilization occurs shortly following melt extraction, as might be expected in a mantle section that experienced adiabatic melting, refertilization will have no obvious impact on the Re–Os system, as no time has elapsed between melt depletion and refertilization (Rudnick & Walker, 2009). When a large time span separates melt depletion and refertilization, the latter will affect the $^{187}Os/^{188}Os$ of the residual mantle, but to a lesser degree than major elements such as CaO and $Al_2O_3$, which are strongly enriched in the melt relative to the residual peridotite. In this case, refertilization will produce a strongly curved array on an $Al_2O_3$ vs $^{187}Os/^{188}Os$ plot, as $Al_2O_3$ is more strongly affected than $^{187}Os/^{188}Os$ (Reisberg & Lorand, 1995; Rudnick & Walker, 2009). Moreover, as the refertilizing melts are usually incompatible element (e.g. LREE) enriched, it is likely that this signature will be imparted to the refertilized lithospheric mantle and, with time, the $\varepsilon_{Nd}$ and $\varepsilon_{Hf}$ of the residues will become negative.

## Proterozoic lithospheric mantle beneath the eastern NCC during the Paleozoic?

Previous studies have shown that the lithospheric mantle beneath the eastern North China craton was dominated by materials with Archean melt depletion ages during the Paleozoic, as revealed by mantle peridotites and chromite separates from the Paleozoic Mengyin, Fuxian and Tieling kimberlites (Gao *et al.*, 2002; Wu *et al.*, 2006; Zhang *et al.*, 2008). Our three new late Archean $T_{RD}$ model ages (2·4–2·7 Ga) obtained for mantle xenoliths from Mengyin (MY9, MY10 and MY34) are consistent with this prior work. However, one Mengyin sample (MY33) has a $T_{RD}$ age of ~1·6 Ga that is much younger, despite a highly refractory composition (Table 7, Fig. 10a). Gao *et al.* (2002) similarly reported a $T_{RD}$ age of 1·3 Ga, for a refractory whole-rock sample from Mengyin, but its relatively high $^{187}Re/^{188}Os$ of 0·48 made the eruption age correction for this sample potentially problematic. Later, Zhang *et al.* (2008) reported a $T_{RD}$ age of 1·8 Ga for a whole-rock sample collected from the Fuxian kimberlite. Several analyses of chromites from Fuxian and Tieling also yielded $T_{RD}$ ages of 1·6–1·8 Ga (Wu *et al.*, 2006).

The relatively high S concentrations and LREE enrichments in the Mengyin peridotites suggest that these samples experienced strong metasomatic enrichment (Table 1, Fig. 5a), so it may be questioned whether the younger model ages record a Proterozoic melt depletion event or

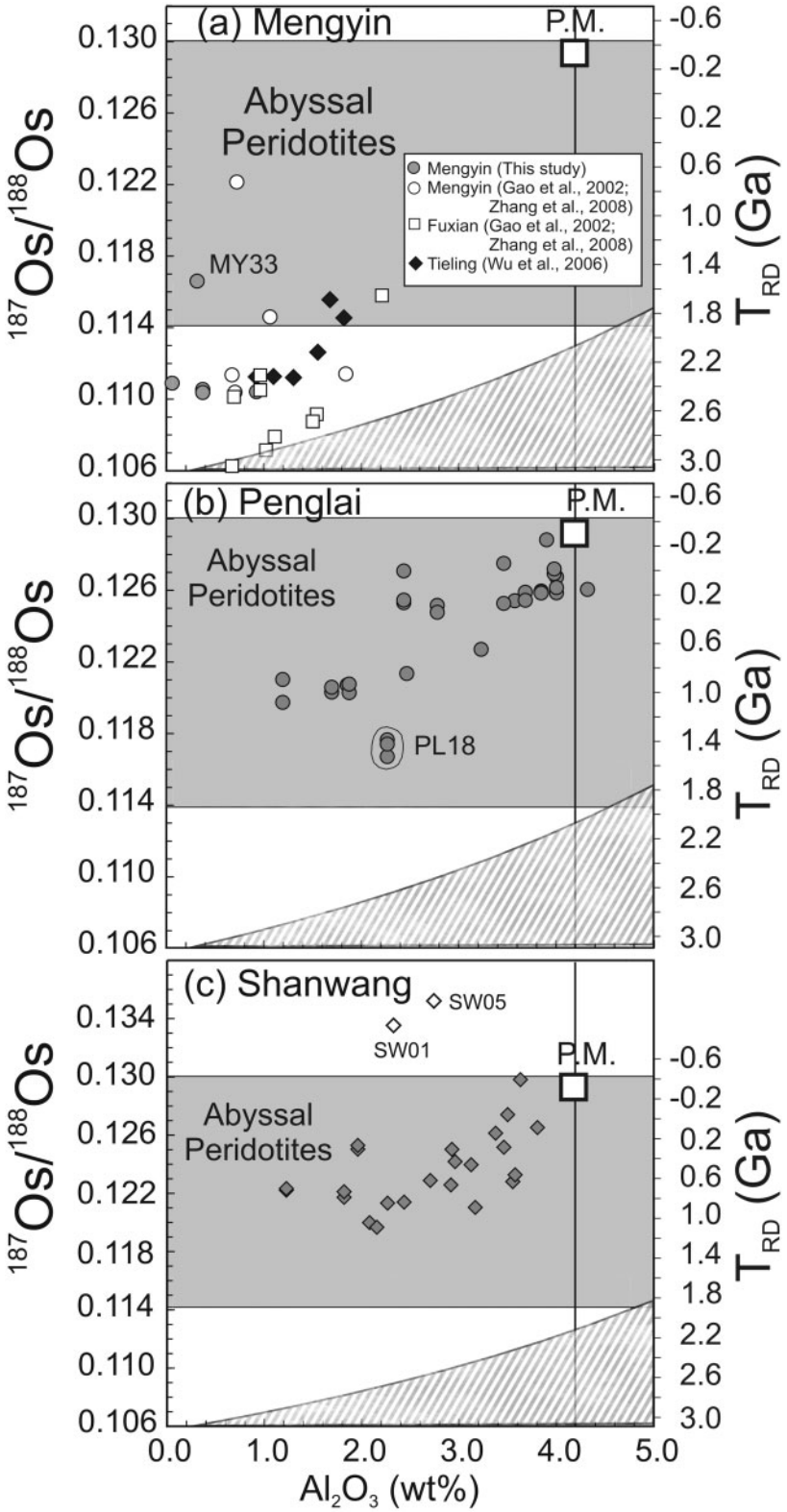


**Fig. 10.** Osmium isotopic compositions vs $Al_2O_3$ (wt %) for peridotites from Mengyin (a), Penglai (b) and Shanwang (c). Other data sources: Mengyin—Gao *et al.* (2002) and Zhang *et al.* (2008); Fuxian—Gao *et al.* (2002) and Zhang *et al.* (2008); Tieling—Wu *et al.* (2006). Osmium isotopic compositions of abyssal peridotites are from Martin (1991), Roy-Barman & Allègre (1994), Snow & Reisberg (1995), Brandon *et al.* (2000), Standish *et al.* (2002), Alard *et al.* (2005), Harvey *et al.* (2006), C. Z. Liu *et al.* (2008); Primitive Upper Mantle (P.M., open square) from Meisel *et al.* (2001, for Os) and McDonough & Sun (1995, for $Al_2O_3$); open diamonds in (c) are wehrlite SW01 and Fe-rich lherzolite SW05 from Shanwang that probably experienced melt–rock reaction at high melt–rock ratios; diagonal shaded area shows refertilization of Archean peridotites (~3 Ga, 3·5 ppb Os, 0·3 wt % $Al_2O_3$ and an $^{187}Os/^{188}Os$ of 0·106) by recent addition of picritic (upper bound, picrite melt with 1 ppb Os, 10 wt % $Al_2O_3$ and an $^{187}Os/^{188}Os$ of 0·15) or basaltic melt (lower bound, basaltic melt has 50 ppt Os, 15 wt % $Al_2O_3$ and an $^{187}Os/^{188}Os$ of 0·15).

complex isotopic systematics resulting from overprinting. However, none of the Mengyin xenoliths studied here show evidence for strong accompanying enrichment of Re (Fig. 8). Moreover, the highly PPGE-depleted Mengyin xenoliths (Fig. 9a), including sample MY33, reflect PPGE removal, rather than addition, consistent with high degrees of melt extraction without subsequent overprinting. Furthermore, IPGE abundances in these rocks are typical of upper mantle materials. Thus, the Os contained in these rocks was probably little affected by the apparent metasomatic event. We conclude that, although the rocks were modified by subsequent processes, the whole-rock model $T_{RD}$ ages may represent the dominant melt depletion age(s) of the peridotites.

Collectively, these data suggest that the Ordovician lithospheric mantle beneath the eastern NCC was dominated by refractory Archean peridotite, containing a minor amount of Proterozoic peridotite. The Proterozoic model ages may provide evidence for minor lithospheric mantle formation as a consequence of Paleo-Mesoproterozoic mantle upwelling related to Columbia supercontinent break-up (Zhai & Liu, 2003; Hou *et al.*, 2008). The limited number of samples, coupled with their highly altered state, precludes a more robust conclusion regarding the absolute age(s) of melt depletion, the proportion of the Proterozoic material and its position in the mantle lithosphere relative to Archean peridotite.

## Effects of secondary processes on Cenozoic mantle xenoliths

The Penglai and many of the Shanwang peridotites appear to have experienced metasomatic overprinting following melt depletion, as reflected by their REE patterns (Fig. 5b and c). Moreover, there are discrepancies in the mass balance of Sr (and Nd) between whole-rocks and cpx in the Shanwang and Penglai peridotites (especially Shanwang). Some samples (e.g. PL11, PL17, PL18, SW02, SW03, SW04, SW10, SW11, SW12, SW19 and SW20) even have higher bulk-rock Sr concentrations than the cpx separates (Tables 1 and 4). As suggested by Rudnick *et al.* (2004), this may reflect one or both of the following: (1) addition of Sr (and Nd) to grain boundaries during metasomatism, host basalt infiltration or post-eruption alteration; (2) the presence of Sr- (and Nd)-bearing accessory phases in the Shanwang and Penglai peridotites. The discrepancies in Sr mass balance in the Shanwang peridotites are greater than those of the Penglai samples, reflecting stronger Sr-rich melt/fluid metasomatism in the Shanwang xenoliths, consistent with their Sr-rich nature (Fig. 5f). Actually, some basalt glass or minor carbonate was identified on grain boundaries in some samples (see Appendix A). Some unleached cpx with slightly higher $^{87}Sr/^{86}Sr$ and lower $^{143}Nd/^{144}Nd$ than their paired leached cpx may be explained by a grain boundary phase that is isotopically slightly more enriched than the cpx (Song & Frey, 1989; Rudnick *et al.*, 2004). Except for sample PL03, unleached cpx have much higher Rb concentrations than their paired, leached cpx. This suggests that Rb is present mainly as a grain boundary phase in the peridotite xenoliths. The Sm/Nd ratios calculated from the whole-rock REE data are lower than those of their paired cpx for many Penglai and Shanwang xenoliths, especially samples PL12, PL17 and PL18. This may also reflect later-stage LREE-rich secondary phase addition to these whole-rocks. The $^{176}Hf/^{177}Hf$ of leached PL19 cpx is slightly higher than its paired, unleached cpx. This may reflect the presence of less radiogenic Hf on the grain boundaries. The positive correlation on the Sm–Nd isochron plot is also consistent with a recent mixing event in the lithospheric mantle under the eastern NCC, where an original LREE-depleted peridotite with positive $\varepsilon_{Nd}$ (e.g. +12) is mixed with a LREE-enriched melt with much lower $\varepsilon_{Nd}$. A rough positive correlation between 1/Nd and $^{143}Nd/^{144}Nd$ (not shown) also supports this mixing hypothesis.

The Penglai xenoliths might have experienced syn- or post-eruption sulfide breakdown, as reflected in their low Os/Ir and high Cu/S (Tables 1 and 8; Fig. 9b) (Handler *et al.*, 1999; Pearson *et al.*, 2004). Collectively, the Penglai and Shanwang data exhibit a rough negative correlation between Os/Ir and whole rock Cu/S (not shown). The Pd/Ir ratios of the Penglai samples are also low, possibly reflecting a high degree of prior melt extraction. As suggested by J. G. Liu *et al.* (2008), another possibility is that the low Pd/Ir ratios of the Pengali xenoliths are also related to syn- or post-eruption sulfide breakdown, as a rough positive correlation exists between the Os/Ir and Pd/Ir ratios for the combined Penglai and Shanwang xenolith data (Fig. 9f).

The higher S concentrations in the Shanwang xenoliths, compared with the Penglai xenoliths, together with significant variations in Re and $^{187}Re/^{188}Os$ (Fig. 8), may indicate that the Re–Os system in some Shanwang xenoliths was influenced by sulfide-bearing melt metasomatism. For example, some Shanwang xenoliths (SW12 and SW21, and especially samples SW01 and SW05) have low Fo numbers, low PGE concentrations, superchondritic $^{187}Re/^{188}Os$, and Os isotopic compositions that are consistent with melt–rock reaction at high melt–rock ratios (Rudnick & Walker, 2009, and references therein).

## Age of the lithospheric mantle beneath the eastern NCC sampled by magmatism during the Cenozoic

Mantle xenoliths from Cenozoic basalts in eastern China give a wide range of Os model ages, from Paleoproterozoic to modern (Gao *et al.*, 2002; Wu *et al.*, 2003, 2006). The meaning of these model ages is highly debated (Gao *et al.*, 2002; Wu *et al.*, 2003, 2006; Xu *et al.*,

2008; Zhang *et al.*, 2008, 2009). Like other mantle xenoliths from Cenozoic basalts in the eastern NCC, the Penglai and Shanwang xenoliths also show Os model ages ranging from Paleoproterozoic to modern.

The Penglai xenoliths (eruption age ~5 Ma) may provide the most robust view of the modern lithospheric mantle beneath the eastern NCC yet available. Although the Penglai xenoliths have experienced variable metasomatic overprinting, as reflected by their REE and trace element characteristics, their PGE patterns do not show PPGE enrichment. Consequently, it is likely that the Re–Os isotope systematics of the Penglai xenoliths were not affected by metasomatic modification. Similarly, although the Penglai xenoliths have experienced post- or syn-eruption sulfide breakdown, as reflected in their low Os/Ir, and high Cu/S, this should not affect their Os isotopic systematics. The Os isotopic compositions of the Penglai xenoliths display a crude positive correlation with $Al_2O_3$ wt % (Fig. 10b). Model ages of relatively refractory samples, harzburgites PL08 and PL23, and cpx-poor lherzolite PL12, are similar at ~1 Ga. The most refractory sample from this locale (based on its low $Al_2O_3$ and CaO contents), harzburgite PL02, which has an olivine Fo-number of 90·8, a Cr-number of 39·4, as well as the lowest HREE concentration in the suite, also has a $T_{RD}$ age of ~1·1 Ga. These model ages are in good agreement with the cpx Lu–Hf errorchron age (~1·3 Ga, Fig. 6c) obtained from the same suite of samples.

Even though there is a fairly close correspondence between the maximum Os and Hf model ages for the Penglai xenolith suite, it should be noted that the two isotope systems do not provide concordant results for single samples. For example, the two Penglai samples that define the Hf errorchron age by having very radiogenic Hf (PL11 and PL19), indicating long-term LREE (and Hf) depletion, have $^{187}Os/^{188}Os$ isotope ratios typical of the modern convecting upper mantle (i.e. 0·12499 and 0·12597, with corresponding $T_{RD}$ ages of 0·3–0·2 Ga, respectively) (Tables 6 and 7). The reason for these age discordancies for single samples is unclear, but probably relates to the very different behavior of lithophile and highly siderophile elements in the upper mantle.

The Shanwang xenoliths, located within the Tan–Lu Fault, are also typical examples of the young lithospheric mantle beneath the NCC during the Cenozoic (Zhang *et al.*, 2006; Zheng *et al.*, 2007). Although the Shanwang samples have experienced some sulfide metasomatism, as mentioned above, most samples have PUM-like PGE + Re characteristics and high Os concentrations (except for SW01 and SW05), implying that their Re–Os isotopes have not been strongly affected (Pearson *et al.*, 2004; Reisberg *et al.*, 2004, 2005; Rudnick & Walker, 2009). The Os isotopic ratios of the Shanwang xenoliths show a crude negative correlation with the Fo-numbers of the olivine in the samples (not shown), and a crude positive correlation with the $Al_2O_3$ wt % of the bulk samples (Fig. 10c). There is also a rough positive correlation between Os isotopic ratios and $(Pd/Ir)_N$ (not shown). Collectively, these characteristics suggest that the different Os isotopic ratios relate to the fertility of the xenoliths. The model ages of relatively refractory Shanwang samples range from 0·8 to 1·0 Ga.

Although mid-Proterozoic Os $T_{RD}$ ages are obtained for refractory xenoliths from both Penglai and Shanwang, it cannot be immediately concluded that this mantle lithosphere formed in the mid-Proterozoic. The modern DMM, as recorded by abyssal peridotites and young ophiolites, includes peridotites with ancient melt depletion histories (back to 2·0 Ga) recorded in their Os isotopic compositions. As suggested by Rudnick & Walker (2009), for post-Archean peridotites, it is necessary to make statistical comparisons via measurement of $^{187}Os/^{188}Os$ ratios for a sizeable suite of samples to assess whether or not the xenoliths are like the DMM or record an older average melt depletion.

As shown in Fig. 11, the overall distribution of $^{187}Os/^{188}Os$ for the Penglai and Shanwang samples, as well as for other Cenozoic mantle xenoliths from the eastern NCC, is similar to that of the modern convecting mantle. Their isotopic compositions are very different from the Paleozoic xenoliths from the eastern NCC (Fig. 11). Combined with the fact that the Sr–Nd–Hf isotope compositions of the Cenozoic mantle xenoliths from the eastern NCC are mostly similar to the modern convecting mantle (Fig. 7), it is likely that the present lithospheric mantle beneath the eastern NCC is juvenile, and formed during the Mesozoic or Cenozoic.

Recent analyses suggest that materials in the suboceanic mantle can also retain a long-term Hf isotopic depletion history (Salters & Zindler, 1995; Andres *et al.*, 2004; Graham *et al.*, 2006; Bizimis *et al.*, 2007). It is possible that the convecting mantle contains materials with high Hf isotopic ratios that never were homogenized, as is surmised for Os. In contrast, all data for the Sm–Nd isotope system suggest that it is more efficiently homogenized, supporting the conclusion that the Lu–Hf isotope system has a higher closure temperature than the Sm–Nd and Rb–Sr systems (e.g. Bedini *et al.*, 2004; Wittig *et al.*, 2006, 2007). Therefore, although a cpx Lu–Hf errorchron of 1·3 Ga was obtained, the Lu–Hf results provide permissive evidence that the lithospheric mantle currently underlying the eastern portion of the NCC was formed during the Mesozoic or Cenozoic from the convective upper mantle.

The conclusion that the present lithospheric mantle beneath the eastern NCC is juvenile may be consistent with the regional geology. Neodymium model ages that are mostly between 2·5 and 2·9 Ga indicate that the NCC was formed during the Archean (Wu *et al.*, 2005*b*).

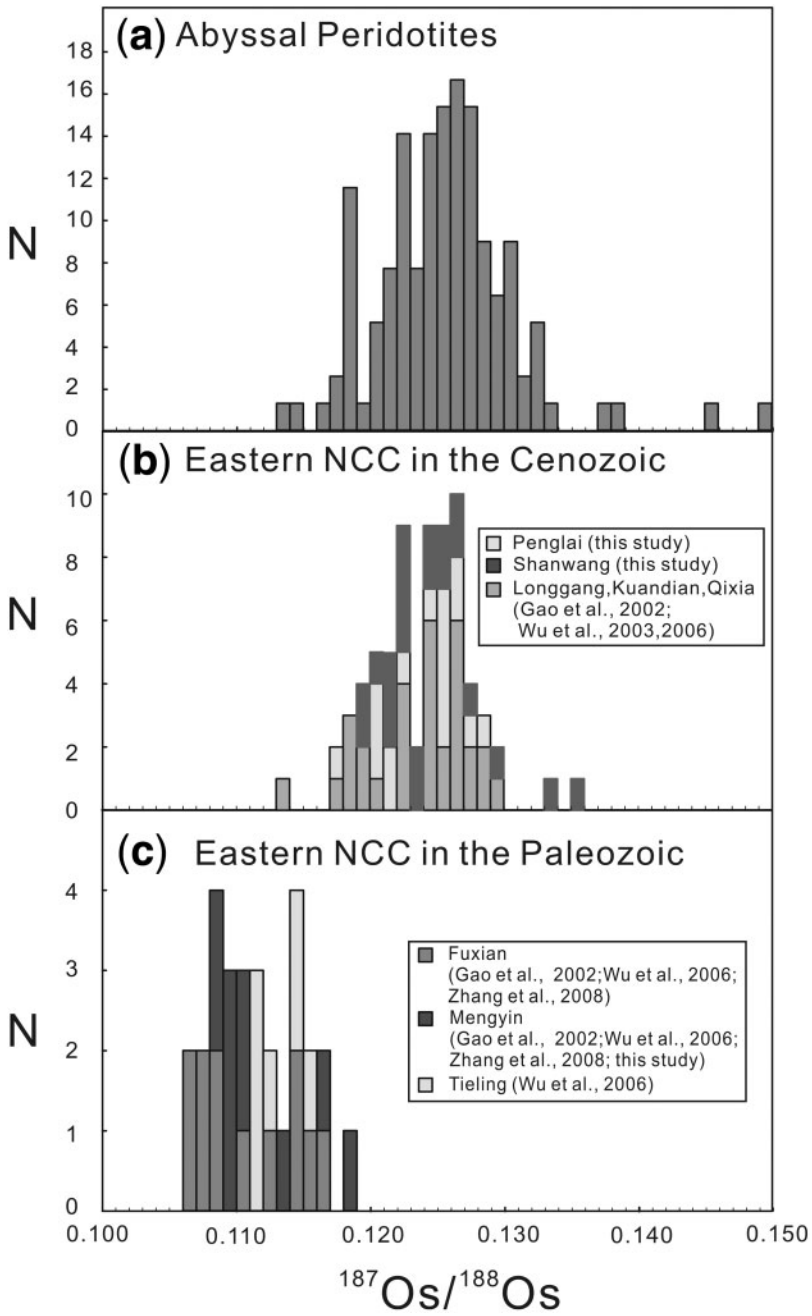


**Fig. 11.** Comparison of Os isotopic compositions in modern abyssal peridotites and mantle xenoliths from the North China Craton. (a) Abyssal peridotites (data sources as in Fig. 10), (b) eastern North China Craton in the Cenozoic (Gao *et al.*, 2002; Wu *et al.*, 2003, 2006; this study), and (c) eastern North China Craton in the Early Paleozoic (Gao *et al.*, 2002; Wu *et al.*, 2006; Zhang *et al.*, 2008; this study).

At ~1·85 Ga, the NCC underwent cratonization by amalgamation of the eastern and western blocks (Zhao *et al.*, 2005), and the crust experienced reworking without any juvenile addition. The NCC remained stable during the Proterozoic and Paleozoic, although very minor amounts of anorogenic rapakivi granite and anorthosite have been identified locally (Ramo *et al.*, 1995; Yang *et al.*, 2005; S. H. Zhang *et al.*, 2007). During the late Paleozoic, the northern margin of the NCC served as an active continental margin characterized by subduction of the Paleo-Asian Ocean to the north (S. H. Zhang *et al.*, 2009). It was not until the Mesozoic that extensive igneous activity occurred throughout the NCC, with significant growth of juvenile crust (Wu *et al.*, 2005*a*; Yang *et al.*, 2008). The addition of

juvenile lithospheric mantle beneath the NCC during the Mesozoic may, thus, have accompanied the creation of new crust (Wu *et al.*, 2005*a*).

## Constraints on the mechanism of lithospheric thinning beneath the NCC

It is widely accepted that a significant part of the deep lithosphere beneath the eastern NCC was removed during the Mesozoic. However, the time, extent, mechanism, and geodynamic setting of the thinning of the lithospheric mantle underlying the eastern NCC is still highly debated (Menzies *et al.*, 2007). Several mechanisms have been proposed to explain the lithospheric thinning, including delamination (e.g. Gao *et al.*, 2002, 2004, 2008; Wu *et al.*, 2005*a*, 2007), thermo-mechanical erosion (e.g. Xu, 2001; Zheng *et al.*, 2007) and lithospheric transformation through peridotite–melt interaction or chemical erosion (e.g. Zhang, 2005; Zhang *et al.*, 2006, 2008, 2009; Ying *et al.*, 2006; Tang *et al.*, 2008).

If thermo-mechanical erosion of the lithosphere induced by the upwelling of the asthenosphere took place gradually from the base of the lithosphere, a stratified lithospheric mantle can be envisaged, with an Archean relict lithosphere overlying newly accreted lithosphere (Griffin *et al.*, 1998; Menzies & Xu, 1998). If asthenospheric upwelling preferentially focused along weak shear zones in the Archean root (e.g. Zheng *et al.*, 2007), then the Archean lithospheric mantle would be dispersed in the newly accreted, Phanerozoic lithospheric mantle. However, the lithospheric mantle sampled during the Paleozoic appears to have been mostly Archean (Gao *et al.*, 2002; Wu *et al.*, 2006; Zhang *et al.*, 2008; this study), whereas in the Cenozoic the mantle lithosphere appears to be exclusively juvenile, with no Archean material identified amongst the xenoliths studied to date (Gao *et al.*, 2002; Wu *et al.*, 2003, 2006; this study). The observation that both garnet- and spinel-facies mantle peridotite xenoliths from the Mengyin and Fuxian kimberlites have Archean Re–Os isotopic ages indicates no chemical stratification of the Archean lithospheric mantle beneath the eastern NCC (Zhang *et al.*, 2008). Furthermore, recent studies indicate that peridotite xenoliths hosted by the Mesozoic (~125 Ma) Laiwu diorites are refractory, have low equilibration temperatures, and have enriched Sr–Nd isotopic compositions, similar to peridotites from Mengyin (W. L. Xu *et al.*, 2008). The lack of garnet in the xenoliths indicates that they were derived from depths <80 km. Osmium isotopic compositions indicate that the Laiwu xenoliths are Archean (Gao *et al.*, 2008), similar to those from Mengyin. These results further confirm that the refractory, Paleozoic lithospheric mantle beneath the eastern NCC is not stratified. We conclude that the Cenozoic lithospheric mantle is not the upper part of the Paleozoic lithospheric mantle or a relict after thinning.

A key question remains as to whether peridotite–melt interaction or melt addition converted the pre-existing refractory lithospheric mantle beneath the eastern NCC into fertile mantle, as suggested by recent studies calling upon lithospheric transformation or refertilization (Zhang, 2005; Zhang *et al.*, 2006, 2008, 2009; Ying *et al.*, 2006; Tang *et al.*, 2008). However, as stated above, because most metasomatic fluids and melts have Os contents two to three orders of magnitude lower than those of the peridotites, it is seemingly difficult to transform peridotites with Archean Os model ages to peridotites with Proterozoic or Phanerozoic model ages through recent melt addition (see also Rudnick & Walker, 2009). Furthermore, if refertilization occurred much later than the formation of the peridotites, it should be recognizable on a plot of $Al_2O_3$ vs $^{187}Os/^{188}Os$ as a curved trend. As shown in Fig. 10, the Os isotopic ratios display a crude positive correlation with $Al_2O_3$ for both the Penglai and Shanwang xenoliths, and lie far above the shaded area within which they would plot if they represented Archean lithosphere (~3 Ga, 3·5 ppb Os, 0·3 wt % $Al_2O_3$ and an $^{187}Os/^{188}Os$ of 0·106) that had experienced recent melt addition (upper bound, picrite melt with 1 ppb Os, 10 wt % $Al_2O_3$ and an $^{187}Os/^{188}Os$ of 0·15; lower bound, basaltic melt with 50 ppt Os, 15 wt % $Al_2O_3$ and an $^{187}Os/^{188}Os$ of 0·15). Collectively, the data do not support the idea that the Cenozoic peridotites are Archean peridotites that have experienced significant melt addition in the Mesozoic or later. As argued above, the Shanwang xenoliths may have experienced intensive sulfide-bearing melt metasomatism. However, even if sulfides were precipitated, the metasomatized mantle should show significant enrichment of PPGE along with high Re/Os ratios (Pearson *et al.*, 2004; Reisberg *et al.*, 2004, 2005; Rudnick & Walker, 2009), which are not observed in most Shanwang xenoliths. Moreover, secondary sulfides typically have one to two orders of magnitude lower Os content than primary sulfides (Alard *et al.*, 2000), which means it may also be difficult to transform peridotites with Archean Os model ages to peridotites with Proterozoic or Phanerozoic model ages through recent sulfide metasomatism (Gao *et al.*, 2002; Reisberg *et al.*, 2004, 2005). Collectively, the present-day lithospheric mantle beneath the eastern NCC is probably not refertilized or metasomatized Archean lithospheric mantle.

It has been long recognized that the mantle lithosphere that existed beneath the eastern NCC during the Paleozoic was highly refractory, with an enriched Sr–Nd isotope composition, in contrast to the lithospheric mantle that underlies this region at present, which is fertile and has a Sr–Nd isotope composition similar to that of the depleted mantle (e.g. Griffin *et al.*, 1998; Menzies *et al.*, 2007), as shown in the present study (Fig. 7). We have also shown on the basis of Os isotopes that the Archean

lithosphere was replaced after the Ordovician by juvenile lithospheric mantle that has Os isotopic characteristics indistinguishable from the modern convecting upper mantle (Fig. 11). Overall, the present lithospheric mantle beneath the eastern NCC is completely different from that present in the Paleozoic, and is much younger than its overlying Archean crust. It is possible that the ancient lithospheric mantle beneath the eastern NCC was removed by foundering during the Mesozoic or later, and replaced by the cooled product of upwelling asthenospheric mantle. Combined with other lines of evidence from Mesozoic magmatic rocks (e.g. Gao *et al.*, 2004, 2008; Wu *et al.*, 2005*a*), the delamination model is our preferred mechanism to account for the loss of the ancient keel that once underlay the North China Craton.

## CONCLUSIONS

(1) Archean Re–Os model ages for peridotite xenoliths hosted by the Paleozoic Mengyin diamondiferous kimberlites provide further evidence that Archean lithospheric mantle dominated the eastern North China Craton lithosphere during the Paleozoic. Our new data also indicate that minor Paleoproterozoic lithosphere was also present.

(2) Like peridotite xenoliths from other Cenozoic basalts in the eastern North China Craton, the Shanwang and Penglai xenoliths have Os model ages that range back to the Mesoproterozoic. The distribution of Os isotopic compositions for these xenoliths, however, is identical to that seen in modern abyssal peridotites, which sample the present-day convecting mantle. This similarity between Cenozoic lithosphere and abyssal peridotites suggests that this lithosphere formed during the Mesozoic or Cenozoic; it is unlikely that the present lithospheric mantle beneath the eastern NCC was refertilized or metasomatized Archean lithospheric mantle.

(3) The high initial $\varepsilon_{Nd}$ (5–24, average = 10) and $\varepsilon_{Hf}$ (7–75, average = 25, excluding the two very radiogenic samples) and low $^{87}Sr/^{86}Sr$ (0·7023–0·7042, average = 0·7030) of cpx from the Cenozoic peridotites are consistent with their derivation from convecting upper mantle during the Mesozoic or Cenozoic.

(4) Nd–Hf isotope decoupling in cpx from the Penglai peridotites indicates that the convecting upper mantle may contain materials with radiogenic Hf isotopic ratios, similar to the ancient Os that is occasionally recorded in abyssal peridotites, whereas Nd isotopes do not reflect such ancient melt depletions.

## ACKNOWLEDGEMENTS

Yan-Bin Zhang, Chao-Feng Li, Qian Mao, Yu-Guang Ma, He Li, Jie Cao, and Jianfeng Gao are thanked for their help in obtaining trace elemental, Sr–Nd isotopic, EPMA, XRF and PGE data. Chuan-zhou Liu, Ji-feng Ying, Qin Zhou and Zhi-chao Liu are thanked for their help with the photomicrography. We also thank J. Blusztajn, H. Becker and an anonymous reviewer for their constructive reviews. This work was financially supported by National Natural Science Foundation of China (NSFC Grants 40634019) and the US National Science Foundation (EAR 0635671).

## SUPPLEMENTARY DATA

Supplementary data for this paper are available at *Journal of Petrology* online.

## REFERENCES

Alard, O., Griffin, W. L., Lorand, J. P., Jackson, S. E. & O'Reilly, S.Y. (2000). Non-chondritic distribution of the highly siderophile elements in mantle sulphides. *Nature* **407**, 891–894.

Alard, O., Luguet, A., Pearson, N. J., Griffin, W. L., Lorand, J. P., Gannoun, A., Burton, K. W. & O'Reilly, S. Y. (2005). *In situ* Os isotopes in abyssal peridotites bridge the isotopic gap between MORBs and their source mantle. *Nature* **436**, 1005–1008.

Andres, M., Blichert-Toft, J. & Schilling, J. G. (2004). Nature of the depleted upper mantle beneath the Atlantic: evidence from Hf isotopes in normal mid-ocean ridge basalts from 79°N to 55°S. *Earth and Planetary Science Letters* **225**, 89–103.

Becker, H., Shirey, S. B. & Carlson, R. W. (2001). Effects of melt percolation on the Re–Os systematics of peridotites from a Paleozoic convergent plate margin. *Earth and Planetary Science Letters* **188**, 107–121.

Becker, H., Carlson, R. W. & Shirey, S. B. (2004). Slab-derived osmium and isotopic disequilibrium in garnet pyroxenites from a Paleozoic convergent plate margin (lower Austria). *Chemical Geology* **208**, 141–156.

Becker, H., Horan, M. F., Walker, R. J., Gao, S., Lorand, J. P. & Rudnick, R. L. (2006). Highly siderophile element composition of the Earth's primitive upper mantle: Constraints from new data on peridotite massifs and xenoliths. *Geochimica et Cosmochimica Acta* **70**, 4528–4550.

Bedini, R. M., Blichert-Toft, J., Boyet, M. & Albarède, F. (2004). Isotopic constraints on the cooling of the continental lithosphere. *Earth and Planetary Science Letters* **223**, 99–111.

Bertrand, P. & Mercier, J. C. (1985). The mutual solubility of coexisting ortho- and clinopyroxene: toward an absolute geothermometer for the natural system? *Earth and Planetary Science Letters* **76**, 109–122.

Beyer, E. E., Griffin, W. L. & O'Reilly, S. Y. (2006). Transformation of Archean lithospheric mantle by refertilization: evidence from exposed peridotites in the Western Gneiss Region, Norway. *Journal of Petrology* **47**, 1611–1636.

Birck, J. L., Roy-Barman, M. & Capmas, F. (1997). Re–Os isotopic measurements at the femtomole level in natural samples. *Geostandards Newsletter* **20**, 19–27.

Bizimis, M., Griselin, M., Lassiter, J. C., Salters, V. J. M. & Sen, G. (2007). Ancient recycled mantle lithosphere in the Hawaiian plume: osmium–hafnium isotopic evidence from peridotite mantle xenoliths. *Earth and Planetary Science Letters* **257**, 259–273.

Boyd, F. R. (1989). Compositional distinction between oceanic and cratonic lithosphere. *Earth and Planetary Science Letters* **96**, 15–26.

Brandon, A. D., Snow, J. E., Walker, R. J., Morgan, J. W. & Mock, T. D. (2000). $^{190}Pt$–$^{186}Os$ and $^{187}Re$–$^{187}Os$ systematics of abyssal peridotites. *Earth and Planetary Science Letters* **177**, 319–335.

Brey, G. P. & Kohler, T. (1990). Geothermobarometry in four-phase lherzolites II: new thermobarometers, and practical assessment of existing thermobarometers. *Journal of Petrology* **31**, 1353–1378.

Büchl, A., Brügmann, G., Batanova, V. G., Münker, C. & Hofmann, A. W. (2002). Melt percolation monitored by Os isotopes and HSE abundances: a case study from the mantle section of the Troodos ophiolite. *Earth and Planetary Science Letters* **204**, 385–402.

Carlson, R. W., Pearson, D. G. & James, D.E. (2005). Physical, chemical, and chronological characteristics of continental mantle. *Review of Geophysics* **43**, 2004RG000156.

Chen, L., Zheng, T. Y. & Xu, W. W. (2006). A thinned lithospheric image of the Tanlu Fault Zone, eastern China: constructed from wave equation based receiver function migration. *Journal of Geophysical Research* **111**, B09312, doi:10.1029/2005JB003974.

Chesley, J., Righter, K. & Ruiz, J. (2004). Large-scale mantle metasomatism: a Re–Os perspective. *Earth and Planetary Science Letters* **219**, 49–60.

Chi, J. S. & Lu, F. X. (1996). *Kimberlites and the features of Paleozoic lithospheric mantle in North China craton*. Beijing: Science Press, 292 pp.

Chu, Z. Y., Chen, F. K., Wang, W., Xie, L. W. & Yang, Y.H. (2007). High-precision measurement for the concentration and isotopic composition of Rhenium and Osmium in micro-amount of geological samples (in Chinese with English abstract). *Rock and Mineral Analysis* **26**, 431–435.

Cohen, A. S. & Waters, F. G. (1996). Separation of osmium from geological materials by solvent extraction for analysis by TIMS. *Analytica Chimica Acta* **332**, 269–275.

Dobbs, P. N., Duncan, D. J., Hu, S., Shee, S. R., Colgan, E. A., Brown, M. A., Smith, C. B. & Allsopp, H. P. (1994). The geology of Mengyin kimberlites, Shandong, China. In: Meyer, O. A. & Leonardos, O. H. (eds) *Kimberlites, Related Rocks and Mantle Xenoliths. CPRM Special Publication* **1A/93**, 40–61.

Dulski, P. (2001). Reference materials for geochemical studies: new analytical data by ICP-MS and critical discussion of reference values. *Geostandards and Geoanalytical Research* **25**, 87–125.

Fan, W. M. & Menzies, M. A. (1992). Destruction of aged lower lithosphere and accretion of asthenosphere mantle beneath eastern China. *Geotectonica et Metallogenia* **16**, 171–180.

Fan, W. M., Zhang, H. F., Baker, J., Jarvis, K. E., Mason, P. R. D. & Menzies, M. A. (2000). On and off the North China craton: where is the Archean keel? *Journal of Petrology* **41**, 933–950.

Faure, M., Lin, W., Monie, P. & Bruguier, O. (2004). Paleoproterozoic arc magmatism and collision in Liaodong Peninsula (north-east China). *Terra Nova* **16**, 75–80.

Foley, S. F. (2008). Rejuvenation and erosion of the cratonic lithosphere. *Nature Geoscience* **1**, 503–510.

Gao, S., Rudnick, R. L., Carlson, R. W., McDonough, W. F. & Liu, Y. S. (2002). Re–Os evidence for replacement of ancient mantle lithosphere beneath the North China Craton. *Earth and Planetary Science Letters* **198**, 307–322.

Gao, S., Rudnick, R. L., Yuan, H. L., Liu, X. M., Liu, Y. S., Xu, W. L., Ling, W. L., Ayers, J., Wang, X. C. & Wang, Q. H. (2004). Recycling lower continental crust in the North China craton. *Nature* **432**, 892–897.

Gao, S., Rudnick, R. L., Xu, W. L., Yuan, H. L., Liu, Y. S., Walker, R. J., Puchtel, I., Liu, X. M., Huang, H., Wang, X. R. & Yang, J. (2008). Recycling deep cratonic lithosphere and generation of intraplate magmatism in the North China Craton. *Earth and Planetary Science Letters* **270**, 41–53.

Govindaraju, K. (1994). 1994 compilation of working values and sample description for 383 geostandards. *Geostandards Newsletter* **18**(Special Issue), 1–158.

Graham, D. W., Blichert-Toft, J., Russo, C. J., Rubin, K.H. & Albarède, F. (2006). Cryptic striations in the upper mantle revealed by hafnium isotopes in southeast Indian ridge basalts. *Nature* **440**, 199–202.

Griffin, W. L., Zhang, A. D., O'Reilly, S. Y. & Ryan, C. G. (1998). Phanerozoic evolution of the lithosphere beneath the Sino-Korean craton. In: Flower, M. F. J., Chung, S. L., Lo, C. H. & Lee, T. Y. (eds) *Mantle Dynamics and Plate Interactions in East Asia. American Geophysical Union, Geodynamic Series* **27**, 107–126.

Griffin, W. L., O'Reilly, S. Y. & Ryan, C. G. (1999). The composition and origin of sub-continental lithospheric mantle. In: Fei, Y., Bertka, M. & Mysen, B. O. (eds) *Mantle Petrology: Field Observations and High-Pressure Experimentation. A Tribute to France R. (Joe) Boyd. Geochemical Society Special Publications* **6**, 13–46.

Handler, M. R., Bennett, V. C. & Esat, T. Z. (1997). The persistence of off-cratonic lithospheric mantle: Os isotopic systematics of variably metasomatised southeast Australian xenoliths. *Earth and Planetary Science Letters* **151**, 61–75.

Handler, M. R., Bennett, V. C. & Dreibus, G. (1999). Evidence from correlated Ir/Os and Cu/S for late-stage Os mobility in peridotite xenoliths: Implications for Re–Os systematics. *Geology* **27**, 75–78.

Harvey, J., Gannoun, A., Burton, K. W., Rogers, N. W., Alard, O. & Parkinson, I. J. (2006). Ancient melt extraction from the oceanic upper mantle revealed by Re–Os isotopes in abyssal peridotites from the Mid-Atlantic ridge. *Earth and Planetary Science Letters* **244**, 606–621.

Hermann, W. & Berry, R. F. (2002). MINSQ—a least squares spreadsheet method for calculating mineral proportions from whole rock major element analyses. *Geochemistry: Exploration, Environment, Analysis* **2**, 361–368.

Hou, G. T., Li, J. H., Yao, W. H., Wang, C. C. & Wang, Y. X. (2008). Geochemical constraints on the tectonic environment of the Late Paleoproterozoic mafic dyke swarms in the North China Craton. *Gondwana Research* **13**, 103–116.

Lee, C. T. & Rudnick, R. L. (1999). Compositionally stratified cratonic lithosphere: petrology and geochemistry of peridotite xenoliths from the Labait volcano, Tanzania. In: Gurney, J. J., Gurney, J. L., Pascoe, M. D. & Richardson, S. R. (eds) *The P. H. Nixon Volume, Proceedings of 7th Internation Kimberlite Conference*. Cape Town: Red Roof Design, pp. 503–521.

Liu, C. Z., Snow, J. E., Hellebrand, E., Brügmann, G., von der Handt, A., Büchl, A. & Hofmann, A. W. (2008). Ancient, highly heterogeneous mantle beneath Gakkel Ridge, Arctic Ocean. *Nature* **452**, 311–316.

Liu, D. Y., Nutman, A. P., Compston, W., Wu, J. S. & Shen, Q. H. (1992). Remnants of >3800 Ma crust in the Chinese part of the Sino-Korean Craton. *Geology* **20**, 339–342.

Liu, J. G., Rudnick, R. L., Walker, R. J., Gao, S. & Wu. F.-Y. (2008). The age of mantle lithosphere on the northernmost margin of the Central Orogenic Belt, North China Craton. In: Abstracts, 9th International Kimberlite Conference, Frankfurt. World Wide Web Address: http://www·9ikc.uni-frankfurt.de/index.html.

Liu, J. Q. (1999). *Active Volcanoes in China (in Chinese)*. Beijing: Science Press, 219 pp.

Lu, X. P., Wu, F. Y., Guo, J. H., Wilde, S. A., Yang, J. H., Liu, X. M. & Zhang, X. O. (2006). Zircon U–Pb geochronological constraints on the Paleoproterozoic crustal evolution of the Eastern Block in the North China Craton. *Precambrian Research* **146**, 138–164.

Makishima, A. & Nakamura, E. (2006). Determination of major, minor and trace elements in silicate samples by ICP-QMS and ICP-SFMS applying isotope dilution-internal standardisation (ID-IS) and multi-stage internal standardisation. *Geostandards and Geoanalytical Research* **30**, 245–271.

Martin, C. E. (1991). Osmium isotopic characteristics of mantle-derived rocks. *Geochimica et Cosmochimica Acta* **55**, 1421–1434.

Masuda, A., Nakamura, N. & Tanaka, T. (1973). Fine structures of mutually normalised rare-earth patterns of chondrites. *Geochimica et Cosmochimica Acta* **37**, 239–244.

McDonough, W. F. & Frey, F. A. (1989). Rare earth elements in upper mantle rocks. In: Lipin, B. R. & McKay, G. A. (eds) *Geochemistry and Mineralogy of Rare Earth Elements. Mineralogical Society of America, Reviews in Mineralogy* **21**, 99–145.

McDonough, W. F. & Sun, S. S. (1995). The composition of the Earth. *Chemical Geology* **120**, 223–253.

Meibom, A. & Frei, R. (2002). Evidence for an ancient osmium isotopic reservoir in Earth. *Science* **296**, 516–518.

Meibom, A., Sleep, N. H., Chamberlain, C. P., Coleman, R. G., Frei, R., Hren, M. T. & Wooden, J. L. (2002). Re–Os isotopic evidence for long-lived heterogeneity and equilibration processes in Earth's upper mantle. *Nature* **419**, 705–708.

Meisel, T., Walker, R. J., Irving, A. J. & Lorand, J. P. (2001). Osmium isotopic compositions of mantle xenoliths: a global perspective. *Geochimica et Cosmochimica Acta* **65**, 1311–1323.

Menzies, M. A. & Xu, Y. G. (1998). Geodynamics of the North China Craton. In: Flower, M. F. J., Chung, S. L., Lo, C. H. & Lee, T. Y. (eds) *Mantle Dynamics and Plate Interactions in East Asia. American Geophysical Union, Geodynamic Series* **27**, 155–165.

Menzies, M. A., Fan, W. M. & Zhang, M. (1993). Palaeozoic and Cenozoic lithoprobe and the loss of >120 km of Archean lithosphere, Sino-Korean craton, China. In: Prichard, H. M., Alabaster, T., Harris, N. B. W. & Neary, C. R. (eds) *Magmatic Processes and Plate Tectonics. Geological Society, London, Special Publications* **76**, 71–81.

Menzies, M. A., Xu, Y. G., Zhang, H. F. & Fan, W. M. (2007). Integration of geology, geophysics and geochemistry: A key to understanding the North China Craton. *Lithos* **96**, 1–21.

Nowell, G. M., Kempton, P. D., Noble, S. R., Fitton, J. G., Saunders, A. D., Mahoney, J. J. & Taylor, R. N. (1998). High precision Hf isotope measurements of MORB and OIB by thermal ionization mass spectrometry: Insights into the depleted mantle. *Chemical Geology* **149**, 211–233.

Parkinson, I. J., Hawkesworth, C. J. & Cohen, A. S. (1998). Ancient mantle in a modern arc: osmium isotopes in Izu–Bonin–Mariana forearc peridotites. *Science* **281**, 2011–2013.

Pearson, D. G. & Woodland, S. J. (2000). Solvent extraction/anion exchange separation and determination of PGEs (Os, Ir, Pt, Pd, Ru) and Re–Os isotopes in geological samples by isotope dilution ICP-MS. *Chemical Geology* **165**, 87–107.

Pearson, D. G., Irvine, G. J., Ionov, D. A., Boyd, F. R. & Dreibus, G. E. (2004). Re–Os isotope systematics and platinum group element fractionation during mantle melt extraction: a study of massif and xenolith peridotite suites. *Chemical Geology* **208**, 29–59.

Pearson, D. G., Parman, S. W. & Nowell, G. M. (2007). A link between large mantle melting events and continent growth seen in osmium isotopes. *Nature* **449**, 202–205.

Qi, L., Zhou, M. F., Malpas, J. & Sun, M. (2005). Determination of rare earth elements and Y in ultramafic rocks by ICP-MS after preconcentration using $Fe(OH)_3$ and $Mg(OH)_2$ coprecipitation. *Geostandards and Geoanalytical Research* **29**, 131–141.

Ramo, O. T., Haapala, I., Vaasjoki, M., Yu, J. H. & Fu, H. Q. (1995). 1700 Ma Shachang complex, northeast China: Proterozoic rapakivi granite not associated with Paleoproterozoic orogenic crust. *Geology* **23**, 815–818.

Rehkämper, M., Halliday, A. N., Barford, D., Fitton, J. G. & Dawson, J. B. (1997). Platinum-group element abundance patterns in different mantle environments. *Science* **278**, 1595–1598.

Reisberg, L. & Lorand, J. P. (1995). Longevity of sub-continental mantle lithosphere from osmium isotope systematics in orogenic peridotite massifs. *Nature* **376**, 159–162.

Reisberg, L., Lorand, J. P. & Bedini, R. M. (2004). Reliability of Os model ages in pervasively metasomatized continental mantle lithosphere: a case study of Sidamo spinel peridotite xenoliths (East African Rift, Ethiopia). *Chemical Geology* **208**, 119–140.

Reisberg, L., Zhi, X. C., Lorand, J. P., Wagner, C., Peng, Z. C. & Zimmermann, C. (2005). Re–Os and S systematics of spinel peridotite xenoliths from east central China: Evidence for contrasting effects of melt percolation. *Earth and Planetary Science Letters* **239**, 286–308.

Roy-Barman, M. & Allègre, C. J. (1994). $^{187}Os/^{186}Os$ ratios of mid-ocean ridge basalts and abyssal peridotites. *Geochimica et Cosmochimica Acta* **58**, 5043–5054.

Rudnick, R. L. & Walker, R. J. (2009). Interpreting ages from Re–Os isotopes in peridotites. In: Brey, G. P., Aulbach, S., Foley, S., Grütter, H. S., Höfer, H., Jacob, D. E., Lorenz, V., Stachel, T. & Woodland, A. B. (eds) *Proceedings of the Ninth International Kimberlite Conference. Lithos*, doi:10.1016/j.lithos.2009.04.042.

Rudnick, R. L., Gao, S., Ling, W. L., Liu, Y. S. & McDonough, W. F. (2004). Petrology and geochemistry of spinel peridotite xenoliths from Hannuoba and Qixia, North China craton. In: Mitchell, R. H., Grütter, H. S., Heaman, L. M., Scott Smith, B. H. & Stachel, T. (eds) *Proceedings of the 8th International Kimberlite Conference. Lithos* **77**, 609–637.

Saal, A. E., Takazawa, E., Frey, F. A., Shimizu, N. & Hart, S. R. (2001). Re–Os isotopes in the Horoman peridotite: evidence for refertilization? *Journal of Petrology* **42**, 25–37.

Salters, V. J. & Zindler, A. (1995). Extreme $^{176}Hf/^{177}Hf$ in the sub-oceanic mantle. *Earth and Planetary Science Letters* **129**, 13–30.

Shi, S. Y., Wen, H. L., Li., B., He, H. L. & Lu, C. F. (2001). Determination of carbon and sulfur in geological samples by high frequency IR-absorption spectrometric method (in Chinese with English abstract). *Rock and Mineral Analysis* **20**, 267–271.

Shirey, S. B. & Walker, R. J. (1995). Carius tube digestions for low-blank rhenium–osmium analysis. *Analytical Chemistry* **67**, 2136–2141.

Shirey, S. B. & Walker, R. J. (1998). The Re–Os isotope system in cosmochemistry and high temperature geochemistry. *Annual Review of Earth and Planetary Sciences* **26**, 423–500.

Snow, J. E. & Reisberg, L. (1995). Os isotopic systematics of the MORB mantle: results from altered abyssal peridotites. *Earth and Planetary Science Letters* **136**, 723–733.

Song, Y. & Frey, F. A. (1989). Geochemistry of peridotite xenoliths in basalt from Hannuoba, Eastern China: implications for subcontinental mantle heterogeneity. *Geochimica et Cosmochimica Acta* **53**, 97–113.

Standish, J. J., Hart, S. R., Blusztajn, J., Dick, H. J. B. & Lee, K. L. (2002). Abyssal peridotite osmium isotopic compositions from Cr-spinel. *Geochemistry, Geophysics, Geosystems* **3**, 1004, doi:10.1029/2001GC000161.

Tang, Y. J., Zhang, H. F., Ying, J. F., Zhang, J. & Liu, X. M. (2008). Refertilization of ancient lithospheric mantle beneath the central North China Craton: Evidence from petrology and geochemistry of peridotite xenoliths. *Lithos* **101**, 435–452.

Vervoort, J. D., Patchett, P. J., Blichert-Toft, J. & Albarède, F. (1999). Relationships between Lu–Hf and Sm–Nd isotopic systems in the global sedimentary system. *Earth and Planetary Science Letters* **168**, 79–99.

Walker, R. J., Carlson, R. W., Shirey, S. B. & Boyd, F. R. (1989). Os, Sr, Nd, and Pb isotope systematics of southern African peridotite xenoliths: Implications for the chemical evolution of subcontinental mantle. *Geochimica et Cosmochimica Acta* **53**, 1583–1595.

Walker, R. J., Prichard, H. M., Ishiwatari, A. & Pimentel, M. (2002). The osmium isotopic composition of convecting upper mantle deduced from ophiolite chromites. *Geochimica et Cosmochimica Acta* **66**, 329–345.

Walker, R. J., Brandon, A. D., Bird, J. M., Piccoli, P. M., McDonough, W. F. & Ash, R. D. (2005). $^{187}Os$–$^{186}Os$ systematics of Os–Ir–Ru alloy grains from southwestern Oregon. *Earth and Planetary Science Letters* **230**, 211–226.

Walker, R. J., McDonough, W. F., Honesto, J., Chabot, N. L., McCoy, T. J., Ash, R. D. & Bellucci, J. J. (2008). Modeling fractional crystallization of group IVB iron meteorites. *Geochimica et Cosmochimica Acta* **72**, 2198–2216.

Wang, W. Y., Takahashi, E. & Sueno, S. (1998). Geochemical properties of lithospheric mantle beneath the Sino-Korea craton: evidence from garnet xenocrysts and diamond inclusions. *Physics of the Earth and Planetary Interiors* **107**, 249–260.

Wells, P. R. A. (1977). Pyroxene thermometry in simple and complex systems. *Contributions to Mineralogy and Petrology* **62**, 129–139.

Wittig, N., Baker, J. A. & Downes, H. (2006). Dating the mantle roots of young continental crust. *Geology* **34**, 237–240.

Wittig, N., Baker, J. A. & Downes, H. (2007). U–Th–Pb and Lu–Hf isotopic constraints on the evolution of sub-continental lithospheric mantle, French Massif Central. *Geochimica et Cosmochimica Acta* **71**, 1290–1311.

Wood, B. J. & Banno, S. (1973). Garnet–orthopyroxene and orthopyroxene–clinopyroxene relationships in simple and complex systems. *Contributions to Mineralogy and Petrology* **42**, 109–124.

Wu, F. Y., Walker, R. J., Ren, X. W., Sun, D. Y. & Zhou, X. H. (2003). Osmium isotopic constraints on the age of lithospheric mantle beneath northeastern China. *Chemical Geology* **197**, 107–129.

Wu, F. Y., Lin, J. Q., Wilde, S. A., Zhang, X. O. & Yang, J.H. (2005*a*). Nature and significance of the Early Cretaceous giant igneous event in Eastern China. *Earth and Planetary Science Letters* **233**, 103–119.

Wu, F. Y., Zhao, G. C., Wilde, S. A. & Sun, D. Y. (2005*b*). Nd isotopic constraints on the crustal formation of the North China Craton. *Journal of Asian Earth Sciences* **24**, 523–545.

Wu, F. Y., Yang, J. H., Wilde, S. A. & Zhang, X.O. (2005*c*). Geochronology, petrogenesis and tectonic implications of Jurassic granites in the Liaodong Peninsula, NE China. *Chemical Geology* **221**, 127–156.

Wu, F. Y., Walker, R. J., Yang, Y. H., Yuan, H. L. & Yang, J. H. (2006). The chemical–temporal evolution of lithospheric mantle underlying the North China Craton. *Geochimica et Cosmochimica Acta* **70**, 5013–5034.

Wu, F. Y., Yang, J. H., Chu, Z. Y., Xie, L. W., Yang, Y. H. & Li, Q. L. (2007). Dating the subcontinental lithospheric mantle (in Chinese with English abstract). *Earth Science Frontiers* **14**, 76–86.

Wu, F. Y., Zhang, Y. B., Yang, J. H., Xie, L. W. & Yang, Y. H. (2008). Zircon U–Pb and Hf isotopic constraints on the Early Archean crustal evolution in Anshan of the North China Craton. *Precambrian Research* **167**, 339–362.

Xu, W. L., Hergt, J. M., Gao, S., Pei, F. P., Wang, W. & Yang, D. P. (2008). Interaction of adakitic melt–peridotite: implications for the high–Mg# signature of Mesozoic adakitic rocks in the eastern North China Craton. *Earth and Planetary Science Letters* **265**, 123–137.

Xu, X. S., Griffin, W. L., O'Reilly, S. Y., Pearson, N. J., Geng, H. Y. & Zheng, J. P. (2008*a*). Re–Os isotopes of sulfides in mantle xenoliths from eastern China: Progressive modification of lithospheric mantle. *Lithos* **102**, 43–64.

Xu, Y. G. (2001). Thermo-tectonic destruction of the Archaean lithospheric keel beneath eastern China: evidence, timing and mechanism. *Physics and Chemistry of the Earth (A)* **26**, 747–757.

Yang, J. H., Wu, F. Y., Liu, X. M. & Xie, L. W. (2005). Zircon U–Pb ages and Hf isotopes and their geological significance of the Miyun rapakivi granites from Beijing, China. *Acta Petrologica Sinica* **21**, 1633–1644.

Yang, J. H., Wu, F. Y., Wilde, S. A., Belousova, E. & Griffin, W. L. (2008). Mesozoic decratonization of the North China block. *Geology* **36**, 467–470.

Yang, Y. H., Wu, F. Y., Wilde, S. A., Liu, X. M., Zhang, Y. B., Xie, L. W. & Yang, J. H. (2009). *In-situ* perovskite Sr–Nd isotopic constraints on petrogenesis of the Mengyin kimberlites in the North China Craton. *Chemical Geology* **264**, 24–42.

Ying, J. F., Zhang, H. F., Kita, N., Morishita, Y. & Shimoda, G. (2006). Nature and evolution of Late Cretaceous lithospheric mantle beneath the eastern North China Craton: Constraints from petrology and geochemistry of peridotitic xenoliths from Jünan, Shandong Province, China. *Earth and Planetary Science Letters* **244**, 622–638.

Zhai, M. G. & Liu, W. J. (2003). Paleoproterozoic tectonic history of the North China Craton: a review. *Precambrian Research* **122**, 183–199.

Zhang, H. F. (2005). Transformation of lithospheric mantle through peridotite–melt reaction: A case of Sino-Korean craton. *Earth and Planetary Science Letters* **237**, 768–780.

Zhang, H. F. & Yang, Y. H. (2007). Emplacement age and Sr–Nd–Hf isotopic characteristics of the diamondiferous kimberlites from the eastern North China Craton (in Chinese with English abstract). *Acta Petrologica Sinica* **23**, 285–294.

Zhang, H. F., Ying, J. F., Tang, Y. J., Zhang, J., Zhao, X. M., Niu, L. F., Xiao, Y. & Su, B. X. (2006). Heterogeneity of Mesozoic and Cenozoic lithospheric mantle beneath the eastern North China Craton: evidence from olivine compositional mapping (in Chinese with English abstract). *Acta Petrologica Sinica* **22**, 2279–2288.

Zhang, H. F., Goldstein, S. L., Zhou, X. H., Sun, M., Zheng, J. P. & Cai, Y. (2008). Evolution of subcontinental lithospheric mantle beneath eastern China: Re–Os isotopic evidence from mantle xenoliths in Paleozoic kimberlites and Mesozoic basalts. *Contributions to Mineralogy and Petrology* **155**, 271–293.

Zhang, H. F., Goldstein, S. L., Zhou, X. H., Sun, M. & Cai, Y. (2009). Comprehensive refertilization of lithospheric mantle beneath the North China Craton: further Os–Sr–Nd isotopic constraints. *Journal of the Geological Society, London* **166**, 249–259.

Zhang, S. H., Liu, S. W., Zhao, Y., Yang, J. H., Song, B. & Liu, X. M. (2007). The 1·75–1·68 Ga anorthosite–mangerite–alkali granitoid–rapakivi granite suite from the northern North China Craton: magmatism related to a Paleoproterozoic orogen. *Precambrian Research* **155**, 287–312.

Zhang, S. H., Zhao, Y., Song, B., Hu, J. M., Liu, S. W., Yang, Y. H., Chen, F. K., Liu, X. M. & Liu, J. (2009). Contrasting Late Carboniferous and Late Permian–Middle Triassic intrusive suites from the northern margin of the North China craton: Geochronology, petrogenesis, and tectonic implications. *Geological Society of America Bulletin* **121**, 181–200.

Zhao, G. C., Sun, M., Wilde, S. A. & Li, S. Z. (2005). Late Archean to Paleoproterozoic evolution of the North China Craton: key issues revisited. *Precambrian Research* **136**, 177–202.

Zheng, J. P. (1999). *Mesozoic–Cenozoic mantle replacement and lithospheric thinning beneath the eastern China* (in Chinese with English abstract). Wuhan: China University of Geosciences Press, 126 pp.

Zheng, J. P., Sun, M., Zhou, M. F. & Robinson, P. (2005). Trace elemental and PGE geochemical constraints of Mesozoic and Cenozoic peridotitic xenoliths on lithospheric evolution of the North China Craton. *Geochimica et Cosmochimica Acta* **69**, 3401–3418.

Zheng, J. P., Griffin, W. L., O'Reilly, S. Y., Yang, J. S., Li, T. F., Zhang, M., Zhang, R. Y. & Liou, J. G. (2006). Mineral chemistry of peridotites from Paleozoic, Mesozoic and Cenozoic lithosphere: constraints on mantle evolution beneath eastern China. *Journal of Petrology* **47**, 2233–2256.

Zheng, J. P., Yu, C. M., Lu, F. X., Zhang, Z. H. & Tang, H. Y. (2007). Age and composition of continental mantle peridotites and implications for the lithospheric thinning, eastern North China (in Chinese with English abstract). *Earth Science Frontiers* **14**, 87–97.

## APPENDIX A: PETROGRAPHIC DESCRIPTIONS OF THE ANALYZED PERIDOTITES

| Sample | Rock type | Mineral assemblage (modal %) | Description |
|---|---|---|---|
| PL01 | Lherzolite | Ol (59) + Opx (26)+Cpx (12) + Sp (3) | Porphyroclastic texture with 3–5 mm grain-size of relict exsolved Opx. The groundmass has a grain-size of 1–2 mm, with sieve-textured Cpx |
| PL02 | Harzburgite | Ol ((75) + Opx (21) + Cpx (3) + Sp (1) | Protogranular texture with grain-size of 1–2 mm. Ol, Opx and Cpx show equilibrium grain boundaries. Some spinels have broken down with variable residues |
| PL03 | Lherzolite | Ol (53) + Opx (30) + Cpx (14) + Sp (3) | Protogranular texture with grain-size of ~1 mm. Most Cpx show reaction rims |
| PL06 | Lherzolite | Ol (56) + Opx (25) + Cpx (15) + Sp (4) | Coarse-grained equigranular texture with grain-size of 2–3 mm. Ol, Opx and Cpx form triple junctions. Some Cpx are modified with sieve-textured rims |
| PL07 | Lherzolite | Ol (56) + Opx (25) + Cpx (15) + Sp (3) | Protogranular texture with grain-size of 1 mm. Opx porphyoclasts can be found occasionally, and no reaction rim is identified for Cpx |
| PL08 | Lherzolite | Ol (73) + Opx (19) + Cpx (6) + Sp (2) | Porphyroclastic texture with ~3 mm Opx blasts and 1 mm matrix crystals. Ol occurs as tabular crystals |
| PL13 | Lherzolite | Ol (59) + Opx (25) + Cpx (13) + Sp (3) | Coarse-grained peridotite with 4–6 mm porphyroclastic Opx; the rest of the minerals are ~3 mm |
| PL14 | Lherzolite | Ol (61) + Opx (23) + Cpx (13) + Sp (3) | Porphyroclastic texture with ~3 mm Opx. The groundmass is <1 mm |
| PL16 | Lherzolite | Ol (58) + Opx (25) + Cpx (14) + Sp (3) | Medium-grained equigranular texture with a grain-size of 1–2 mm; triple junctions are well developed between Ol,Cpx and Opx |
| PL17 | Lherzolite | Ol (60) + Opx (26) + Cpx (11) + Sp (3) | Medium-grained equigranular texture with grain-size of 1–2 mm. Ol, Opx and Cpx mostly form equilibrated triple junctions. Some Cpx develops sieve texture along the grain margin |
| PL18 | Harzburgite | Ol (71) + Opx (22) + Cpx (5) + Sp (3) | Tabular, equigranular texture with grain-size of ~1 mm. Most Sp is decomposed with a reaction rim |
| PL19 | Lherzolite | Ol (68) + Opx (22) + Cpx (8) + Sp (2) | Equigranular texture with grain-size of ~1 mm. Most Ol, Opx and Cpx form triple junctions, indicating their equilibrium occurrence. Most Sp have reaction rim |
| PL23 | Harzburgite | Ol (64) + Opx (30) + Cpx (4) + Sp (2) | Coarse-grained protogranular texture with grain-size o f 3–5 mm. Cpx is characterized by reaction rim |
| SW01 | Wehrlite | | Resorption texture with grain-size of 3–5 mm. Ol is surrounded by sieve-textured clinopyroxene. Some Ol are weakly serpentinized |
| SW02 | Lherzolite | Ol (59) + Opx (21) + Cpx (18) + Sp (3) | Protogranular texture with grain-size of 0·5–1·5 mm. Opx porphyroclasts occasionally occur up to 4 mm. Serpentinization is observed on fractures, along with minor carbonates |
| SW03 | Lherzolite | Ol (52) + Opx (35) + Cpx (11) + Sp (2) | Protogranular texture with grain-size of ~1 mm. Most Ol are serpentinized with few fresh grains |
| SW04 | Pyroxenite | Ol (35) + Opx (15) + Cpx (50) + Sp (<1) | Mosaic porphyroclastic texture. Opx forms porphyroclasts with maximum grain-size of ~5 mm. The groundmass, composed of Ol, Cpx and Opx, is usually <0·4 mm. Basaltic glass and minor carbonates are identified on grain boundaries |
| SW05 | Lherzolite | Ol (64) + Opx (23) + Cpx (11) + Sp (2) | Protogranular texture with grain-size of 1–2 mm. Ol are weakly serpentinized; Cpx is sieve-textured. Sp mostly occur within the sieve-textured Cpx as inclusions |

(continued)

*Appendix A: Continued*

| Sample | Rock type | Mineral assemblage (modal %) | Description |
|---|---|---|---|
| SW06 | Lherzolite | Ol (61) + Opx (27) + Cpx (10) + Sp (2) | Porphyroclastic texture; Opx porphyroclasts have a grain size of ~2 mm. Other minerals are <0·5 mm |
| SW07 | Harzburgite | Ol (77) + Opx (18) + Cpx (5) + Sp (1) | Equigranular texture with banded structure. Cpx mostly has thin reaction rims, and Sp occurs along the layering |
| SW08 | Lherzolite | Ol (61) + Opx (22) + Cpx (14) + Sp (3) | Equigranular texture with grain-size of <1 mm. Some Cpx and Sp show sieve textures along their margins |
| SW09 | Lherzolite | Ol (73) + Opx (18) + Cpx (8) + Sp (2) | Equigranular texture with grain-size of <1 mm; weak serpentinization. Most Cpx show reaction rims |
| SW10 | Lherzolite | Ol (63) + Opx (22) + Cpx (12) + Sp (3) | Porphyroclastic texture with Opx, and sometimes Ol, occurring as porphyroclasts with grain-size of ~4 mm. Some Ol inclusions in Opx porphyroclasts |
| SW11 | Lherzolite | Ol (65) + Opx (21) + Cpx (13) + Sp (2) | Granuloblastic texture with equilibrated Ol, Opx and Cpx. Serpentinization occurs along fractures, in which very thin (<0·1 mm width) carbonate vein is identified |
| SW12 | Lherzolite | Ol (57) + Opx (25) + Cpx (15) + Sp (3) | Porphyroclastic texture with Opx as porphyroclast (grain size of ~2–3 mm). Other minerals are mostly <1 mm |
| SW13 | Lherzolite | Ol (65) + Opx (22) + Cpx (10) + Sp (3) | Porphyroclastic texture. Opx, and sometimes Ol, occur as porphyroclasts with grain-sizes of ~3–4 mm |
| SW14 | Lherzolite | Ol (62) + Opx (21) + Cpx (14) + Sp (3) | Granuloblastic texture with grain-size of <1 mm. Serpentinization is developed along fractures. Minor basalt glass droplet is identified |
| SW15 | Lherzolite | Ol (62) + Opx (24) + Cpx (13) + Sp (2) | Granuloblastic texture with grain-size of 1–2 mm. Fresh Ol, Opx and Cpx form triple junctions |
| SW16 | Lherzolite | Ol (66) + Opx (23) + Cpx (10) + Sp (2) | Granuloblastic texture with grain-size of 1–2 mm. Some Cpx develop reaction rims; weak serpentinization occurs along fractures |
| SW17 | Lherzolite | Ol (58) + Opx (26) + Cpx (13) + Sp (3) | Mosaic porphyroclastic texture. Opx and sometimes Ol occur as porphyroclasts with a grain-size of ~3 mm. Most Cpx show resorption textures, and Sp usually coexists with the sieve-textured Cpx |
| SW18 | Lherzolite | Ol (72) + Opx (16) + Cpx (10) + Sp (2) | Mosaic porphyroclastic texture; Opx and Ol occur as porphyroclasts with grain-size of ~3 mm. The relatively fine-grained minerals have grain-size of ~1 mm |
| SW19 | Lherzolite | Ol (60) + Opx (16) + Cpx (22) + Sp (1) | Granuloblastic texture with grain-size of ~1 mm. Serpentinization is developed along fractures, in which some thin carbonate veins with width of <0·1 mm are identified |
| SW20 | Lherzolite | Ol (73) + Opx (16) + Cpx (9) + Sp (2) | Mosaic porphyroclastic texture with Opx occurring as porphyroclasts with grain-size of ~4 mm |
| SW21 | Wehrlite | Ol (64) + Opx (3) + Cpx (30) + Sp (4) | Coarse and poikilitic texture. The coarse-grained Ol has grain-size of ~4–6 mm; some fine-grained Ol occurs as inclusions within Opx. Most Cpx show sieve texture. Serpentinite occurs along fractures with minor carbonate |
| SW22 | Lherzolite | Ol (61) + Opx (26) + Cpx (11) + Sp (2) | Granuloblastic texture with grain-size of <2 mm. The fresh Cpx rarely develops sieve texture |

Ol, olivine; Opx, orthopyroxene; Cpx, clinopyroxene; Sp, spinel. Numbers in parentheses are modal abundances calculated from mass balance (Hermann & Berry, 2002).

## APPENDIX B: ANALYTICAL METHODS

### XRF

Approximately 0·5 g of rock powder was mixed with ~3·6 g of $Li_2B_4O_7$ and 3–4 drops of $NH_4Br$ and the mixture was fused in a furnace to form a glass disk. The disks were then analyzed using a Shimadzu XRF 1500 with a current and voltage of 50 mA and 50 kV, respectively. The analytical results for Chinese ultramafic rock standard DZE-1 are reported in Table B1.

### ICP-MS

About 100 mg of crushed whole-rock powder were dissolved in 2 ml HF and 1 ml $HNO_3$ in a closed Teflon bomb, which was heated on a hot plate at ~140°C, then opened and subsequently evaporated to dryness to remove silica. Then, 1·5 ml HF, 1·5 ml $HNO_3$ and 10 μl $HClO_4$ were added to the Teflon bomb. The bomb was placed in a steel jacket and heated in an oven at 190°C for 5 days to completely dissolve the sample. This was followed by dry-down and addition of concentrated $HNO_3$ to form nitrates, followed by a final evaporation. Then, 2 ml 50% $HNO_3$ was added to the Teflon bomb, which was subsequently put it into the jacket again and heated to 150°C for 24 h. Finally, 0·5 g Rh (1 ppm) was added to the solution as an internal standard, and then the solution was diluted by a factor of 500. The solutions were then ready for ICP-MS analysis. The analytical results for peridotite reference materials JP-1 and WPR-1 are reported in Table B2.

### S analysis

Samples were weighed into crucibles with Fe and W chips added as accelerators to ensure complete combustion of the sample. The crucible was then heated in an RF induction furnace in a stream of $O_2$ and the sulfur derived as gaseous $SO_2$ and $SO_3$. The gases were then passed through a dust filter, drying tube ($SO_2$ dissolves in water, thus water must be removed) and finally through a catalyst tube to ensure conversion to dioxides. From there the gases were directed into a sulfur IR absorption cell and the $SO_2$ peak was converted to S values. These values were then adjusted for calibration and sample weight to give the final concentration.

### Sr–Nd–Hf isotopic analysis

About 150–300 mg of cpx powder was weighed into 7 ml Savillex™ Teflon beakers, and appropriate amounts of mixed $^{87}Rb$–$^{84}Sr$, $^{149}Sm$–$^{150}Nd$, $^{176}Lu$, and $^{180}Hf$ spikes were added. The samples were dissolved using a mixed acid of 2 ml HF and 0·2 ml $HClO_4$ on a hotplate at 120°C for more than 1 week. After the samples were completely dissolved, the solutions were dried on hotplate at 130–180°C to remove the HF and $HClO_4$. The sample residues were re-dissolved in 4 ml of 6M HCl, and then dried down again. Finally, the samples were dissolved in 5 ml of 3M HCl.

The solutions were loaded onto pre-conditioned Eichrom® LN (LN-C-50A, 100–150 μm, 2 ml) chromatographic columns. The Rb, Sr, Sm, Nd, and matrix elements were eluted with 3M HCl. Then, the Lu was stripped with 4M HCl. After this step, Ti was removed with a mixed solution of 4M HCl and 0·5% $H_2O_2$. Then, Hf (and Zr) was stripped with a mixed acid of 6M HCl and 0·2M HF.

The Sr, Nd collections from the LN columns were dried down and re-dissolved in 1 ml 2·5M HCl, and then the solutions were loaded onto pre-conditioned cation exchange columns packed with AG50W × 12 resins (200–400 mesh, 2 ml). Rubidium and Sr were stripped with 5 M HCl, and then REE were stripped with 6M HCl.

The REE collections were dried down and re-dissolved in 0·4 ml 0·25M HCl, and then the solutions were loaded onto pre-conditioned Eichrom® LN (LN-C-50B, 100–150 μm, 2 ml) chromatographic columns. The La, Ce and a portion of the Pr were eluted with 6 ml 0·25M HCl, and the Nd was stripped with 3 ml 0·4M HCl, and then the Sm was stripped with 4 ml 0·8M HCl.

### Re–Os and PGE analysis

About 2 g of finely ground sample powder (200–400 mesh), and appropriate amounts of a $^{187}Re$–$^{190}Os$ mixed spike and a $^{191}Ir$–$^{99}Ru$–$^{194}Pt$–$^{105}Pd$ mixed spike were weighed into a clean, dry, chilled Pyrex® borosilicate glass Carius tube. Then, 3 ml of purified concentrated HCl and 6 ml of purified concentrated $HNO_3$ were added into the tube, and then the tube was sealed (Shirey & Walker, 1995). The digestions were performed at ~240°C for 48–72 h in an oven at IGGCAS and at ~260°C for 48–72 h in an oven at UMD. After opening the tubes, Os was extracted from the aqua regia solution into $CCl_4$ (Cohen & Waters, 1996) and then back-extracted into HBr, followed by purification via microdistillation (Birck *et al.*, 1997). The total procedural Os blank was 3–5 pg with a $^{187}Os/^{188}Os$ of about 0·15 at IGGCAS and about 0·5 pg with a $^{187}Os/^{188}Os$ of about 0·17 at UMD, respectively. The blank correction on Os concentrations and Os isotopic ratios was negligible for all samples.

Rhenium and remaining PGE (Ir, Ru, Pt, Pd) were separated from the matrix and purified by anion exchange chromatography using 2 ml resin (AG 1 × 8, 100–200 mesh) (Walker *et al.*, 2008). The Re, Ru fraction was eluted with 6M $HNO_3$, Ir and Pt were eluted with 13·5M $HNO_3$, and the Pd was eluted with 10M HCl. The Re was further purified using a small anion exchange column packed with 0·1 ml resin at UMD. All the collected fractions were dried down and re-dissolved in 1 ml of 0·8M $HNO_3$, for ICP–MS measurement. Total procedural

blanks were about 3 pg for Re, 7 pg for Ir, 7 pg for Ru, 4 pg for Pt and 4 pg for Pd at IGGCAS, and about 5 pg for Re, 4 pg for Pd, 10 pg for Pt, 1 pg for Ir, and 3 pg for Ru at UMD. The blank corrections were negligible (<1%) for Ir, Ru, Pt and Pd, but were as great as 10–70% for Re for some low-Re samples.

*Table B1: Analytical results of Chinese ultramafic rock standard DZE-1 by XRF (wt %)*

| | $SiO_2$ | $TiO_2$ | $Al_2O_3$ | $TFe_2O_3$ | MnO | MgO | CaO | $Na_2O$ | $K_2O$ | $P_2O_5$ | LOI | Total |
|---|---|---|---|---|---|---|---|---|---|---|---|---|
| Measured | 34·54 | 0·01 | 0·75 | 6·88 | 0·07 | 40·95 | 0·03 | 0·01 | 0·04 | 0·01 | 15·20 | 98·49 |
| Reference value* | 34·34 | 0·008 | 0·67 | 6·9 | 0·068 | 41·03 | 0·1 | 0·008 | 0·01 | 0·004 | | |

*Source: Govindaraju (1994).

*Table B2: Analytical results of ultramafic rock standard materials by ICP-MS (ppm)*

| Element | JP-1 | | | | | WPR-1 | |
|---|---|---|---|---|---|---|---|
| | Measured | References | | | | Measured | References |
| | ($n=1$) | Dulski (2001) | Qi *et al.* (2005) | Makishima *et al.* (2006) | GeoREM* | ($n=1$) | GeoREM* |
| Ni | 2508 | | | | 2460 | 2780 | 2900 |
| Cu | 5·0 | | | | 5·7–6·72 | 1514 | 1640 |
| Zn | 50 | | | | 43–61 | 91·8 | 95 |
| Sr | 0·605 | 0·63 | | 0·546 | | 7·05 | 7 |
| Y | 0·088 | 0·097 | 0·088 | 0·082 | | 4·18 | 5 |
| Zr | 5·6 | 5·5 | | | | 19·2 | 18 |
| Nb | 0·042 | | | | 0·0336–1 | 1·97 | 2·4 |
| Ba | 9·05 | 9·2 | | 9·5 | | 25·6 | 22 |
| La | 0·029 | 0·034 | 0·031 | 0·027 | | 2·03 | 2·2 |
| Ce | 0·060 | 0·063 | 0·054 | 0·060 | | 5·63 | 6 |
| Pr | 0·0078 | 0·0089 | 0·0076 | 0·0074 | | 0·773 | 0·7 |
| Nd | 0·033 | 0·033 | 0·030 | 0·0318 | | 3·59 | 3·5 |
| Sm | 0·0097 | 0·009 | 0·0077 | 0·0084 | | 0·907 | 0·9 |
| Eu | 0·0029 | 0·0021 | 0·0011 | 0·0024 | | 0·294 | 0·31 |
| Gd | 0·012 | 0·0092 | 0·0064 | 0·0097 | | 1·00 | 0·9 |
| Tb | 0·0024 | 0·0016 | 0·0017 | 0·0019 | | 0·155 | 0·1–0·2 |
| Dy | 0·015 | 0·013 | 0·013 | 0·015 | | 0·938 | 1·1 |
| Ho | 0·0038 | 0·003 | 0·0031 | 0·0036 | | 0·184 | 0·18 |
| Er | 0·012 | 0·011 | 0·011 | 0·012 | | 0·511 | 0·5 |
| Tm | 0·0024 | 0·0023 | 0·0021 | 0·0024 | | 0·0711 | 0·09 |
| Yb | 0·022 | 0·021 | 0·019 | 0·021 | | 0·466 | 0·48 |
| Lu | 0·0046 | 0·004 | 0·0034 | 0·0042 | | 0·0716 | 0·07 |
| Hf | 0·13 | 0·127 | | | | 0·579 | 0·61 |
| Ta | 0·0035 | | | | 0·00304–0·068 | 0·117 | 0·21 |
| Pb | 0·128 | 0·18 | | 0·0765 | | 5·25 | 6 |
| Th | 0·010 | 0·012 | | 0·013 | | 0·329 | 0·4 |
| U | 0·014 | 0·0116 | | 0·014 | | 0·182 | 0·17 |

GeoREM: http://georem.mpch-mainz.gwdg.de/.

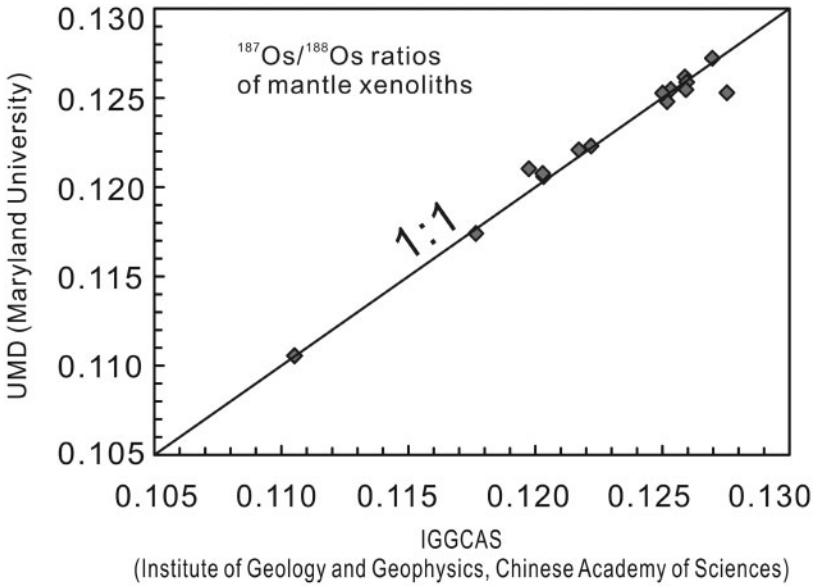


**Fig. B1.** Comparison of analytical results of Os isotopic ratios between UMD and IGGCAS. UMD: measured at University of Maryland; IGGCAS: measured at Institute of Geology and Geophysics, Chinese Academy of Sciences.